

THE FUNCTION OF NON-MUSCLE MYOSIN 2C IN THE INTESTINAL EPITHELIUM

By

Colbie Rose Chinowsky

Dissertation

Submitted to the Faculty of the
Graduate School of Vanderbilt University
in partial fulfillment of the requirements

for the degree of

DOCTOR OF PHILOSOPHY

in

Cell and Developmental Biology

October 31st, 2021

Nashville, Tennessee

Approved by:

Irina Kaverina, Ph.D

Christopher Williams, M.D, Ph.D

Adrian Olivares, Ph.D

Dylan Burnette, Ph.D

Matthew Tyska, Ph.D

For all those who have felt like they don't belong in science.

ACKNOWLEDGEMENTS

The first people I must acknowledge are the faculty, staff, and students of the Physics department at Mount Holyoke College. Late nights in the physics lounge was where I first fell in love with science, and the physics faculty were the only reason I applied for PhD programs, or even knew what getting a PhD entailed. I would not be here without their continual guidance and support at the very beginning of my scientific career. Mount Holyoke gave me the confidence to pursue science in the way I wanted to and taught me that there is a place for everyone in science.

Next, I must give my heartfelt thanks to my mentor, Dr. Matthew Tyska. I think you believed in my abilities more than I did. You have taught me how to build experiments, question the world, share science with other, and given me the independence to grow into myself, while being supportive and encouraging every step of the way. I cannot imagine doing my PhD in any other lab. It has been an absolute privilege to complete this stage of my scientific training the in Tyska lab.

On that note, I must acknowledge the lab members, past and present, who made my time in the Tyska lab so special. Meredith, who was my first introduction to the lab, and would always advocate on my behalf. Meagan, Leslie and Bryan, who gave me guidance when I barely understood how to culture cells. Julia, who I found wandering in the halls of MRBIII, and would become one of my closest and most valued friends in Nashville. Bella and Angelo, the other members of the “Three Musketeers”. Having two other people along for the ride made it that much better. Caroline, and Gill, my lab neighbors, putting up with timers beeping for too long, and quite a few mutterings of frustration. Our newest lab members, Deanna, Julissa, Olivia and Jen, who have all

added so much to the lab, and only made it a better environment to do science. Every single member of the Tyska lab has made being in lab fun, provided a listening ear for frustrations (science related or not), and been an incredibly valuable source of ideas and feedback. I must also acknowledge the incredible resources available at Vanderbilt, and their commitment to creating a training environment unlike any other. The department of Cell and Developmental Biology, the Molecular Biophysics community, and the members of the Microtubules and Motors club have all provided valuable feedback over the years, and helped create an environment filled with learning and ideas.

Next, the team that has become a huge part of my life, and always has my back. I picked up the sport of weightlifting during my second year of graduate school, and this sport has given me so much. My coach, Cortney, who knows when I'm stressed before I've even acknowledged it, and gives me a space to vent, and grow as an athlete and a person. The members of CB Weightlifting always encourage me and gave me a shoulder to lean on whenever things got hard. Mo and Kara, your friendship has meant the world to me, and been the best source of fun over the last few years.

Ben. I don't know how you've managed to stick by my side over the last four years. It has never been easy, but you've been there every step of the way, with support and love. I was never looking for this, but I'm so glad I found you. Thank you for making me laugh when the world gets too heavy, making sure I eat when I'm busy, and always believing in me. I love you so much.

TABLE OF CONTENTS

	Page
ACKNOWLEDGEMENTS	III
LIST OF FIGURES	VIII
CHAPTER 1	1
THE CYTOSKELETON.....	1
<i>Actin</i>	2
<i>Filopodia</i>	5
<i>Microvilli</i>	6
<i>Stereocilia</i>	9
MOLECULAR MOTORS	10
<i>Myosin super-family</i>	11
<i>Myosin-2</i>	16
ROLE OF CONTRACTILE FORCE IN BIOLOGY	20
<i>Cell shape</i>	21
<i>Tissue morphogenesis</i>	23
THE GASTROINTESTINAL TRACT	24
<i>Development and morphogenesis</i>	26
<i>Crypt-villus migration and differentiation</i>	28
<i>Enterocytes</i>	30
<i>Paneth cells</i>	30
<i>Goblet cells</i>	31
<i>Tuft cells</i>	31
<i>Enteroendocrine cells</i>	32
<i>Plasticity of the intestine and homeostasis</i>	32
<i>The intestinal epithelium and the brush border</i>	33
<i>The terminal web</i>	35
SUMMARY	37
CHAPTER 2	39
CELL CULTURE AND IMMUNOFLUORESCENCE	39
CLONING AND CONSTRUCTS.....	40
TRANSFECTIONS AND LENTIVIRUS PRODUCTION	40
DRUG TREATMENTS.....	41
IN VIVO BLEBBISTATIN TREATMENT, ANIMAL SURGERY AND TISSUE PREPARATION	42
WHOLE MOUNT TISSUE PREPARATION AND IMMUNOFLUORESCENCE	42
ORGANOID CULTURE AND IMMUNOFLUORESCENCE	43
FORMALIN-FIXED PARAFFIN EMBEDDED SWISS ROLL PREPARATION AND IMMUNOHISTOCHEMISTRY	44

LIGHT MICROSCOPY	45
ELECTRON MICROSCOPY	46
IMAGE ANALYSIS AND STATISTICAL TESTING	47
CHAPTER 3.....	50
SUMMARY.....	50
INTRODUCTION	51
RESULTS	55
<i>NM2C is enriched in the enterocyte brush border terminal web in vivo</i>	55
<i>Terminal web and junctional NM2C puncta exhibit continuous remodeling</i>	59
<i>Activation of NM2 leads to shortening of microvilli</i>	61
<i>Inhibition of NM2 leads to microvillar elongation</i>	68
<i>Blebbistatin reverses the impact of calyculin A on microvillar length</i>	68
<i>NM2 promotes actin turnover in brush border microvilli</i>	70
<i>Knockdown of NM2C results in aberrant actin structures and limited viability</i>	71
<i>NM2C motor domain activity is required for limiting microvillar length</i>	74
DISCUSSION.....	79
<i>NM2C activity limits the length of dynamic epithelial microvilli</i>	79
<i>Organization of NM2C in the terminal web</i>	80
<i>Contractility-dependent actin turnover as a conserved function for NM2</i>	82
<i>Additional roles for NM2C in polarized epithelia</i>	85
CHAPTER 4.....	87
INTRODUCTION	87
RESULTS	93
<i>NM2C KO mice display abnormal gross intestinal morphology.</i>	93
<i>Whole-mount imaging reveals the extent of three-dimensional morphology changes.</i>	95
<i>NM2C forms a continuous layer across the apical surface.</i>	99
<i>Loss of NM2C disrupts apical ultrastructure.</i>	101
<i>Absence of NM2C alters cell shape and tissue integrity.</i>	104
<i>Aberrant growth and junctional defects are epithelial cell-autonomous.</i>	108
<i>Loss of NM2C induces tuft cell hyperplasia in a cell-autonomous manner.</i>	111
DISCUSSION.....	114
<i>Role of known NM2C mutations in disease</i>	114
<i>Maintenance of villus shape</i>	115
<i>Tension in the intestinal epithelium</i>	115
CHAPTER 5.....	118

ROLE OF COFILIN IN REGULATING BB LENGTH	118
LOSS OF NM2C MAY IMPACT CELL MIGRATION	122
ASSESSING THE ROLE OF MYOSIN-2 INHIBITION/ACTIVATION IN VIVO	126
ROLE OF NM2C IN TUFT CELLS.....	129
INVESTIGATING MOLECULAR ORGANIZATION OF NM2C IN THE TERMINAL WEB	132
ROLE OF NM2C IN OTHER ORGAN SYSTEMS	133
CONCLUSIONS.....	135
REFERENCES.....	137

LIST OF FIGURES

	Page
Figure 1-1: Cartoon schematic of actin polymerization.....	4
Figure 1-2: Types of cellular actin-based protrusions.....	5
Figure 1-3: Schematic of various actin-associated proteins within microvilli.	7
Figure 1-4: Phylogenetic tree of the myosin superfamily.....	13
Figure 1-5: Crystal structure of conserved myosin head region.	14
Figure 1-6: Graphical depiction of the myosin crossbridge cycle.	16
Figure 1-7: Schematic of various forms of myosin 2.	16
Figure 1-8: Negative stain electron microscopy of all three non-muscle myosin filaments.....	19
Figure 1-9: Mechanisms of cell shape change.	22
Figure 1-10: Cartoon of the structure and morphology of the small intestine.	26
Figure 1-11: schematic of the various types of intestinal epithelial cells.....	29
Figure 1-12: Ultrastructure of the brush border.	34
Figure 1-13: The terminal web supports the brush border. Quick freeze deep-etch electron micrograph of the brush border and terminal web. Scale bar = 0.1µm. Adapted from Hirokawa et al., 1982 [3].	36
Figure 3-1: : Cell type-specific expression of myosin genes in the mouse ileal epithelium assessed by scRNA-seq.	56
Figure 3-2: NM2C localizes to the enterocyte terminal web..	58
Figure 3-3: Medial and junctional populations NM2C puncta exhibit similar dynamics.	60
Figure 3-4: NM2C localizes specifically to the terminal web of W4 cells.	61
Figure 3-5: Activation of NM2 shortens epithelial microvilli.	66
Figure 3-6: Activation of NM2C with 4-HAP shortens epithelial microvilli.	67
Figure 3-7: Inhibition of NM2 elongates microvilli and limits actin turnover.	69
Figure 3-8: NM2C KD results in aberrant actin structures.	73
Figure 3-9: A functional NM2C motor domain is required for microvillar length regulation..	78
Figure 3-10: Model of contractility-dependent actin turnover in brush border microvilli.	80
Figure 4-1 Crypts of WT and KO mice are positive for proliferative marker, Ki67.	93

Figure 4-2: NM2C KO mice display abnormal gross intestinal morphology.....	94
Figure 4-3 :Whole mount imaging reveals extent of three-dimensional morphology changes.....	98
Figure 4-4: NM2C forms a continuous layer.....	101
Figure 4-5: Loss of NM2C perturbs ultrastructure.	104
Figure 4-6: Loss of NM2C results in changes to cell shape and tissue integrity.....	106
Figure 4-7: KO phenotypes are present in organoids and epithelial cell autonomous.	110
Figure 4-8: KO of NM2C results in tuft cell hyperplasia in vivo and in organoid cultures.	114
Figure 5-1: Cofilin influences actin dynamics in a variety of ways.	119
Figure 5-2: Potential role of cofilin in the brush border.	120
Figure 5-3: Preliminary data suggests cell migration is impaired with loss of NM2C...	124
Figure 5-4: In vivo perfusion of Blebbistatin..	127
Figure 5-5: Tuft cells lack medial NM2C expression.	132
Figure 5-6: Determining orientation of NM2C filaments in the terminal web.	132
Figure 5-7: NM2C displays tissue specific localization..	135

CHAPTER 1

INTRODUCTION

THE CYTOSKELETON

The cytoskeleton is an integral part of all eukaryotic cells. Comprised of networks of filamentous polymers and regulatory proteins, the cytoskeleton allows a cell to transport cargo, change shape, and resist deformation [7]. Notably, the cytoskeleton plays a critical role in cell division and the maturation of cell-cell junctions, which allows for large sheets of cells to form a robust barrier, a function critical for an organism's survival [7, [8]. It is not an exaggeration to state that the study of the cytoskeleton is absolutely a fundamental part of modern cell biology.

There are three types of filaments that are key components of the cytoskeleton: microtubules, intermediate filaments, and actin. Microtubules are 25 nm in diameter, formed from tubulin subunits and are classically known for their role in orienting chromosomes during cell division and providing a substrate for long-range intracellular transport [9]. Intermediate filaments are about 10 nm in diameter, and perhaps the most understudied component of the mammalian cytoskeleton. They are known to play important structural roles in various cell types [9]. Actin is the smallest of the cytoskeletal filaments at 6-7 nm in diameter and known providing mechanism support for the cell and producing driving force required for movement. As actin is an integral part of this dissertation, we will now discuss it in more detail than the other cytoskeletal filaments.

Actin

Actin exists in two forms within a cell: globular actin, or G-actin, and filamentous actin, or F-actin (Figure 1-1). G-actin consists of a single 43 kDa protein, which contains an “ATPase fold”, where the molecular can bind ATP and hydrolyze it to ADP [9]. Unbound G-actin in the cytoplasm is typically bound to ATP. F-actin is a polymer formed from G-actin monomers bound together to form a helical multi-strand filament. An actin filament has structural polarity due to the orientation of the G-actin subunits, which are rotated by 166° within the filament, which gives F-actin its characteristic double-stranded helix appearance [9]. One end of the actin filament will have an exposed ATP binding site (known as the minus end), whereas the other end will have the ATP binding side oriented towards the adjacent subunit (known as the plus end). Classically, the minus end is also known as the pointed end and the plus end as the barbed end. This nomenclature arose due to the appearance of actin filaments in early TEM images, where the actin filaments were labeled with myosin subfragment 1 (S1) decoration [10].

Actin filaments are known for their highly dynamic nature and ability to undergo a process known as “treadmilling”. A treadmilling actin filament will remain approximately the same length; new g-actin monomers are continuously added at the barbed ends, while monomers are continuously disassociating from the pointed end [11]. This treadmilling action is possible due to differing critical concentrations (C_c) at the barbed and pointed ends. Thus, the critical concentration required at the barbed end is $0.1 \mu\text{M}$ (C_c^B), while the critical concentration for the pointed end is $0.8 \mu\text{M}$ (C_c^P). A steady state of treadmilling occurs when the concentration of actin is between C_c^B and C_c^P [12]. Actin filaments are inherently responsible for many of the mechanical properties of the cytoplasm, and are capable of producing enough force to deform the plasma membrane

[13], resulting in actin-based protrusions, which will be discussed in detail later in this introduction.

In vitro, actin filaments will polymerize in a solution that only contains G-actin under physiological salt conditions [14]. However, purified actin will produce filaments that turnover slowly. Within a cell, actin can depolymerize and polymerize much more rapidly, thanks to over 60 families of actin binding proteins. These actin-binding proteins serve to regulate where and when actin filaments form. The concentration of G-actin in a single cell is far more than the critical concentration required for *in vitro* polymerization, and without regulatory proteins, the actin within a cell would rapidly polymerize and remain relatively static. *In vivo*, there are several classes of protein that work to regulate actin [15]. One class is “nucleators”: nucleators assist in the formation of an actin nucleus, which consists of three actin monomers bound together (Figure 1-1). The formation of an actin nucleus is an energy barrier that must be overcome for an actin filament to begin elongation. Nucleators such as formins and the Arp2/3 complex reduce this energy barrier and allow for more actin filament growth than would be possible with g-actin alone [16]. To balance nucleators, a variety of actin severing proteins are also present within the cytoplasm, the most prolific being cofilin. More precisely, the actin depolymerization factor (ADF)/Cofilin family of proteins are widely responsible for regulating the length of actin filaments by severing the pointed end. Cofilin plays a crucial role in regulating cell migration, shape, and motility [17].

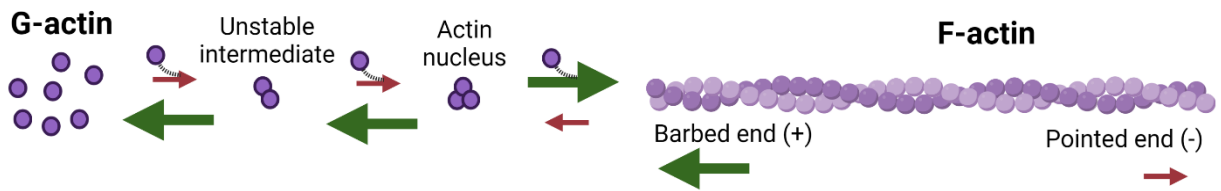


Figure 1-1: Cartoon schematic of actin polymerization.

There are far too many actin-binding proteins to discuss for this introduction, so finally, we shall introduce actin-bundling proteins, which are of particular import for creating and maintaining actin-based protrusions. Bundling proteins include villin, espin, fascin, and fimbrin. Bundling proteins serve to bring several actin filaments together in parallel; such structures are known as actin bundles. Actin bundles are typically present in highly complex cellular structures, as bundled actin has high tensile strength and can support various specific functions [13]. Three such structures are filopodia, stereocilia, and microvilli, which will be discussed in detail (Figure 1-2). However, it is essential to note that actin-based protrusions are highly evolutionarily conserved, with protrusions of bundled actin observed in elementary organisms such as sponges, where the feeding

cells, choanocytes, have many actin protrusions at their surface [18, [19].

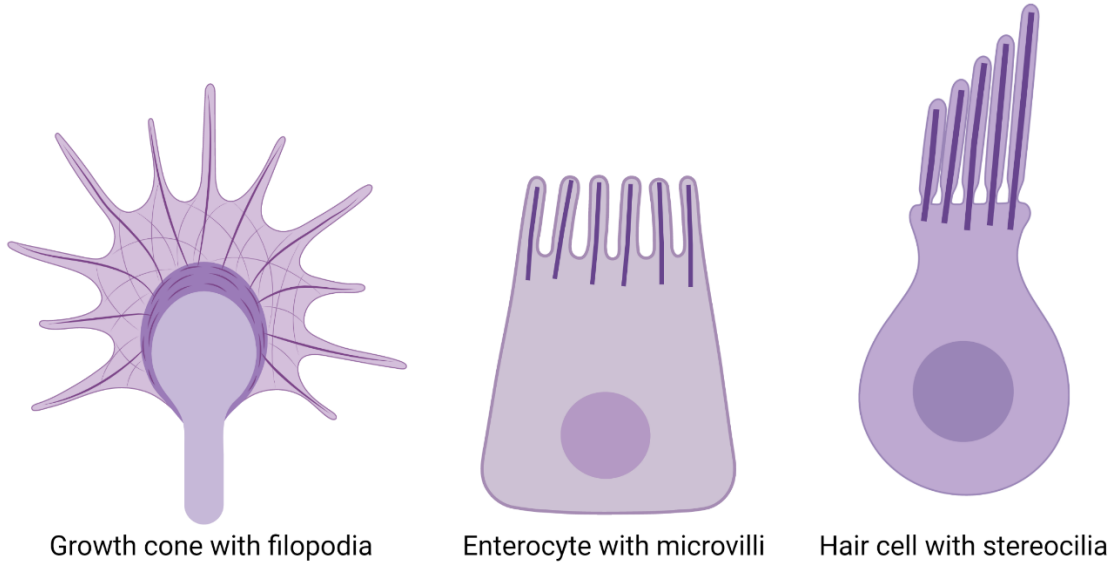


Figure 1-2: Types of cellular actin-based protrusions

Filopodia

Filopodia are highly dynamic, thin plasma membrane protrusions that are generally considered a way for the cell to probe and investigate the surrounding environment [20]. They are typically somewhat transient and may rapidly grow and shrink in accordance with the needs of the cell. Indeed, these thin structures are commonly seen at the leading edges of migrating cells, where they are believed to initiate motility [20]. However, filopodia have a variety of functions, including cell-cell adhesion and neuronal outgrowth. The growth of filopodia is generally considered to be dependent on myosin X, an actin-based molecular motor, a specific formin known as diaphanous 2 (Dia2), and the ENA/VASP family of proteins, which protect the barbed ends of actin filaments from being capped and thus allow for growth [21, [22, [23].

Microvilli

Microvilli are apical surface protrusions that exist on a variety of epithelial cell types. These protrusions are found in the intestines and parts of the kidney, where they increase the membrane surface area available for solute and nutrient transport. Microvilli are typically considered more permanent structures than the transient filopodia and are of matched length across a cell, ranging from 0.5 μm to 3 μm depending on the organ structure [24, [25]. Additionally, microvilli have been extremely well-characterized, with over six decades of data on microvillar ultrastructure, biochemistry, and function. An individual microvillus is approximately 100nm in diameter and contains 20-30 bundled actin filaments. Three proteins are responsible for bundling microvillar actin filaments in parallel; villin, fimbrin, and espin (Figure 1-3A) [26, [27, [28]. The core actin bundle is then linked to the overlying plasma membrane through ezrin, myosin-6, and myosin-1a (Figure 1-3B) [29, [30, [31, [32, [33]. Additionally, the barbed ends of these actin filaments are oriented towards the tips of the microvillus, which contain a “dense tip material”, termed as such due to its appearance in electron micrographs [34, [35]. This dense tip material is thought to contain a variety of proteins that play key roles in microvillar growth. Thus far, epidermal growth factor pathway substrate 8 (EPS8) and insulin receptor tyrosine kinase substrate (IRTKS) have been identified as tip localized factors in the microvillar tip complex [36].

Microvilli rarely exist as a single microvillus; rather, they form large arrays that span a cell or an entire tissue. Indeed, in addition to those proteins that help to form the internal structure of a single microvillus, a variety of factors have been identified that help microvilli form higher-ordered arrays. These include the intermicrovillar adhesion complex (IMAC) (Figure 1-3C). The IMAC consists of a tripartite complex of ANKS4B, USH1C, and Myosin-7B (MYO7B) [37, [38]. This tripartite complex interacts with CDHR2 and CDHR5, two cadherin family molecules that form heterophilic bonds that span the distance between microvilli, hence resulting in intermicrovillar adhesion [39]. Here, MYO7B is responsible for carrying other members of the IMAC out to the distal

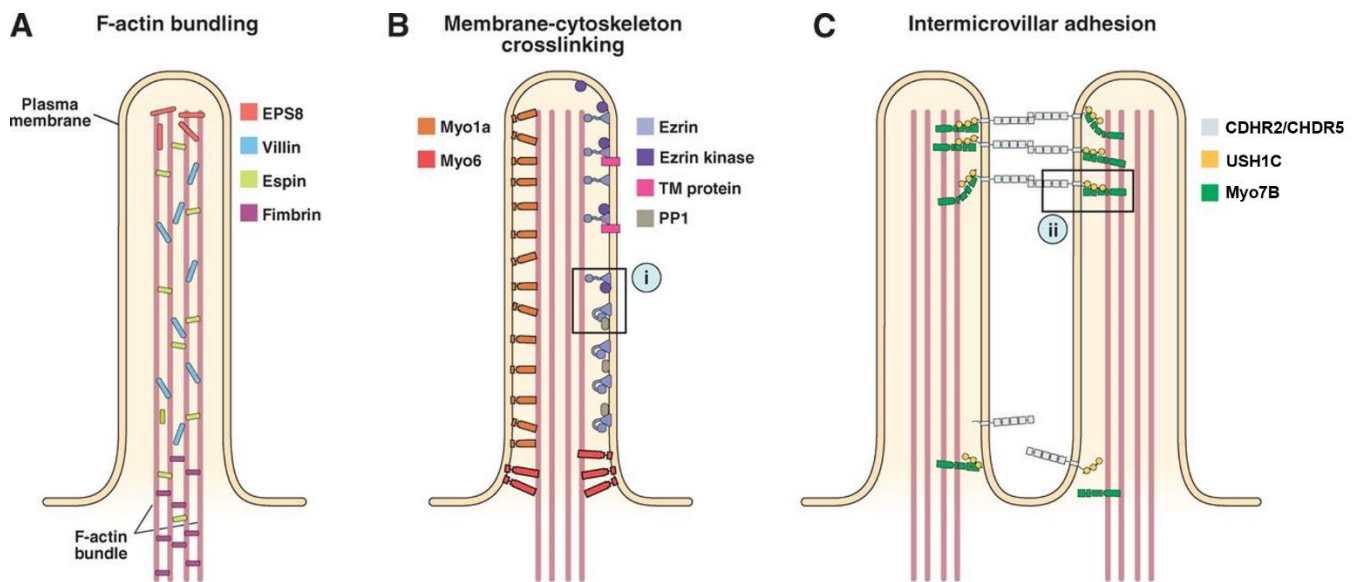


Figure 1-3: Schematic of various actin-associated proteins within microvilli. **A**, actin bundling proteins, including EPS8, which is considered to have capping and bundling properties. **B**, membrane-cytoskeletal crosslinkers. **C**, known components of the intermicrovillar adhesion complex, ANKS4B not shown. Adapted from Crawley et al., 2014.

tips of microvilli via its cargo-binding tail [38].

Additionally, a portion of the microvillar actin core is not wrapped in plasma membrane but is instead embedded in the cytoplasm. This portion of the microvillus is

typically known as the actin rootlet. Within the intestine, the rootlets are embedded in a filamentous mesh known as the terminal web [40, [41, [42]. The terminal web is known to contain spectrin, and early electron micrographs identified that a myosin-2 appearing to span microvillar rootlets [34, [40, [43, [44, [45, [46, [47]. This region is defined by both the presence of a filament network and by the exclusion of organelles. Indeed, the terminal web has also been referred to as the “zone of exclusion” [41]. A well-defined terminal web does appear to be unique to the mammalian intestine, as kidney epithelial cells that present with apical microvilli do not appear to have the same structure underlying the apical membrane [42].

The formation of microvilli has been somewhat unclear until recently. Early on, it was postulated that membrane deformation was a physical force that must be overcome by an epithelial cell to form microvilli. The ability of a cell to resist membrane deformation is determined by three factors, membrane bending stiffness, surface tension, and any present membrane cytoskeleton adhesions, which have associated energy. Recent work has revealed that EPS8 is enriched in discrete puncta at sites of new microvillar growth. It is only after this initial enrichment of EPS8 that microvilli emerge and overcome the force of the plasma membrane to become a membrane-wrapped protrusion [48]. These nascent microvilli also present with an early enrichment of IRTKS. As the core microvillar actin bundle elongates, the microvillus becomes encapsulated in the membrane [48], suggesting that the force of actin polymerization within the bundle provides the force required to deform the membrane, as would be expected based on work done in other systems [49, [50]. In vitro biophysical assays have demonstrated that actin polymerization is capable of producing forces in the pN

range [51], which would be sufficient to drive membrane deformation and, thus, microvillar elongation. However, if a newly formed microvillus loses its tip localized EPS8 puncta, these nascent protrusions are not yet stable and will rapidly shorten and disappear back into the cell [48]. Thus, nascent microvilli rely on several proteins for initiation and elongation.

Cells with microvilli typically present with dense, well-packed arrays. However, microvilli emerge as single protrusions and must cluster to develop into the dense arrays seen on the apical surface of mature epithelial cells. Immature epithelial cells demonstrate actin-driven microvillar motility, which allows for single microvilli to form larger clusters, and eventually, densely packed arrays that cover the entire surface of the cell [52].

Stereocilia

Stereocilia are typically considered to be microvillus derivatives and are found only on the surface of the sensory epithelial cells of the cochlear and vestibular systems [53]. While microvilli are typically matched in height, stereocilia form several graded rows that vary in height and are organized from the shortest rows near the center of the cells to the tallest rows closer to the edge of the cell [53]. Stereocilia are μ and are directly responsible for hearing and balance. Depending on the location within the inner ear, stereocilia can range from 1 μm to 100 μm in length and are composed of bundles of hundreds of actin filaments [54, [55]. Similar to microvilli, stereocilia have an actin rootlet that is embedded in the cytoplasm. Indeed, the rootlets of stereocilia are embedded in the cuticular plate, a dense meshwork similar to the terminal web [54].

Here, it has been identified that tropomyosin [56], TRIOBP [57], spectrin [56], and α -actinin [58] crosslink the stereocilia actin rootlets.

In order for stereocilia to be functional, they must be able to fulfill their mechanotransductive role. Indeed, the physical force produced by sound, head movement, or gravity are all converted into electric signals received by the brain due to the deflection of stereocilia [59]. The tallest row of stereocilia is anchored in the tectorial membrane and are deflected backward by physical force. This tension is transferred through a tip link connecting to the next row of shorter stereocilia [59]. Similar to the IMAC, the tip link of stereocilia is formed by a heterophilic complex of cadherin-23 and protocadherin-15 (PCDH15) [60]. PCDH15 then interacts with TMC1 and TMC2, which have been identified as components of the mechano-electrical transduction channel (MET), which allow for an electrical signal to be transmitted through the cochlear nerve [60].

Stereocilia are considered extremely stable, and once they are damaged (by excessive noise, etc.), they cannot be repaired to their original, fully functional state [54]. It is currently understood that stereocilia have a variety of proteins localized to their tips, including EPS8, USH1C, SANS, and myosin-7a (MYO7A) [54]. Additionally, it is currently thought that actin only turns over at the distal tips of stereocilia.

MOLECULAR MOTORS

In addition to the three filaments that form the most basic structural units of the cytoskeleton, a variety of molecular motors use microtubules and actin as “tracks” for delivering cargo, transduce force, and shape cellular morphology [9]. The defining feature of all molecular motors is that they convert chemical energy to mechanical

energy via ATP hydrolysis [61]. There are three broad families of molecular motors: myosins, kinesins, and dynein. The kinesin and dynein family of motors both bind to microtubules and are primarily viewed as ideal for long-distance cargo transport within the cell. However, kinesin, in particular, encompasses a large superfamily of motors, which have many different functions. Unfortunately, we will not discuss kinesin or dynein further and will instead focus in detail on the only molecular motor that is associated with actin; myosin.

Myosin super-family

The myosin super-family is highly evolutionary conserved and diversified very early on in eukaryotic evolution (Figure 1-4) [62]. Only a few taxonomic groups, such as red algae, exist without myosin. Higher-order mammals have up to 40 different unique myosin genes, and plants contain unique myosins as well. Collectively, there are 31 classes of myosin, with many classes containing a variety of myosins within them [62]. Indeed, as one might expect within a diverse superfamily of proteins, myosins participate in a wide variety of cellular processes, including but not limited to cytokinesis, cell polarization, transcriptional regulation, muscle contraction, and intracellular transport [9].

The myosin superfamily is further subdivided into “conventional” and “unconventional” myosins. The vast majority of myosins are classified as unconventional myosins, with myosin 2 (M2) being considered a conventional myosin [63]. The reasoning for this is primarily historical—M2 was the first motor protein ever identified [64] and assumed to be standard for actin-bound motors. Advances in the field later demonstrated that this was not the case, but the naming nomenclature remains to

this

day.

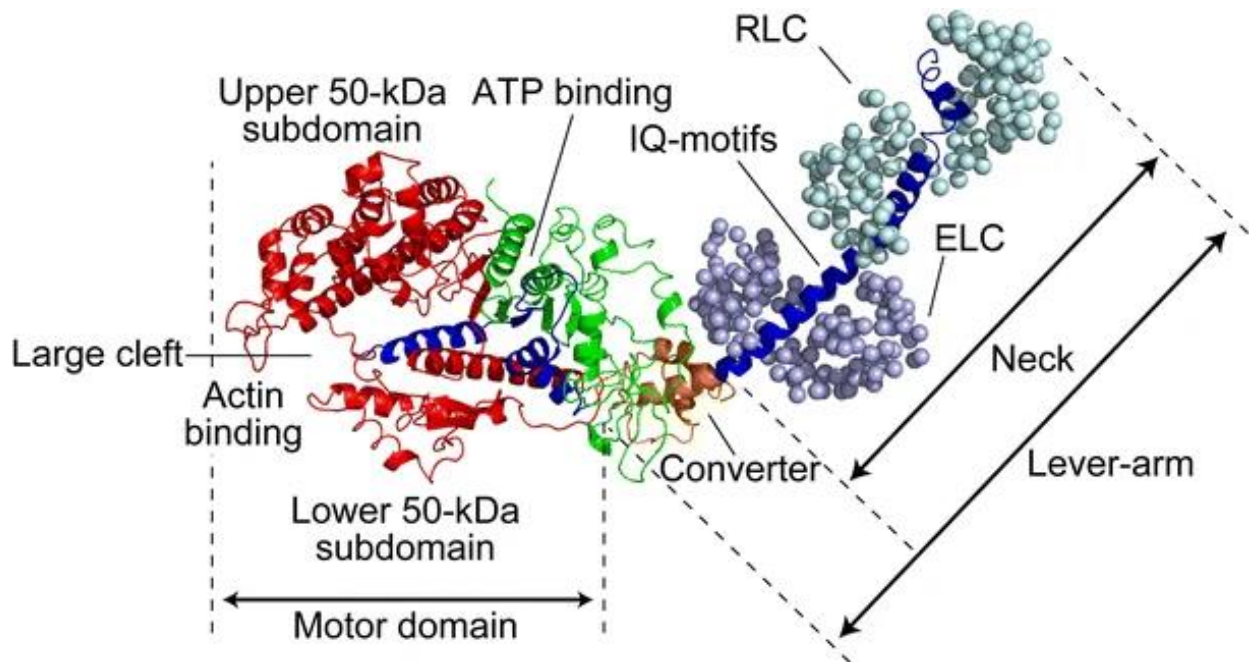


Figure 1-5: Crystal structure of conserved myosin head region. This includes the motor domain, which contains the actin binding and ATP binding sites. Also noted here is the converter, and neck, with contains IQ-motifs, and bound regulatory light chain (RLC) and essential light chain (ELC). This structure was resolved using myosin 2 S1. from Kodera and Ando, 2014 [5].

Despite the many classes of myosins that have been described, they all share three well-defined features [66]. All myosins have a highly conserved N-terminal motor domain, which contains an actin-binding domain, and an ATPase binding domain (Figure 1-5). This motor domain undergoes conformational changes upon nucleotide binding, ATP hydrolysis, and product release, in a cycle known as the myosin crossbridge cycle [67](Figure 1-6). This cycle begins with ADP-Pi-bound myosin, which is in a “loaded” confirmation and ready to bind to actin. In this state, the myosin head can loosely bind to actin. Upon Pi release, the myosin head rotates in a movement called a “powerstroke”. After which the ADP is released, and myosin is in a strongly bound state. The binding of a new ATP molecule releases the motor from the actin filament, and the hydrolyzing of ATP to ADP-Pi causes the motor head to rotate back to it’s original “loaded” confirmation. This cycle of conformational changes allow for myosin

motility and force transduction. Then, all myosins contain a central neck region, which acts as a lever arm for force transduction and has several binding spots for light chains. The amount of light chain binding regions can vary greatly between myosins. Furthermore, depending on the myosin species, a consensus IQ motif sequence of IQXXXRGXXRK can bind essential (ELC) or regulatory light chains (RLC) or calmodulin (CaM) or CaM-like molecules [68, [69](Figure 1-5). Many of these light chains are sensitive to calcium-binding or phosphorylation state, which serves to regulate myosin activity. Additionally, this neck region can also contain coiled-coil domains that mediate dimerization. Finally, all myosins contain a C-terminal tail. Depending on the myosin species, this tail may mediate cargo interactions, autoinhibition, or further regulate the activity and localization of the myosin molecule [70].

While there are many myosin species with a wide variety of functions, for the purposes of this introduction, we will further focus on myosin-2, the conventional myosin class.

Myosin-2

Myosin-2 was the first motor protein ever discovered—muscle myosin-2 was identified in muscle extracts in 1864 [64]. Despite almost two centuries of work on M2, a considerable amount of ongoing research is focused on M2. A functional class 2 myosin is, in fact, a hexameric molecule consisting of two heavy chains, two essential light chains, and two regulatory light chains (Figure 1-7). The heavy chain of M2 is encoded by a myosin gene and consists of an N-terminal motor domain, a neck region containing

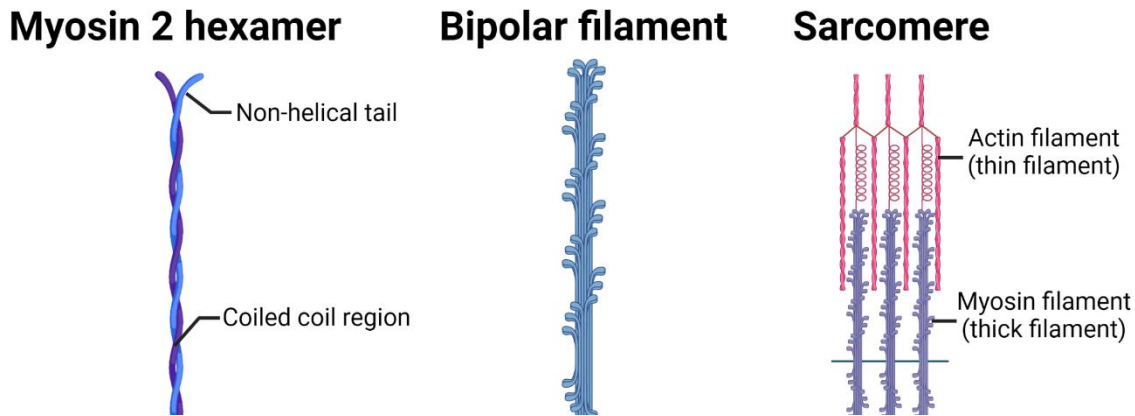


Figure 1-6: Graphical depiction of the myosin crossbridge cycle. This cycle allows for the motor to exert force on anchored actin filaments or move in a processive manner

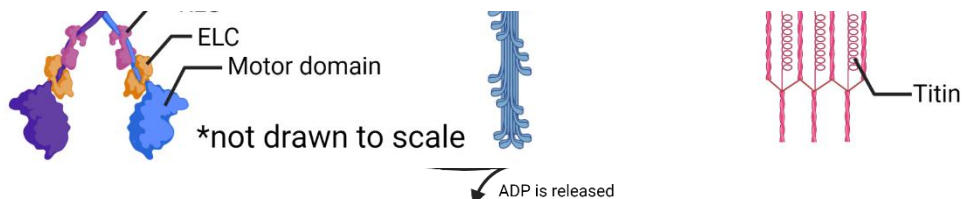


Figure 1-7: Schematic of various forms of myosin 2. The myosin 2 hexamer consists of two heavy chains, two ELCs and two ERLCs. Collectively, myosin 2 hexamers can form bipolar filaments via interactions between the coiled coil region of each hexamer. Myosin 2 also forms the thick filaments of sarcomeres, the fundamental unit of muscle contraction.

binding regions for an essential and a regulatory light chain, followed by a long coil coiled region that ends in a short non-helical C-terminal tail. The long coiled-coil of an M2 heavy chain allows for multimerization, which enables M2 to form bipolar “thick filaments” [71, [72] (Figure 1-7). A thick filament is the fundamental unit of contractile force in biology. The C-terminal tail of class 2 myosins is thought to play a role in thick filament assemble and intracellular localization of M2 [72].

The activity of M2 is primarily regulated by RLC phosphorylation on two residues: Ser19 and Thr18 [73]. It has been demonstrated in vitro that these phosphorylation events increase the total actin-activated Mg^{2+} -ATPase activity of M2 isoforms. It has also been demonstrated that phosphorylation of the RLC regulates the assembly of M2 thick filaments via a head-tail interaction that occurs in the unphosphorylated state. A variety of kinases have been found to phosphorylate M2 RLC, including myosin light chain kinase (MLCK), Rho-associated coiled coil-containing kinase (ROCK), leucine zipper interacting kinase (ZIPK), citron kinase, and myotonic dystrophy kinase-related CDC42-binding kinase (MRCK) [73]. MLCK only associates with M2 RLC, whereas other kinases, such as ROCK, phosphorylate a variety of other substrates. Indeed, ROCK primarily inhibits phosphatase protein phosphatase 1 (PP1), which dephosphorylates M2, despite its ability to phosphorylate RLCs directly. Interestingly, kinases that phosphorylate RLCs are often differentially localized throughout the cell (i.e., MLCK is often more peripheral, and ROCK more central), which means that actomyosin structures within the cell may exhibit different levels of stability and sensitivity depending on their localization [73]. Class 2 myosins can be further regulated by phosphorylation sites in their coiled-coil domain and non-helical tails [72].

Class 2 myosins constitute a large class, with 14 M2 heavy chains found in the human genome [74, [75]. 10 of these are found in cardiac or skeletal muscle and form large arrays called sarcomeres, which are responsible for skeletal and cardiac muscle contraction. A sarcomere is a unit of two actin filaments running parallel on either side of a myosin bipolar filament. Sarcomeres are anchored by Z lines at either end. Outside of skeletal and cardiac muscle M2s, there is one gene that encodes for smooth M2 (SM2), MYH11. Unlike all other M2s, SM2 is capable of forming unipolar filaments and is found in the muscle of all hollow organs aside from the heart. Finally, there are three known paralogs of non-muscle myosin-2 (NM2): NM2A (encoded by MYH9), NM2B (encoded by MYH10), and NM2C (encoded by MYH14) [76, [77]. Unlike the name suggests, NM2s are ubiquitously expressed in nearly all cell types, including muscle cells. NM2 paralogs have distinct kinetic properties, which allow these motors to perform specific and distinct functions at the cell and tissue scale, including cytokinesis, cell motility, collective cell migration, and regulating the paracellular permeability of epithelial sheets [1]. In the context of in vitro sliding filament assays, tail-less NM2C heavy meromyosin (HMM) fragments move actin filaments at $\sim 0.05 \mu\text{m/s}$, slower than both NM2B ($\sim 0.08 \mu\text{m/s}$) and NM2A ($\sim 0.29 \mu\text{m/s}$). Bipolar filaments assembled by NM2C ($\sim 293 \text{ nm}$) tend to be shorter than those assembled by NM2B ($\sim 323 \text{ nm}$) or NM2A ($\sim 301 \text{ nm}$) (Figure 1-8). Filaments composed of NM2C also contain fewer molecules than those assembled by NM2A and NM2B, resulting in thinner structures ($\sim 8 \text{ nm}$ vs. $\sim 11 \text{ nm}$ wide) and presumably a lower potential for generating force. The NM2 paralogs are also capable of forming co-assemblies of two or more paralogs within the same minifilament [78, [79].

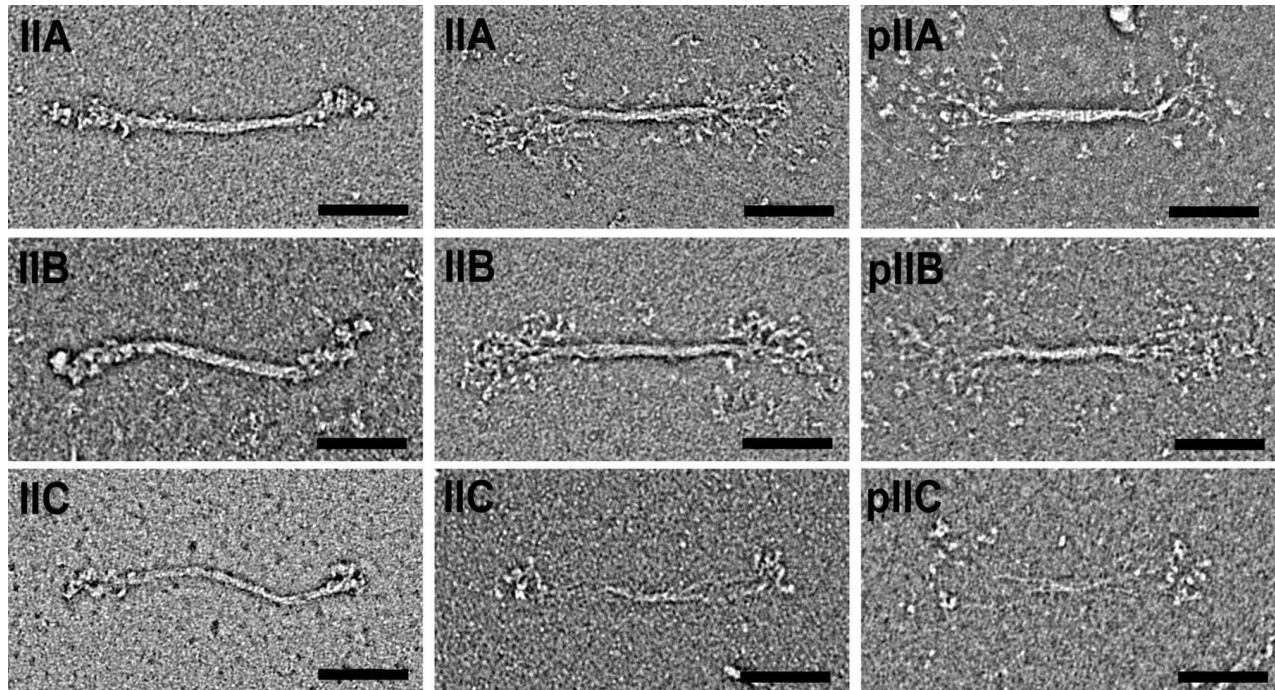


Figure 1-8: Negative stain electron microscopy of all three non-muscle myosin filaments. The first two columns show unphosphorylated filaments in the absence of ATP. The last column shows filaments with phosphorylated RLCs. Adapted from Billington et al., 2013 [1].

There exists a significant body of work dedicated to the biological function of NM2A and NM2B. Both paralogs have been implicated in cell migration, the formation of filopodia, and the formation of basal focal adhesions. NM2 also seems to play a role in the cellular response to external forces. Furthermore, NM2 is implicated in both the formation and the stability of cell-cell junctions and the organization of three-dimensional epithelial tissues. Finally, NM2 is required for cell division. Given the vast biological roles for NM2, it is no surprise that mutations in NM2A and NM2B are associated with disease. Indeed, NM2A knockout (KO) mice fail to form a visceral endoderm and are embryonic lethal at day 6.5, prior to organ formation [80, [81]. Conversely, NM2B KO mice survive to E14.5, at which point they exhibit cardiac and

brain defects [81]. However, unlike NM2A and NM2B, little literature has explored the role of NM2C. NM2C is one of the most recent myosins to be identified, have been discovering in 2004 after the completion of the human genome project [82]. Interestingly, NM2C is expressed in a more tissue-specific pattern than NM2A or NM2B [6]. NM2C is only found in high levels in parts of the brain, the cochlea, and the intestine. Of the limited work that has been done on NM2C, it has been found that it localizes to cell-cell junctions of the hair cells of the inner ear and the small intestine [83]. Indeed, it was determined that contraction and relaxation of these junctional bands of NM2C results in changes in apical cell shape and tissue geometry [84]. Additionally, there are a handful of mutations in NM2C that have been identified, most of which are associated with autosomal dominant non-syndromic hearing loss (DFNA4A) [85, [86, [87, [88, [89, [90, [91, [92, [93, [94].

ROLE OF CONTRACTILE FORCE IN BIOLOGY

The discovery of M2 and subsequent decades of study on class 2 myosins have allowed for an incredibly thorough investigation of the role of contractile force in biological systems, using a variety of techniques include computer-based modeling, in vitro biochemistry, and in vivo model organism studies. Class-2 myosins are the classical producer of biological contractile force [95], and NM2 paralogs, in particular, play a wide variety of roles by providing contractile force on an intracellular scale [77, [96, [97, [98, [99, [100], which can then be propagated throughout a tissue or organ. Indeed, D’Arcy Thompson first proposed that an organism’s form, aka shape, is a “diagram of the forces” that have acted upon it in his 1917 book *On Growth and Form* [101]. A century ago, what these forces could be was unknown. Today, a variety of forces that shape life itself have been described, including those that influence cell

shape and tissue morphogenesis [102]. Myosin motor activity is not necessarily required to produce contractile force; however, the myosin motor itself is usually still involved. The classical model of contractile force relies on M2 thick filaments in sarcomeres, which undergo ATP hydrolysis to exert force on actin filaments. The motor activity-independent contractile force pathway relies on motors or other actin-associated proteins as crosslinkers [103]. In this model, the depolymerization of anchored actin filaments drives contraction. In vivo, it is often difficult to determine if the motor activity of myosin is required for contraction, as many techniques to disrupt myosin can affect both motor activity and any potential crosslinking activity [102]. Regardless of the method of myosin involvement, the importance of contractile force in biological systems is well-established.

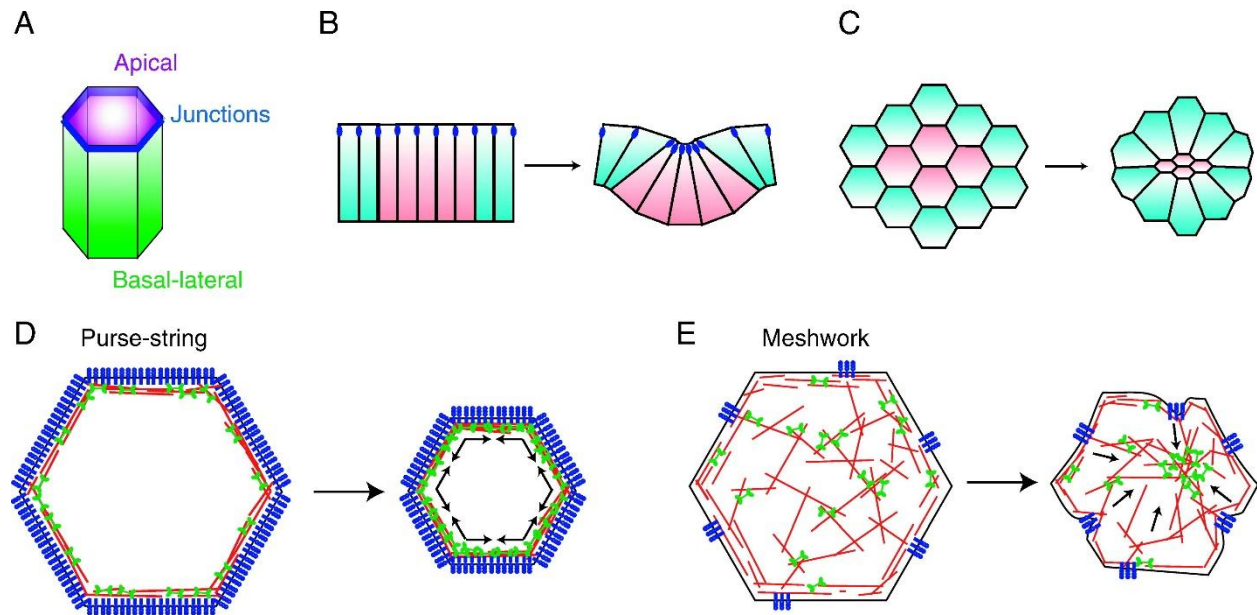
Cell shape

Simply put, the cell surface is under tension. However, this is unlike the surface tension in liquids, which is caused by the cohesive nature of the molecules which make up the liquid, in which the molecules within the bulk of the liquid exert an attractive force on the surface molecules, which results in the liquid assuming a shape with the least surface area. Instead, cellular tension (not the surface tension of the plasma membrane) is generated thanks to an actomyosin network at the cell cortex. Cell-cell adhesion, osmotic pressure, and myosin activity can all change relative cortical tension [104].

While the contraction of striated muscle depends on sarcomeres, organized antiparallel f-actin filaments with a bipolar myosin filament in the center, more unstructured networks are also capable of contractile activity [105, [106]. These

unstructured networks are thought to be the basis of how smooth muscle and non-muscle cells contract. However, some model systems, such as the ventral furrow cells of *Drosophila* embryos, have organized, sarcomere-like structures that are arranged radially, and if this structure is disrupted, apical contraction is inhibited [107]. The ability of a cell to carefully use contractile force is key for cell division, cell migration, and wound healing.

In particular, many cells contain an actomyosin junctional belt, which is critical for



maintaining cell-cell junctions [108, [109, [110] (Figure 1-9A). Contraction in the junctional belt can alter the apical shape and area of a single cell, and this change can

Figure 1-9: Mechanisms of cell shape change. **A**, schematic of the polarized organization of an epithelial cell. **B**, apical–basal cross-section of cells undergoing apical constriction. Apical constriction facilitates the bending/folding of epithelia by causing cells to adopt a wedge shape. **C**, apical surface view of apical constriction. Apical constriction pulls neighboring cells inward, suggesting that contractile forces generate tension in constricting cells. **D**, the purse-string model of apical constriction. Contractile force generated by myosin-II-driven actin filament sliding within the circumferential cable constricts the cell apex. Forces are generated parallel to the cell surface. **E**, The meshwork model of apical constriction. Myosin II contracts a two-dimensional actin meshwork that spans the apical cortex of the cell. Forces generated perpendicular to the cell surface pull discrete adherens junction sites inward to constrict the cell. Reprinted from *Developmental Biology*, Volume 341, Martin, A.C, Pulsation, and stabilization: Contractile forces that underlie morphogenesis, Pages 114-12., Copyright 2010, with permission from Elsevier.

be propagated to shape changes within an entire epithelial sheet [105, [106, [111](Figure 1-9B and 1-9C). But perhaps the most well-known example of contraction on a cellular scale is cytokinesis. Following completion of mitosis, a dividing cell must physically split into two daughter cells. This physical separation is done via a contractile ring that assembles directly underneath the plasma membrane [112, [113, [114, [115]. This carefully regulated process is key for the development and maintenance of all organisms, from yeast to humans.

Tissue morphogenesis

Contractile force can influence the shape and movement of singular cells and also plays a critical role in shaping epithelial sheets, and thus, shaping organs. The contractile or tensile forces generated by the actomyosin network within a single cell can be transmitted between cells in a sheet via cell-cell junctions or the extracellular matrix [83, [109, [116, [117]. For example, the apical constriction of a columnar epithelial cell results in a cone or wedge-shaped cell, which then facilitates a bending or folding of the epithelial sheet as this shape change is propagated through the sheet (Figure 1-9B and 1-9C). This type of apical constriction has been observed to happen due to a variety of actomyosin networks. During neural tube closure in vertebrates, a circumferential actin belt associated with the adherens junction contracts the cell apex in a “purse-string” manner (Figure 1-9D) [105]. However, during mesoderm invagination in *Drosophila*, myosin localized to the entire apical surface of the cell, like a meshwork (Figure 1-9E) [106]. This meshwork undergoes contractile pulses, which result in apical constriction, just as in the case of neural tube closure. It is unclear why these various mechanisms exist and why some morphological events use different manners of actomyosin contractile force. Actomyosin contraction also has a well-defined role in

convergent-extension in a variety of model systems and organs [84]. [118] Thus, it is certainly safe to say that morphogenesis and development rely greatly on those contractile forces generated from actomyosin architectures.

THE GASTROINTESTINAL TRACT

Mammals contain a variety of polarized epithelial surfaces, which provide a barrier between inside and outside worlds and serve as the first line of defense against physical, chemical, and biological hazards. In order for any substance to enter the body, it must first pass through an epithelial sheet. The largest epithelial sheet is the skin that lines the body, the second largest is the gastrointestinal tract, which is our focus for this dissertation. The gastrointestinal (GI) tract consists of the mouth, the pharynx, the esophagus, the stomach, the small intestine, and the large intestine, rectum, and anus. While all of these organs are lined with polarized epithelial cells, we shall only discuss the small intestine in detail, although it shares many features with the large intestine. The small intestine is a hollow organ lined with a single layer of solute transporting epithelial cells [119]. Underlying the epithelium is the lamina propria, composed of loose connective tissues. This is followed by the submucosa, which is formed out of dense, connective tissues and contains large blood vessels and components of the enteric nervous system. Lastly, the small intestine has an external smooth muscle layer, which plays an important role in morphogenesis and homeostasis. [119]

The small intestine can be further separated into three distinct segments: duodenum, jejunum, and ileum. The most proximal segment is the duodenum which connects directly to the stomach and helps to further digest food coming from the stomach, as well as beginning to absorb nutrients from digested substances. In

humans, the duodenum is the shortest part of the small intestine at approximately 25-38cm long. Directly after the duodenum is the jejunum, which is responsible for the bulk of nutrient absorption—this includes passive and active transport through the epithelial sheet. In humans, the jejunum is approximately 2.5m long. The most distal segment of the small intestine is the ileum, which is approximately 2-4m long in humans. The ileum serves to absorb any products of digestion that were not previously absorbed in the jejunum, as well as vitamin B₁₂ and bile salts [119]. Many severe intestinal ailments, such as Crohn's disease and Celiac disease, have a more substantial phenotype in the ileum [120, [121].

The morphology of the mature small intestine makes it one of the most architecturally complex organs. Broadly, the small intestine has two morphologically separate domains—the crypts and the villi. Villi are long finger-like protrusions that serve to increase the surface area available for nutrient absorption significantly [122] (Figure 1-10A). The crypts of Lieberkühn, first described in the 1700s, contain LGR5+ stem cells, which remain actively proliferative throughout an organism's lifespan [123, [124]. As the LGR5+ stem cells differentiate, they migrate out of the crypt, up the villi, and finally undergo apoptosis and shed off at the tips [123] (Figure 1-10B). This process of crypt to villus migration is critical for intestinal homeostasis and regenerative renewal of the epithelium. Additionally, the constant turnover of cells resulting from crypt to villus migration enables the intestine to remain a dynamic organ, which is vital for its function [125].

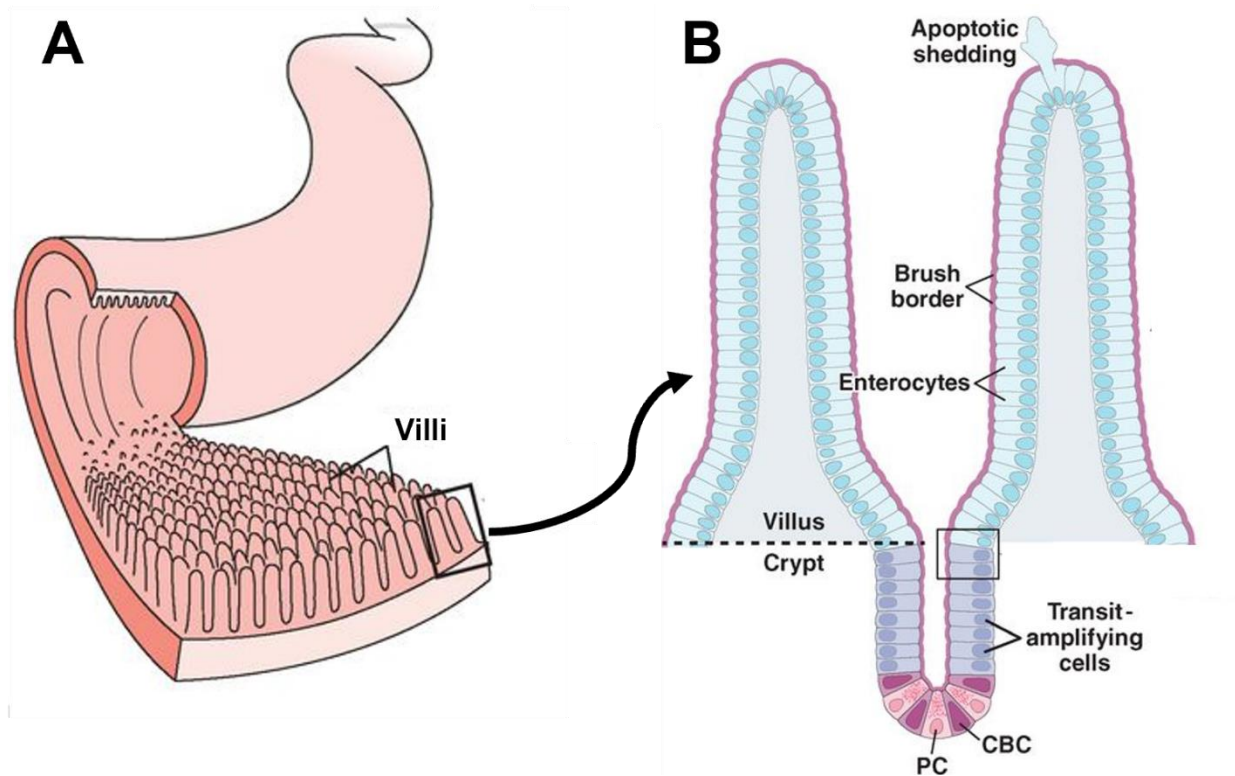


Figure 1-10: Cartoon of the structure and morphology of the small intestine. A, the small intestine is covered in fold of tissue called villi. **B,** villi are primarily lined with enterocytes, with differentiation in the crypts, migrate up the villus, and shed off at the top via apoptosis. Adapted from Crawley et al., 2014 [2].

Development and morphogenesis

During embryogenesis, the GI system is one of the first to polarize. The early gut tube develops after the three primary germ layers are specified during gastrulation. The gut tube develops from the endoderm and forms along the anterior-posterior axis of the embryo. The anterior endoderm is responsible for the formation of the foregut, which eventually develops into the portion of the GI tract that stretches from the mouth to the duodenum. The posterior endoderm forms the hindgut, which consists of the distal third of the colon to the rectum, and the endoderm between the anterior and posterior poles forms the remaining midgut. The splanchnic mesoderm goes on to form the mesenchyme around the gut tube. This mesenchyme later forms a variety of cell types and the smooth muscle walls along the outside of the small intestine [126].

In the chicken, the gut tube maintains a smooth luminal surface until embryonic day 7 (E7). However, it is at this point that the outer mesenchyme begins to differentiate into two layers of smooth muscle; the first one with the contractile axis oriented circumferentially and finishes differentiating by E13. It is at this point that the other smooth muscle layer, with the contractile axis oriented longitudinally, begins to differentiate [127]. This sequential differentiation of smooth muscle layers is critical for the formation of villi. From E8-12, ridges emerge as the circumferential muscle layer emerges and begins to contract the epithelial surface. From E13-15, the formation of the longitudinal muscle layer, the previous ridges transform into a zigzag. And finally, as the longitudinal muscle continues to develop and contract, villi are formed from the zigzags. In this manner, the morphology of the intestinal epithelium emerges as a consequence of elastic energy minimization during the constrained growth of the endoderm [127]. The endoderm then differentiates into the various epithelial cell types that populate the intestine. Interestingly, villi become shorter when you move proximal to distal in the intestine; the developmental mechanisms for these structural differences are not currently understood.

Unlike villi which develop during embryogenesis, crypts develop post-natal as a result of myosin-2 apical constriction in the "intervillar region" [128]. A Rac1 signaling pathway results in the compartmentalization of crypts and villi. Rac1 activity continues to be high in adult crypts. While the intervillar cells are specified around E15.5, crypt morphogenesis occurs between postnatal day 2 (P2) and P10. Beginning at P0, the apical area of the intervillar cells begins to constrict significantly, corresponding with an increase in the expression of contractility-related genes [128]. Interestingly, during this

process, the mean number of cells within the intervillar region remains constant, which indicates that cell proliferation does not drive the process of crypt morphogenesis. After invagination of the intervillar regions is initiated via apical constriction, hinges are formed from cells that are basally constricted and apically expanded. These hinge regions are initially formed from P3 to P5; however, changes in cell shape do not occur until P6. These regions serve to morphologically separate the crypts from the villi. Once the invagination of the tissue behind and the hinge regions are formed, the crypts continue to elongate until approximately P10 [128]. After this point, the complex morphology of the intestine is consistent, although it can change due to feeding behaviors, disease/infection, and age.

Crypt-villus migration and differentiation

Intestinal crypts are one of the few stem cell niches that remain active throughout an organism's lifespan [123]. This is due to the fact that the integrity of the intestinal epithelium depends on a process of regenerative renewal, in which new cells continuously differentiate, migrate out of the crypts, replacing old, damaged cells that are shed off at the tips of villi. These new cells will continue to migrate up the villus until they too are shed off, in a process known as crypt-villus migration. Indeed, due to this continuous migration, the entire intestinal epithelium is turned over in the course of a week in humans. It is partially due to this continuous cycle of division, differentiation, and migration that the cancers in the GI tract are some of the most common [129]. However, this regenerative renewal is also critical for repairing the intestinal barrier after disease or infection [130].

For decades, it was assumed that mitotic pressure from the dividing cells in the crypts was the driving force behind crypt-villus migration. However, it was recently demonstrated that crypt-villus migration continues even in animals that have been given hydroxyurea (HU), an S-phase inhibitor that inhibits mitosis at low doses [131]. It was found that mitotic pressure does play a role in the crypts and lower villus region, but not beyond. In this same study, they also demonstrated that Arp2/3 dependent basal protrusions, similar to lamellipodia, are required for crypt-villus migration to occur [131]. Thus, it is now thought that active cell migration is key for homeostatic renewal of the intestinal epithelium,

The population of cells in the intestinal crypts is also important. At the base of the crypts sits a population of LGR5+ stem cells. This population was originally known as crypt base columnar (CBC) cells. Further up the crypt, there is a population of transit-amplifying (TA) cells, which divide faster than the LGR5+ stem cells.

Differentiation into the various cell types of the intestine epithelium begins at the 5+ position—there are two primary intestinal cell fate pathways, absorptive and secretory [123] (Figure 1-11). These pathways can give rise to a variety of cell types, which will be individually discussed below [132, [133].

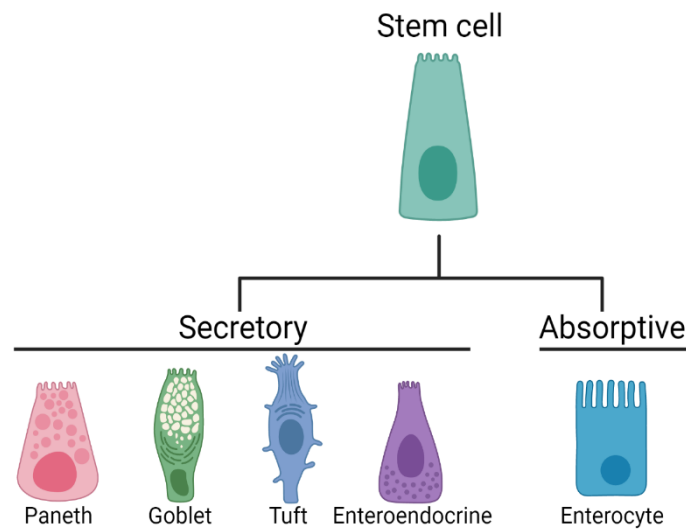


Figure 1-11: schematic of the various types of intestinal epithelial cells.

Enterocytes

Enterocytes make up the majority of the cells within the intestine, and indeed, are considered the “default” cell differentiation pathway within the small intestine. They are one of the only nutrient-absorbing cells in the body, and their ability to function is critical for maintaining homeostasis. Enterocytes are characterized by their well-packed array of apical microvilli, which collectively form the brush border. The brush border is immature on enterocytes in the crypts but grows increasingly dense as cells move out of the crypts until finally covering the entire apical surface of villus enterocytes [2].

Paneth cells

Paneth cells arise from the secretory progenitor cells, and unlike all other intestinal epithelial cells, they migrate down to the base of the crypt after differentiation instead of up onto the villus. Paneth cells are also long-lived compared to others in the intestine; a single Paneth cell may persist for up to a month, while most intestinal epithelial cells turn over within a few days. This specialized cell type was first described in the late 1800s, where they were noted for prominent eosinophilic granules in their cytoplasm. It is now understood that those granules contain antimicrobial peptides such as lysozyme, as well as proteins that help to modulate the microbiota of the intestine. Paneth cells are primarily found in the distal portion of the small intestine, which has made them somewhat difficult to study. The antimicrobial peptides secreted by Paneth cells are a critical part of host defense, as the stem cells in the crypt are particularly vulnerable points for pathogen invasion [134].

Goblet cells

Goblet cells are the primary secretory cells of the intestinal epithelium and are responsible for the maintenance of a mucus layer that forms over the single layer of epithelial cells that make up the intestinal mucosa. Goblet cells secrete mucins, primarily MUC2, in the small intestine. These mucins form a physical barrier to keep commensal bacteria and other microbes separate from the epithelial cells. A breach of the mucus layer can result in inflammation, even if only commensal microbes are present. Thus, goblet cells play a key role in the maintenance of the intestinal barrier and thus homeostasis. Goblet cells are upregulated during periods of infection, as these cells are an essential part of the adaptive immune response [134].

Tuft cells

Tuft cells are incredibly rare within the epithelium and can be easily identified by the mega-microvilli, present on their apical surface, which are longer and have a wider diameter than microvilli present on enterocytes. Tuft cell microvilli also have massive actin rootlets that extend deep into the cytoplasm. This unique morphology allowed them to be originally identified via electron microscopy [135]. Interestingly, tuft cells express proteins similar to those in taste buds, leading them to be classified as chemosensory cells. Tuft cells were initially thought to differentiate from secretory progenitor cells. However, while all other secretory cell types are dependent on the transcription factor *Atoh1*, tuft cells can still be found in *Atoh-1* deficient animals, suggesting a different mechanism for tuft cell differentiation [136]. Due to their rarity, it has been difficult to perform detailed studies on tuft cell function and ultrastructure. However, it is known that tuft cells play a role in type 2 immunity via IL25. Primarily, tuft cells initiate a type 2 immune response upon helminth infection [137, [138]. It is also

believed that the taste receptors expressed in tuft cell microvilli allow them to sense parasites in the lumen directly [138], but further investigation is needed.

Enteroendocrine cells

Enteroendocrine cells are thought to make up about 1% of the intestinal epithelium and are derived from secretory progenitor cells. These cells are scattered through the epithelium as single cells and secrete a variety of hormones that influence enzyme secretion, GI motility, and appetite [139]. While little work currently focuses on intestinal enteroendocrine cells, they are thought to be a key player in mucosal immunity, as they can sense microbial metabolites and release cytokines in response to pathogens [140]. As the intestine is an incredibly large mucosal surface that interacts with the environment, the immune system and signaling within the gut are critical for health and homeostasis. Interestingly, despite their relative rarity in the intestinal epithelium, enteroendocrine cells form the largest endocrine system in humans [140].

Plasticity of the intestine and homeostasis

The continuous regenerative renewal of the intestine allows it to remain an incredibly plastic and dynamic organ. This plasticity can be observed at multiple scales; the length of the GI tract itself, villus length, microvillus length, and protein expression are all subject to change as a result of environmental factors. It has been well-established that villi are capable of changing their morphology; this is a homeostatic response in the case of fasting and feeding periods, and also a response that can occur as a result of infection or chronic diseases, such as Crohn's and Coeliac disease [120, [141, [142, [143, [144, [145, [146, [147, [148, [149, [150, [151]. For example, it has been shown in a variety of animal models that changes in villus length occur as a result of fasting and feeding behaviors. Villi can regain lost length in as little as two hours after refeeding

[151]. Classically, it was assumed that these changes in length occur due to increased cell shedding rate (to shorten) or increased cell proliferation rate (to lengthen). However, it was previously found that the rate of cell production did not increase until 12hrs after refeeding, suggesting that there may be additional mechanisms that allow for villus lengthening shortly after refeeding [151]. Decreased expression of many of the transporters required for nutrient absorption have also been noted [146].

The intestinal epithelium and the brush border

The brush border on enterocytes is an excellent example of how form follows function and function follows form. The brush border has two functions; it markedly increases the membrane surface area available for nutrient absorption by 9 to 16 fold and provides a line of defense against luminal pathogens [152, [153]. The microvilli that form the brush border are remarkably uniform in length and diameter (~100nm diameter and 1-3 microns in length depending on the region of the GI tract) and incredibly well packed across the entire cell (Figure 1-12A and 1-12B).

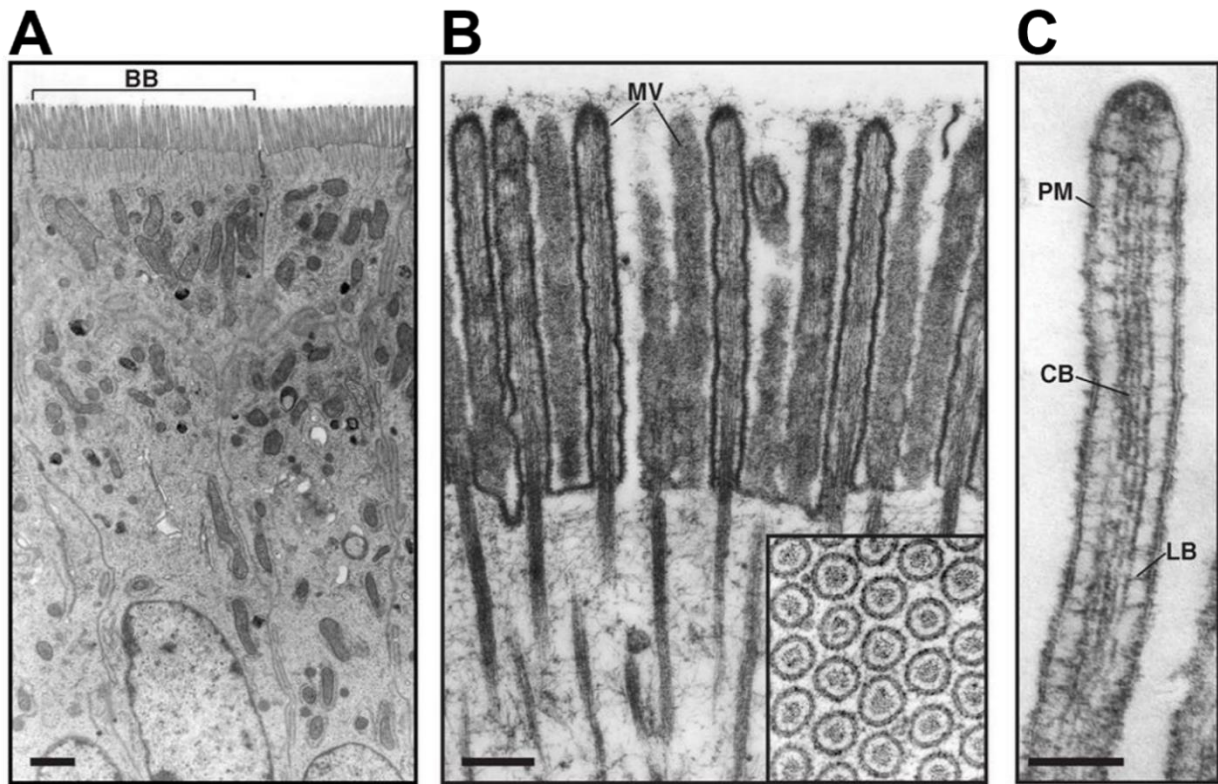


Figure 1-12: Ultrastructure of the brush border. **A**, enterocytes from mouse small intestine, brush border (BB) is noted by black bracket. **B**, brush border microvilli (MV) from chicken small intestine. Reproduced from Mooseker and Tilney (1975). The inset shows hexagonally packed microvilli in cross section. **C**, a single microvillus. Plasma membrane (PM) is linked to the core bundle (CB) by lateral bridges (LB) that are formed at least in part by myo1a. Reproduced from Mooseker and Tilney (1975). Scale bars are as follows: A=1 μm , B=0.2 μm , C= 0.1 μm . Figure adapted from Crawley et al., 2014 [2].

Brush border microvilli contain a core bundle of 20-30 actin filaments, which are connected to the plasma membrane by actin-membrane crosslinkers such as myo1a [2] (Figure 1-12C).

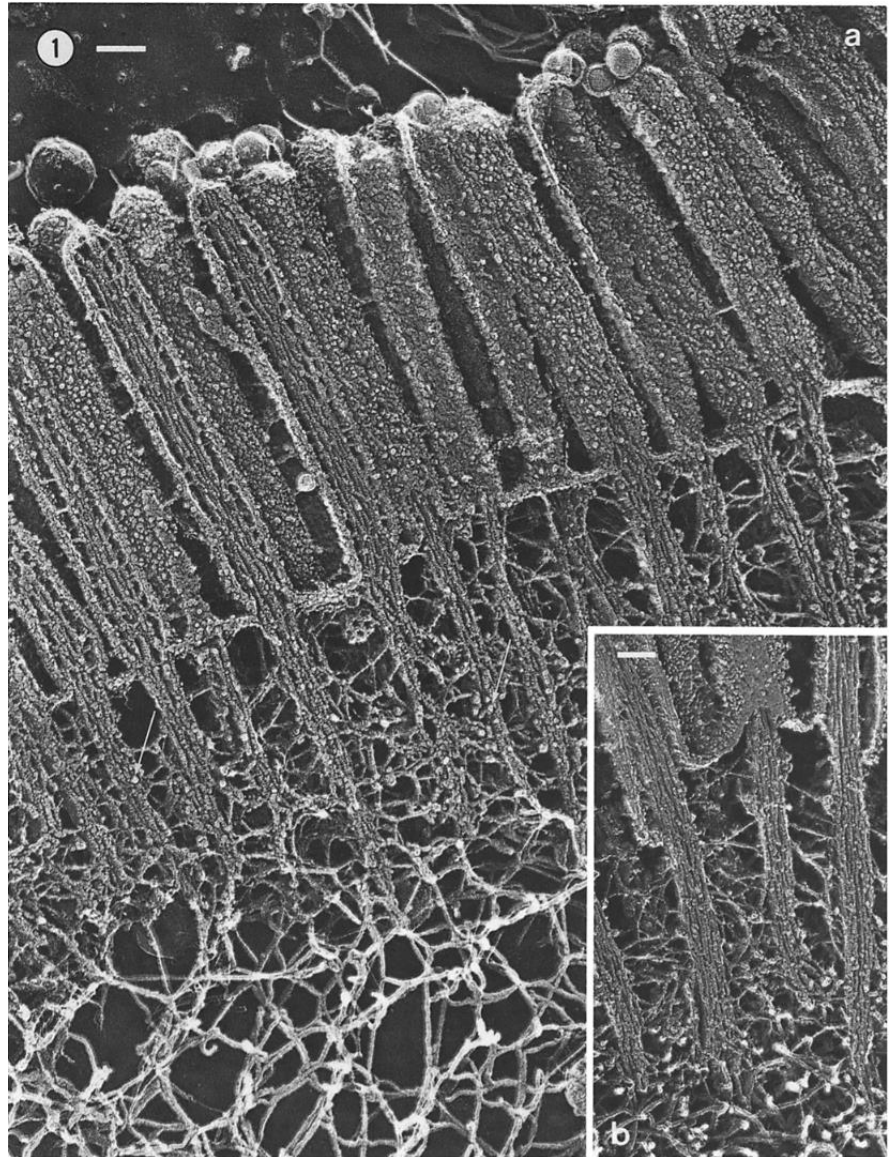
The brush border is immature in the crypts, with sparse microvilli across the cell surface. While it has been demonstrated that microvilli “surf” across the cell and will cluster with other microvilli when they interact [52], it is still unclear how these clusters of microvilli come together in an organized manner to form the brush border.

The terminal web

The pointed ends of actin bundles that form the core of the microvilli that form the brush border are anchored in a dense, filamentous network known as the terminal web (Figure 1-13). This dense meshwork appears to be somewhat unique to the small intestine, as other organs with microvilli, just as the kidney, do not have a well-defined terminal web. Incidentally, the microvilli of the kidney are not nearly as well organized at the intestinal brush border.

The terminal web was first described several decades ago in ultrastructural studies and has been called the “zone of exclusion” due to the exclusion of organelles from this region [40]. However, it has not been determined how it contributes to the apical domain structure, microvillar organization, or brush border function. Interestingly, knockout (KO) mouse models lacking major brush border structural components, such as PACSIN-2, plastin-1, or actin-bundling proteins (villin, espin, and plastin-1) exhibit significant perturbations to the terminal web [33, [154, [155, [156]. All of these models exhibit a common phenotype, where the terminal web thins and microvilli become disorganized or shortened, which further suggests that terminal web architecture and brush border morphology are intimately linked.

Previous biochemical and ultrastructural studies of the terminal web identified several components of this filamentous network, including intermediate filaments (primarily keratin) and spectrins [25, [46, [47]. Early deep-etch electron microscopy (EM) studies also identified “8 nm filaments”, which appeared to crosslink microvillar actin bundle rootlets [3]. However, these structures did not label with myosin sub-fragment 1



(S1), suggesting they were not composed of actin. Additional immunogold labeling EM data

Figure 1-13: The terminal web supports the brush border. Quick freeze deep-etch electron micrograph of the brush border and terminal web. Scale bar = 0.1 μ m. Adapted from Hirokawa et al., 1982 [3].

led to speculation that 8 nm filaments contained myosin [3]. This was further supported by immunofluorescence labeling studies that made use of a pan-myosin antibody raised against myosin-2 epitopes [43]. However, the identity of the myosin and the organization and function of 8 nm filaments in brush border structure and function have remained uninvestigated since the early 80s.

Summary

M2, the first motor protein ever described [64], operates at multiple scales in biology. Muscle M2 coordinates the large-scale movement of skeletal muscle, and NM2 plays a variety of roles in cell shape and tissue morphogenesis. While it had been previously hypothesized that an M2 isoform would play a role in the complex morphology of the intestine, little recent work had investigated M2 in the intestinal epithelium. Indeed, the intestine exhibits incredibly complex morphology, from the level of tissue to the ultrastructural level.

Previously, it was shown that M2 is required for crypt morphogenesis [128], and that NM2C localized to the apical surface of enterocytes [83]. However, NM2C remained relatively understudied, with no clearly defined function in any tissue. Thus, the goal of this thesis was to elucidate the role of NM2C in the intestinal epithelium, and in doing so, gain insight into the function of NM2C as a motor. The studies in this dissertation are the first to determine a role for NM2C in any organ.

Here, we demonstrate that NM2C is localized to the terminal web of enterocytes, answering a decades-old question about M2 in the terminal web [157]. We show that NM2C works to control the length of microvilli via contractility-dependent actin turnover. This gives us valuable insight into factors that control microvillar length and have opened up future studies in gaining a deeper understanding of this contractility-dependent mechanism that results in actin turnover.

Furthermore, we demonstrate that loss of NM2C results in aberrant morphology within the intestinal epithelium. This is in contrast to previous work that has suggested that NM2A can completely compensate for the loss of NM2C [83]. This indicates a

unique role for NM2C in the intestinal epithelium, likely due to how the network of NM2C across enterocytes propagates tension across the epithelial sheet as it undergoes crypt-villus migration. Collectively, the work done in this dissertation provides significant insight into the biological role of NM2C and provides advances in understanding the role of mechanical force in the small intestine.

CHAPTER 2

MATERIALS AND METHODS

Cell Culture and immunofluorescence

Ls174T-W4 (W4) cells (female Hs colon epithelial cells) were cultured in DMEM with high glucose and 2 mM L-glutamine supplemented with 10% tetracycline-free fetal bovine serum (FBS), blasticidin (10 µg/ml), G418 (1 mg/ml), and phleomycin (20 µg/ml); cells were grown at 37°C and 5% CO₂ as our group and others have previously described. This cell line was generous gift from Dr. Hans Clevers (Utrecht University, Netherlands). For SIM or laser scanning confocal imaging, W4 cells were plated onto glass coverslips, and allowed to adhere overnight in the presence of 1 µg/ml doxycycline. For NM2C staining, cells were then washed with warm phosphate-buffered saline (PBS) and fixed with warm 4% paraformaldehyde/PFA for 15 min at 37°C. Cells were subsequently washed three times with PBS, and then permeabilized with 0.1% Triton-X-100 in PBS for 15 minutes at room temperature. Cells were then blocked for 1 hr at room temperature in 5% bovine serum albumin (BSA) in PBS. Finally, cells were incubated with primary antibody (Proteintech anti-NM2C, #20716-1-AP) diluted in 5% BSA/PBS, at 37°C for 1.5 hr, followed by three washes with fresh PBS. Cells were then incubated for 1 hr with goat anti-rabbit Alexa Fluor 488F(ab')₂ Fragment (1:1000, A11070; Invitrogen) and Alexa Fluor 568 Phalloidin (A12380; Invitrogen) at 37° C. Coverslips were washed three times with PBS and mounted on glass slides in ProLong Gold Antifade Mounting Media (P36930; Invitrogen). For cells transfected with Halo-tagged constructs, cells were incubated for 30 min with Janelia Fluor HaloTag ligand (gift from Dr. Luke Lavis, HHMI Janelia Farms) of the appropriate color, diluted to 100 nM after fixation with 4% PFA. Alexa Fluor 488-phalloidin (1:200,

A12379; Invitrogen) was diluted in PBS and incubated for 1 hr at room temperature. Coverslips were washed three times with PBS then mounted on glass slides in ProLong Gold (P36930; Invitrogen).

Cloning and Constructs

pEGFP-NM2C was obtained from Addgene (plasmid #10843). mNEON-green- β -actin was purchased from Allele Biotechnology. pHalo-C1-NM2C (Halo-NM2C) construct was generated via PCR using pEGFP-NM2C as a template. NM2C open reading frame PCR product was TOPO cloned into the pCR8/GW/TOPO vector (K250020; Invitrogen) and then shuttled into the pHalo-C1 backbone, adapted for Gateway cloning using the Gateway conversion kit (11828029; Invitrogen). To generate pHalo-NM2C mutant variants, E479A, R257A, N252A, and R784A were introduced into pHalo-NM2C using QuikChange site-directed mutagenesis kit (200524; Agilent).

Transfections and lentivirus production

All transfections were performed using Lipofectamine2000 (#11668019; Invitrogen) according to manufacturer's instructions and W4 cells were allowed to recover overnight. Following recovery, W4 cells were seeded onto plates or coverslips, and incubated overnight in the absence or presence of 1 μ g/ml doxycycline to induce polarity, and then prepared for immunofluorescence or live cell imaging. Lentivirus was generated by co-transfecting HEK293FT cells (Fetal Hs embryonic epithelial cells; T75 flasks at 80% confluency) with 6 μ g of pLKO.1 shRNA KD plasmids (Millipore Sigma; TRCN0000285308, TRCN0000275175, TRCN0000146426, TRCN0000148318, TRCN0000275115, TRCN0000275174), 4 μ g of psPAX2 packaging plasmid, and 0.8 μ g of pMD2.G envelope plasmid using FuGENE 6 (Promega). For efficient lentiviral production, cells were incubated for 48 hr, then lentivirus-containing media was

collected and concentrated with Lenti-X concentrator (Clontech). To transduce W4 cells with lentivirus, the media was supplemented with 6 ug/ml polybrene (Sigma) and the lentiviral shRNAs. After a 24-hour incubation, the media was changed and resupplemented with 6 ug/ml polybrene and lentiviral shRNAs for an additional 24 hours. The cells were then seeded into plates or flasks and incubated ON in the absence or presence of 1 µg/ml doxycycline, and then prepared for immunofluorescence or SDS-PAGE. For rescue experiments, cells were transiently transfected 48 hours after the second lentiviral infection using Lipofectamine 2000, induced with 1 ug/ml doxycycline ON, and fixed the following morning for immunofluorescence staining with respective antibodies.

Drug Treatments

For fix and stain experiments, W4 cells were split onto glass coverslips, and incubated for 12 hours in the presence of 1 µg/ml doxycycline to induce apicobasal polarity and brush border formation. Induced W4 cells were then incubated with either 20 µM Blebbistatin (B592500; Toronto Research Chemicals), 4 nM Calyculin A (PHZ1044; Invitrogen) or 1 mM 4-hydroxyacetophenone (278564; Sigma-Aldrich) for 10, 30 or 60 minutes. After drug incubation, cells were fixed using methods described below. For live cell imaging experiments, W4 cells were transfected with the appropriate construct and then split onto 35 mm glass bottom dishes (Invitro Scientific, D35- 20–1.5-N). Cells were imaged 24-72 hours after transfection. Once on the microscope, Blebbistatin, Calyculin A or 4-hydroxyacetophenone were added after ~3-5 minutes of baseline imaging; cells were then imaged for an additional 20-60 minutes depending on the drug treatment.

In vivo Blebbistatin treatment, animal surgery and tissue preparation

Animal surgery was conducted humanely according to NIH and AVMA guidelines by a protocol approved by Vanderbilt University IACUC. Mice were anesthetized with vaporized isoflurane (Piramal Healthcare, 66794-017-25) and proximal jejunum was exteriorized. Two 5 mm incisions were made 1 cm apart on the anti-mesenteric side of the jejunum to avoid vasculature on the mesenteric side. The luminal contents were flushed with normal saline and drug was perfused for 4 hours. Verapamil, a broad-spectrum efflux pump inhibitor (Sigma Aldrich, V1711202) was used at a 10 mM; Blebbistatin (B592500; Toronto Research Chemicals) was used at 80 μ M. Animals were sacrificed by isoflurane overdose followed by cervical dislocation. Segments of jejunum were excised and cut along the length to exteriorize the lumen. Guts were fixed in 2% formaldehyde in 100 mM phosphate-buffered saline (PBS; pH 7.1) supplemented with 2 mM Ca^{2+} / Mg^{2+} for 12 hours at 4C.

Whole mount tissue preparation and immunofluorescence

Segments of WT and KO intestine were removed, flushed with phosphate-buffered saline (PBS), and prefixed for 10 min with 2% paraformaldehyde (PFA) to preserve the tissue structure. The tube was then cut along its length, subdissected into 0.5 μ m² square chunks, fixed for an additional 30 min in 2% PFA at room temperature (RT), and washed three times in PBS-T with 0.2% Triton X-100 for ten minutes each. Tissue chunks were then blocked with 5% normal Goat serum (NGS) overnight (ON) at 4°C with constant agitation using a Labquake® shaker/rotisserie. Primary antibodies (listed below) were diluted in 1% NGS/PBS-T and incubated at 4°C ON with constant agitation using a Labquake® shaker/rotisserie, followed by three washes with PBS-T. Tissue chunks were then stained with phalloidin and secondary antibodies (listed below) in 1%

NGS/PBS-T for 4h at RT or ON at 4°C, washed three times with PBS, and mounted with Prolong Gold Antifade mounting medium (P36930; Invitrogen) on 35mm glass bottom dishes, with villi oriented towards the glass for imaging on an inverted microscopy setup.

Organoid culture and immunofluorescence

Intestinal organoids were generated from littermate MYH14^{-/-}-eGFP-LifeAct and MYH14^{+/+}-eGFP-LifeAct mice generated from MYH14^{-/-}-eGFP-LifeAct breeding pairs. Crypts were isolated from the duodenum of 6–8-week-old animals using 2.5mM EDTA in DPBS. Crypts were initially cultured in advanced DMEM/F12 supplemented with 500 ng/ml EGF (Invitrogen), 150 ng/ml Wnt/Noggin/R-spondin 1 combination solution and 1mM Y27632, suspended in 50 µL Matrigel (BD Biosciences). 24-48hrs after isolation, media was switched to advanced DMEM/F12 (Invitrogen) supplemented with the following growth factors: 500 ng/ml EGF (Invitrogen), 100 ng/ml Noggin (R&D Systems), 500 ng/ml R-spondin 1 (R&D Systems), and 1mM N-Acetylcysteine (Sigma). Organoids were grown at 37°C and 5% CO₂. Prior to live imaging or fixation, organoids were transferred to glass bottom dishes (Celvis D35-20-1.5-N) and cultured in advanced DMEM/F12 (Invitrogen) supplemented with the following growth factors: 500 ng/ml EGF (Invitrogen), 50 ng/ml Noggin (R&D Systems), 500 ng/ml R-spondin 1 (R&D Systems), and 1mM N-Acetylcysteine (Sigma) for a minimum of 12hrs. For immunofluorescence imaging, organoids were fixed for 30 min in 2% PFA at room temperature (RT), and washed three times in PBS-T. Organoids were permeabilized with 0.2% Triton X-100 in PBS-T for 40min at RT, and then blocked with 5% normal Goat serum (NGS) (Abcam ab7481) overnight (ON) at 4°C. Primary antibodies (listed below) were diluted in 1% NGS/PBS-T and incubated at 4°C ON, followed by three washes with PBS-T.

Organoids were then stained with phalloidin and secondary antibodies (listed below) in 1% NGS/PBS-T for 4h at RT or ON at 4°C, washed three times with PBS and imaged in PBS.

Formalin-fixed paraffin embedded swiss roll preparation and immunohistochemistry

Segments of WT and KO intestine were removed, flushed with phosphate-buffered saline (PBS), and prefixed for 10 min with 4% paraformaldehyde (PFA) to preserve the tissue structure. The tube was then cut along its length, rolled from proximal to distal, secured with a 26g syringe needle and fixed for 48hrs in a large volume of neutral buffered formalin (NBF) at room temperature (RT). Following initial fixation, the syringe needle was carefully removed, and the tissue roll placed in a large cassette for paraffin embedded. Dehydration, paraffin-embedding, and sectioning at 10- μ m was performed by the Translational Pathology Shared Resource (TPSR) at Vanderbilt University Medical Center. Paraffin-embedded small intestinal swiss rolls of WT and PACSIN2 KO were deparaffinized using Histo-clear solution (Fisher) and rehydrated in a descending graded-ethanol series. Slides were then subject to an antigen retrieval step consisting of boiling for 1 h in a solution of 10 mM Tris (pH 9.0) and 0.5 mM ethylene glycol-bis(β -aminoethyl ether)-N,N,N',N'-tetraacetic acid (EGTA). Slides were then washed three times in PBS and stained blocked at 4°C with primary antibodies (see below) in 5% NGS/PBS. Slides were then stained ON at 4°C with primary antibodies (see below) in 1% NGS/PBS. After being washed three times with PBS, samples were stained with secondary antibodies in 1% NGS/PBS for 4 h at RT. Slides were then washed three

times with PBS and mounted in ProLong Gold Antifade mounting media. Hematoxylin and eosin (H&E) stain was performed by the TPSR.

Light microscopy

Super-resolution imaging was performed using a Nikon N-SIM Structured Illumination Microscope equipped with an Andor DU-897 EM-CCD, four excitation lasers (405, 488, 561, and 647 nm), and a 100x/1.49 NA TIRF objective. SIM images were reconstructed using Nikon Elements. For live-cell spinning disk confocal microscopy, W4 cells were transfected with the appropriate marker construct in a six well plate. Cells were then split onto 35 mm glass bottom dishes (Invitro Scientific, D35- 20–1.5-N) and incubated in the presence or absence of 1 µg/ml doxycycline for a minimum of 12 hrs and up to 36 hrs. Cells transfected with Halo-tagged constructs were incubated with appropriately colored Janelia Fluor HaloTag ligand diluted to 100 nM in the standard cell culture media described above. Cells were incubated for 30 min with HaloTag ligand-media, media was then removed, and cells were washed with 37° C PBS. PBS was replaced with standard cell culture media and cells were allowed to equilibrate to new media for 15 min at 37° C. Live-cell imaging was performed on a Nikon Ti2 inverted light microscope equipped with a Yokogawa CSU-X1 spinning disk head, Andor DU-897 EMCCD camera or a Photometrics Prime 95B sCMOS camera, 488 nm and 561 nm excitation lasers, a 405 nm photo-stimulation laser directed by a Bruker mini-scanner to enable targeted photoactivation, photoconversion, and photobleaching), and a 100x/1.49 NA TIRF objective. Images were acquired every 15-60 sec for 20-60 min. For photokinetic studies of actin dynamics, baseline images were obtained for several frames prior to bleaching, then for an additional 3-10 min of recovery at 10 sec intervals. Bleaching was performed on a line ROI (0.1 µm in width and 3-15 µm in length) using a

405 nm laser at 30% power with a 10 μ s dwell time. During imaging, cells were maintained with humidity at 37° C with 5% CO₂ using a stage-top incubation system. Image acquisition was controlled with Nikon Elements software. 3D time series images were oversampled in the z-dimension with z-steps ranging from 0.09 μ m to 0.18 μ m to allow for deconvolution (Nikon Elements Automatic or Richardson-Lucy algorithms).

Fixed cell or tissue confocal microscopy was performed using a Nikon A1 laser-scanning confocal microscope equipped with 405, 488, 561 and 645nm LASERs or a Nikon Ti2 Eclipse equipped with 488, 561 and 635nm, excitation LASERs, a Hamamatsu X1 spinning disk and Hamamatsu Orca-Fusion BT sCMOS camera. Objectives used on both microscopes were 10x/0.45 NA, 20x/0.75 NA, 25x/1.05 NA SIL, 40x/1.25 NA SIL, 60x/1.40 NA oil, 100x/1.25 NA SIL, and 100x/1.49 TIRF oil. All images used for quantitative comparisons were prepared with equal treatment, acquired with identical parameters (e.g. pinhole diameter, detector gain, laser power), and processed in an identical manner. High resolution 10x magnification slide scanning for PPFE immunohistochemistry slides was performed by the Digital Histology Shared Resource (DHSR) at Vanderbilt University Medical Center (VUMC).

Electron microscopy

Segments of WT and KO intestine were placed in 0.1M HEPES (pH 7.3) and subdissected into 2-mm chunks at RT. Samples were placed in scintillation vials, incubated in RT fix buffer (4% PFA, 2.5% glutaraldehyde, 2 mM CaCl₂ in 0.1M HEPES) for 1 h, and washed three times in HEPES buffer. Samples were incubated with 1% tannic acid/HEPES for 1 h and washed three times with ddH₂O, followed by incubation

with 1% osmium tetroxide/ddH₂O for 1 h. Samples were then washed three times with ddH₂O, incubated in 1% uranyl acetate/ddH₂O for 30 min, and then washed with ddH₂O. For SEM, samples were dehydrated in a graded ethanol series and then dried using critical point drying. Samples were then mounted on aluminum stubs and coated with gold/palladium using a sputter coater. Imaging was performed using a Quanta 250 Environmental SEM operated in high-vacuum mode with an accelerating voltage of 5 kV. All EM reagents were purchased from Electron Microscopy Sciences. For TEM, segments were dehydrated in a graded ethanol series, gradually infiltrated with Spurr's standard, and cured at 60°C for 8–12 h until blocks were firm, but not brittle. Thin sections were cut and poststained with uranyl acetate and Sato's lead citrate. Images were collected with a Philips FEI T-12 transmission electron microscope operating at 100 kV.

Image analysis and statistical testing

All images were processed and analyzed using Nikon Elements software, FIJI software package (<https://fiji.sc>), or IMARIS software.

To quantify murine tuft cells, the number of villus structures was counted per field of view (FOV) manually. Tuft cells per FOV were counted using 3D segmentation in IMARIS. Quantification of tuft cells in organoids was done manually.

Crypt depth was computed by drawing a 1px line from the bottom on the crypt, to the hinge region, and measuring the length of line using FIJI. Villus area was computed by manually drawing an region of interest (ROI) around the edge of a villus, and measuring with FIJI. Villi per mm was calculated by manually counting the number of villi in a small intestine swiss roll and measuring the length of the serosa.

For lateral area and cell aspect ratio measurements, villi were manually divided into thirds. Lateral area and aspect ratio were measured automatically by FIJI, using manually drawn ROIs of cells that were judged to be in the plane of the section.

Measurements of cell roughness, circularity, elongation, apical area, and perimeter were performed automatically using Nikon Elements software. ZO-1 signal was used to manually define the threshold of cell boundaries. Thresholded signal was used to create a binary. Binary objects that did not represent a whole cell due to tissue curvature were manually deleted prior to using the Nikon Elements automated measurement feature.

Organoids were thresholded using the 3D thresholding feature in Nikon Elements.

Volume and surface area of whole organoids were computed automatically using the 3D measurements feature in Nikon Elements.

Cell area, equivalent diameter, cell perimeter and roughness of cells in organoids were computed automatically using Nikon Elements software. ZO-1 signal was used to manually define the threshold of cell boundaries. Thresholded signal was used to create a binary. Binary objects that did not represent a whole cell due to organoid curvature were manually deleted prior to using the Nikon Elements automated measurement feature.

Radiality maps from en face SIM images showing terminal web NM2C-EGFP puncta were generated using NanoF-Super-Resolution Radial Fluctuations (SRRF) in FIJI (**Gustafsson et al., 2016**) with a ring radius of 2, radiality magnification of 1, and six ring axes. To perform line-scan analysis, a line was drawn along the axis of microvilli that were in plane with a distinct tip and base visible. The intensity of the

NM2C signal was recorded and normalized with the lowest intensity set to 0 and the maximum set to 1. The microvillar length axis from individual scans was also normalized with the base set to 0 and the tip set to 1. Normalized line scans were then plotted together and fitted to a single Gaussian using nonlinear regression analysis (Prism v.7; GraphPad). For quantification of the percentage of cells with brush border, cells were scored as “brush border positive” if they displayed polarized F-actin accumulation as visualized using a 40x objective on a Nikon A1R laser-scanning confocal microscope as we have previously described. Microvillar length measurements were performed on projected SIM images by tracing individual microvillar actin bundles using FIJI. For analyses in which individual microvilli were measured, at least 10 microvillar actin bundles were scored per cell and at least 10 cells measured per experiment

Statistical significance was calculated using unpaired T-test for pairwise comparisons, or one-way ANOVA for multiple comparisons. Percent brush border and microvillar length data were analyzed with a D’Agostino and Pearson omnibus normality test to determine normal distribution. Statistical analyses performed are stated in the figure legends. All graphs were generated and all statistical analysis were computed in PRISM v.9.2 (Graphpad).

CHAPTER 3

NONMUSCLE MYOSIN-2 CONTRACTILITY-DEPENDENT ACTIN TURNOVER LIMITS THE LENGTH OF EPITHELIAL MICROVILLI

Originally published as:

Chinowsky, C.R., Pinette, J.A, Meenderink, L.M., Lau, K.S., Tyska, M.J. (2020)
Nonmuscle myosin-2 contractility-dependent actin turnover limits the length of
epithelial microvilli. *Molecular Biology of the Cell* 31:2, 2803-2815

SUMMARY

Brush border microvilli enable functions that are critical for epithelial homeostasis, including solute uptake and host defense. However, mechanisms that regulate the assembly and morphology of these protrusions are poorly understood. The parallel actin bundles that support microvilli have their pointed-end rootlets anchored in a filamentous meshwork referred to as the “terminal web”. Although classic EM studies revealed complex ultrastructure, the composition and function of the terminal web remains unclear. Here we identify non-muscle myosin-2C (NM2C) as a component of the terminal web. NM2C is found in a dense, isotropic layer of puncta across the sub-apical domain, which transects the rootlets of microvillar actin bundles. Puncta are separated by ~210 nm, the expected size of filaments formed by NM2C. In intestinal organoid cultures, the terminal web NM2C network is highly dynamic and exhibits continuous remodeling. Using pharmacological and genetic perturbations in cultured intestinal epithelial cells, we found that NM2C controls the length of growing microvilli by regulating actin turnover in a manner that requires a fully active motor domain. Our

findings answer a decades old question on the function of terminal web myosin and hold broad implications for understanding apical morphogenesis in diverse epithelial systems.

INTRODUCTION

Hollow organs such as the intestinal track, kidney tubules, and brain ventricles, are lined with solute transporting epithelial cells. In the small intestine, individual epithelial cells, known as enterocytes, present thousands of microvilli on their apical surface. These protrusions are tightly packed into a highly ordered array collectively known as the brush border [2]. Microvilli serve two general functions - they markedly increase the membrane surface area for nutrient absorption, and also provide the first line of defense against harmful compounds and microbes found in the luminal compartment [122]. Due to the constant regeneration of the mammalian gut epithelium, continuous differentiation of enterocytes and assembly of the brush border are critical for maintaining homeostasis throughout an organism's lifetime. Despite microvilli occupying a critical physiological interface, mechanisms that regulate apical morphogenesis remain unclear.

A single microvillus is supported by a core of 20-30 actin filaments, bundled together in parallel by actin bundlers villin, espin, and fimbrin [26, [27, [28, [158], with the barbed-ends oriented at the distal tips, and the pointed-ends anchored in a dense, filamentous network known as the terminal web [34, [41, [42]. While the terminal web was first described several decades ago in ultrastructural studies, little is known about how it contributes to the apical domain structure, microvillar organization, or brush border function. Interestingly, knockout (KO) mouse models lacking major brush border

structural components, such as PACSIN-2, plastin-1, or actin bundling proteins (villin, espin and plastin-1) exhibit significant perturbations to the terminal web [154, [155, [156]. All of these models exhibit a common phenotype, where the terminal web thins and microvilli become disorganized or shortened, which further suggests that terminal web architecture and brush border morphology are intimately linked.

Previous biochemical and ultrastructural studies of the terminal web identified several components of this filamentous network, including intermediate filaments and spectrins [46, [47, [159, [160]. Early deep-etch electron microscopy (EM) studies also identified “8 nm filaments”, which appeared to crosslink microvillar actin bundle rootlets [40]. However, these structures did not label with myosin sub-fragment 1 (S1) suggesting they were not composed of actin. Additional immunogold labeling EM data led to speculation that 8 nm filaments contained myosin [3, [34]. This was further supported by immunofluorescence labeling studies that made use of a pan-myosin antibody raised against myosin-2 epitopes [43]. However, the identity of the myosin, and the organization and function of 8 nm filaments in brush border structure and function remained unclear for decades.

All class 2 myosins are constitutive dimers of heavy chains, each comprised of an N-terminal motor domain, followed by a tandem pair of IQ motifs that are constitutively bound by regulatory and essential light chains (RLC and ELC, respectively), a long coiled-coil, and a non-helical tail piece at the C-terminus [161]. A fully functional myosin-2 molecule consists of two heavy chains (HC), each bound by one RLC and one ELC. Class 2 myosins are regulated by reversible phosphorylation at sites on the RLC, the C-terminal tailpiece, or both, which controls activation and

assembly of contractile units, respectively [72, [73, [162]. Driven by electrostatic interactions between their coiled-coil tails, skeletal, cardiac and non-muscle myosin-2 (NM2) variants self-assemble into bipolar filaments that serve as fundamental force-generating units [71, [163].

Non-muscle class 2 myosins (NM2A encoded by MYH9, NM2B encoded by MYH10, and NM2C encoded by MYH14) are ubiquitously expressed and have been implicated in diverse contractile activities including cytokinesis, cell motility, and the control of cell morphology [73]. At higher levels of biological complexity, these motors have been implicated in shaping and bending of tissues, collective cell migration, and regulating the paracellular permeability of epithelial sheets [65, [73]. NM2 paralogs have distinct kinetic properties, which allow these motors to perform specific and distinct functions within the cell [1, [161]. In the context of in vitro sliding filament assays, tail-less NM2C heavy meromyosin (HMM) fragments move actin filaments at $\sim 0.05 \mu\text{m/s}$, slower than both NM2B ($\sim 0.08 \mu\text{m/s}$) and NM2A ($\sim 0.29 \mu\text{m/s}$) [164]. Bipolar filaments assembled by NM2C ($\sim 293 \text{ nm}$) tend to be shorter than those assembled by NM2B ($\sim 323 \text{ nm}$) or NM2A ($\sim 301 \text{ nm}$). Filaments composed of NM2C also contain fewer molecules than those assembled by NM2A and NM2B, resulting in thinner filaments ($\sim 8 \text{ nm}$ vs. $\sim 11 \text{ nm}$ wide) and presumably a lower potential for generating force [1].

A previous proteomic study by our laboratory revealed that brush border fractions isolated from mouse small intestine contain all three NM2 paralogues, with NM2C exhibiting high-level abundance [165]. Although NM2C remains the most poorly understood paralogue with regard to biophysical properties and physiological function, previous work established that this isoform exhibits specific expression in pituitary

gland, glial cells, as well as inner ear sensory, intestinal, and kidney epithelia [166]. Mutations in MYH14 have been linked to hearing loss, peripheral neuropathies, and developmental defects in the lower gastrointestinal tract [88, [89, [90, [91, [167, [168, [169, [170, [171]. The parallel perturbation of both inner ear and intestinal epithelial systems by mutations in MYH14 is intriguing, as actin bundled–supported stereocilia found on the apical surface of hair cells are closely related to microvilli found on solute-transporting epithelia and may share mechanisms of assembly and maintenance [55, [172]. Previous studies of a NM2C-EGFP–expressing mouse revealed that this motor is highly enriched at the junctional margins of sensory and intestinal epithelial cells, where cell–cell contacts are formed [83]. At these sites, NM2C assembles into circumferential sarcomere-like structures, characterized by a linear array of puncta that are uniformly separated by ~300–400 nm, a distance comparable to the expected length of contractile filaments formed by NM2 isoforms [1, [83]. Treatment of NM2C-EGFP mouse epithelial tissues with myosin-2 inhibitor blebbistatin (which prevents force generation) increased the interpuncta distance, indicating that under normal conditions the circumferential NM2C band is under tension [83]. Careful inspection of images in this previous study also revealed that the NM2C signal is not confined to the circumferential/junctional array, as dimmer puncta also appear to span the cell medially, throughout the entire subapical region.

In this paper, we report that NM2C localizes at the pointed ends of microvillar actin bundles, where it forms a highly dynamic array of puncta that are confined to the plane of the subapical terminal web. Although these puncta demonstrate approximately twofold lower levels of NM2C enrichment relative to those found in a circumferential

array, based on their similar spacing and dynamics, we propose that they represent NM2C contractile filaments. Using pharmacological and genetic perturbations in cultured intestinal epithelial cells, we found that the activity of this motor controls the length of growing microvilli by regulating actin disassembly at the pointed ends. These findings address a decades-old question on the function of the terminal web myosin-2 and hold important implications for understanding brush border assembly and apical morphogenesis in epithelial systems.

RESULTS

NM2C is enriched in the enterocyte brush border terminal web in vivo

Although all three NM2 isoforms are detectable in the brush border proteome [165], our analysis of recently generated single-cell RNAseq (scRNAseq) data from the intestinal tract [173, [174]revealed that NM2C is preferentially expressed in mature villus enterocytes relative to NM2A or NM2B, the latter of which was barely detectable (Figure 3-1). We therefore focused subsequent studies on characterizing the function of NM2C.

To investigate the subcellular distribution

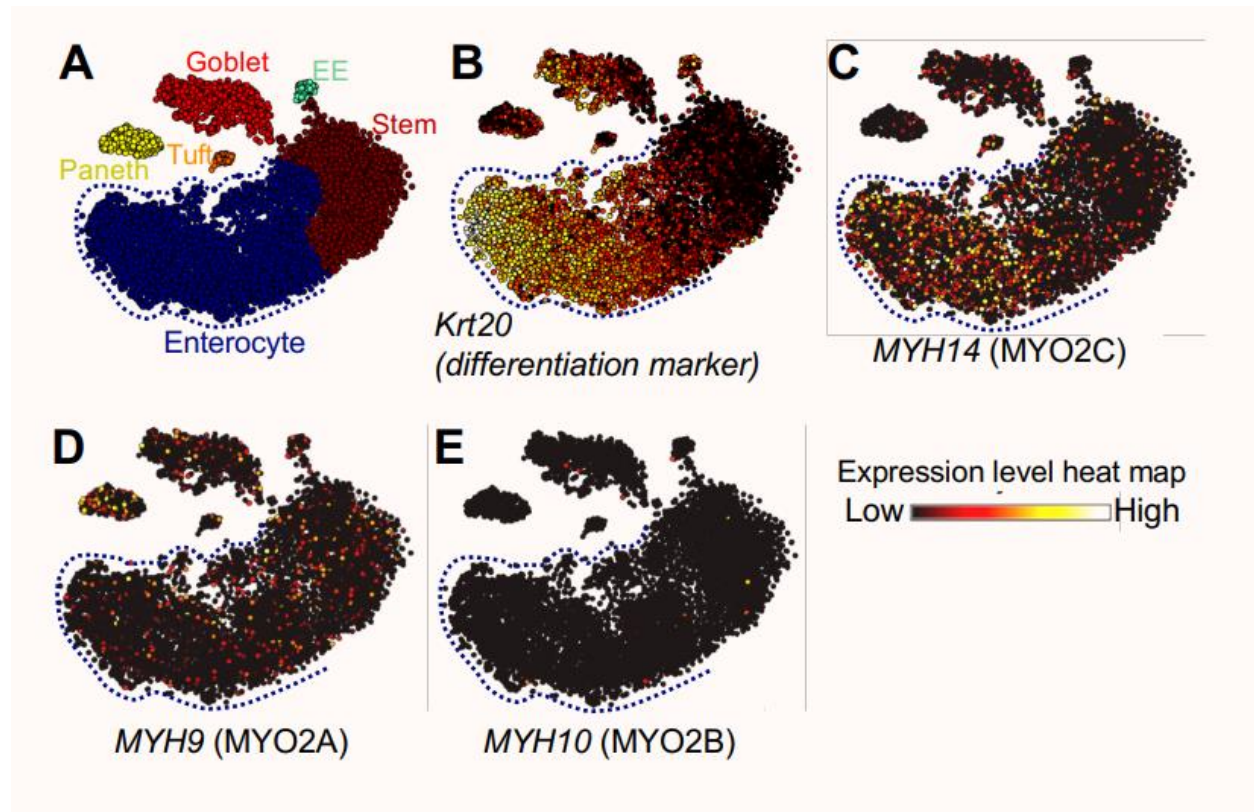


Figure 3-1: : Cell type-specific expression of myosin genes in the mouse ileal epithelium assessed by scRNA-seq. **A**, Annotated intestinal epithelial cell populations defined by canonical markers for each cell type. Enterocyte lineage denoted by blue dotted line. Overlay of gene expression of **B**, *Krt20* to delineate differentiation status and **C-E**, various NM2 isoforms. Overlays are normalized gene expression on a log-like (ArcSinh) scale.

of this motor in intestinal tissues in more detail, we took advantage of mice that express an enhanced green fluorescent protein (EGFP)-tagged form of NM2C from the endogenous locus [83]. In this model, EGFP is fused in frame to the C-terminus of the NM2C heavy chain. Consistent with scRNAseq analysis, confocal imaging of frozen intestinal tissue sections revealed the strong apical signal of NM2C along the full length of villi (Figure 3-2A). Lower levels of NM2C were also observed on the apical surface of immature epithelial cells in the stem cell-containing crypt compartments (Figure 3-2A, merge). To gain additional resolution at the subcellular scale, tissue sections from NM2C-

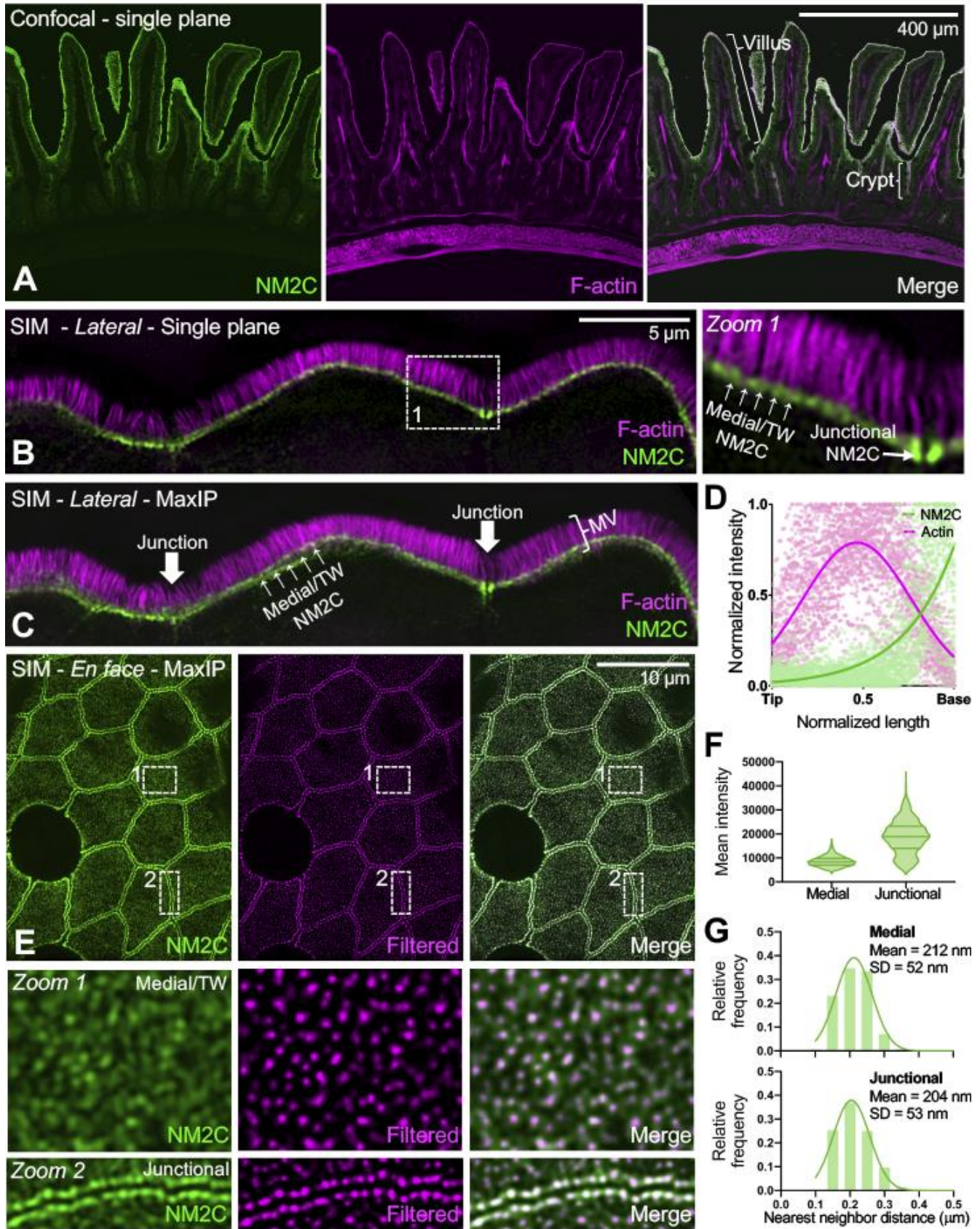


Figure 3-2: NM2C localizes to the enterocyte terminal web. **A**, Single plane confocal microscopy of small intestinal tissue from a mouse endogenously expressing EGFP-NM2C (green), co-stained with phalloidin-568 to visualize F-actin (magenta). Representative villus and crypt regions are highlighted by brackets in merge panel. **B**, Single plane structured illumination microscopy (SIM) image of small intestinal tissue from a mouse endogenously expressing EGFP-NM2C (green), co-stained with phalloidin-568 to visualize F-actin (magenta). Zoom 1 shows region bound by the dashed white box; medial and junctional population are highlighted. **C**, Maximum intensity projection (MaxIP) of lateral view shown in B. **D**, Normalized intensity plots of NM2C and F-actin signals taken from line-scans drawn parallel to the microvillar axis ($n = 45$) reveals enrichment of NM2C at the base of microvilli in the terminal web. **E**, *En face* SIM MaxIP images of small intestinal tissue from a mouse endogenously expressing EGFP-NM2C (green); medial/terminal web and junctional populations are highlighted in zooms 1 and 2, respectively. SIM image (left) is shown in parallel with a version that was filtered using NanoF-SRRF (middle), which accentuated intensity peaks from individual NM2C puncta and allowed for more precise localization of their position. Merge image (right) shows composite of the original SIM image with the SRRF-filtered image. **F**, Mean intensity of medial/terminal web vs. junctional NM2C puncta from SIM images. **G**, Histograms of nearest neighbor distances generated by localizing medial (top) vs. junctional (bottom) NM2C puncta in SRRF-filtered SIM images. For F and G, $n = 2,480$ medial puncta and $n = 1,019$ junctional puncta. Scale is indicated on individual image panels.

EGFP mice were subject to super-resolution structured illumination microscopy (SIM).

SIM images of enterocytes were acquired with the apical-basolateral axis either parallel or perpendicular to the focal plane (lateral or *en face*, respectively). Lateral views revealed that the apical NM2C-EGFP signal observed in lower-magnification images was confined to a band of signal that overlapped specifically with the rootlets of microvilli, near the pointed ends of core actin bundles (Figure 3-2B and C). This band of signal spanned the entire apical surface at the level of the terminal web, and its intensity increased significantly where it connected to the circumferential/junctional array at the margins of the cell (Figure 3-2C, white arrows). This was further confirmed with quantitative line scan analysis of NM2C-EGFP fluorescence intensities along individual microvilli visualized in SIM images (Figure 3-2D). *En face* images of NM2C-EGFP tissue samples revealed that the terminal web NM2C signal was strikingly punctate; the

differential enrichment of NM2C in medial versus junctional puncta was also apparent in these images (Figure 3-2E). Intensity analysis revealed that medial puncta in the terminal web were approximately half the intensity of junctional puncta (Figure 3-2F). Moreover, nearest neighbor distance calculations showed that medial and junctional puncta are minimally separated by approximately the same distance, ~210 nm (Figure 3-2G). Thus, in addition to its localization in the circumferential band at the margins of enterocytes, NM2C is also enriched throughout the terminal web, where it is well-positioned to interact directly with the rootlets of microvillar core actin bundles.

Terminal web and junctional NM2C puncta exhibit continuous remodeling

To enable live imaging studies of NM2C dynamics in the terminal web, we isolated crypts from NM2C-EGFP mice, which were then expanded into 2-dimensional (2D) organoid monolayers by plating on a thin layer of Matrigel. Confocal imaging of 2D organoids revealed a pattern of apical NM2C-EGFP distribution similar to that observed in fixed native tissue sections, with prominent junctional bands and a layer of medial puncta at the level of the terminal web (Figure 3-3A.) Time-lapse imaging showed that both networks are highly dynamic and continuously remodeling, with puncta across the surface translocating, fusing and splitting on a timescale of minutes (Figure 3-3A zooms 1 and 2). We also performed photokinetic studies to examine the turnover rates of NM2C-EGFP puncta in the medial vs. junctional populations (Figure 3-3B-E). Fluorescence recovery after photobleaching (FRAP) analysis revealed that, despite the two-fold difference in puncta intensity (Figure 3-2F), the recovery rates for these two populations were remarkably similar (Figure 3-3D). Thus, medial NM2C-EGFP puncta exhibit spacing and

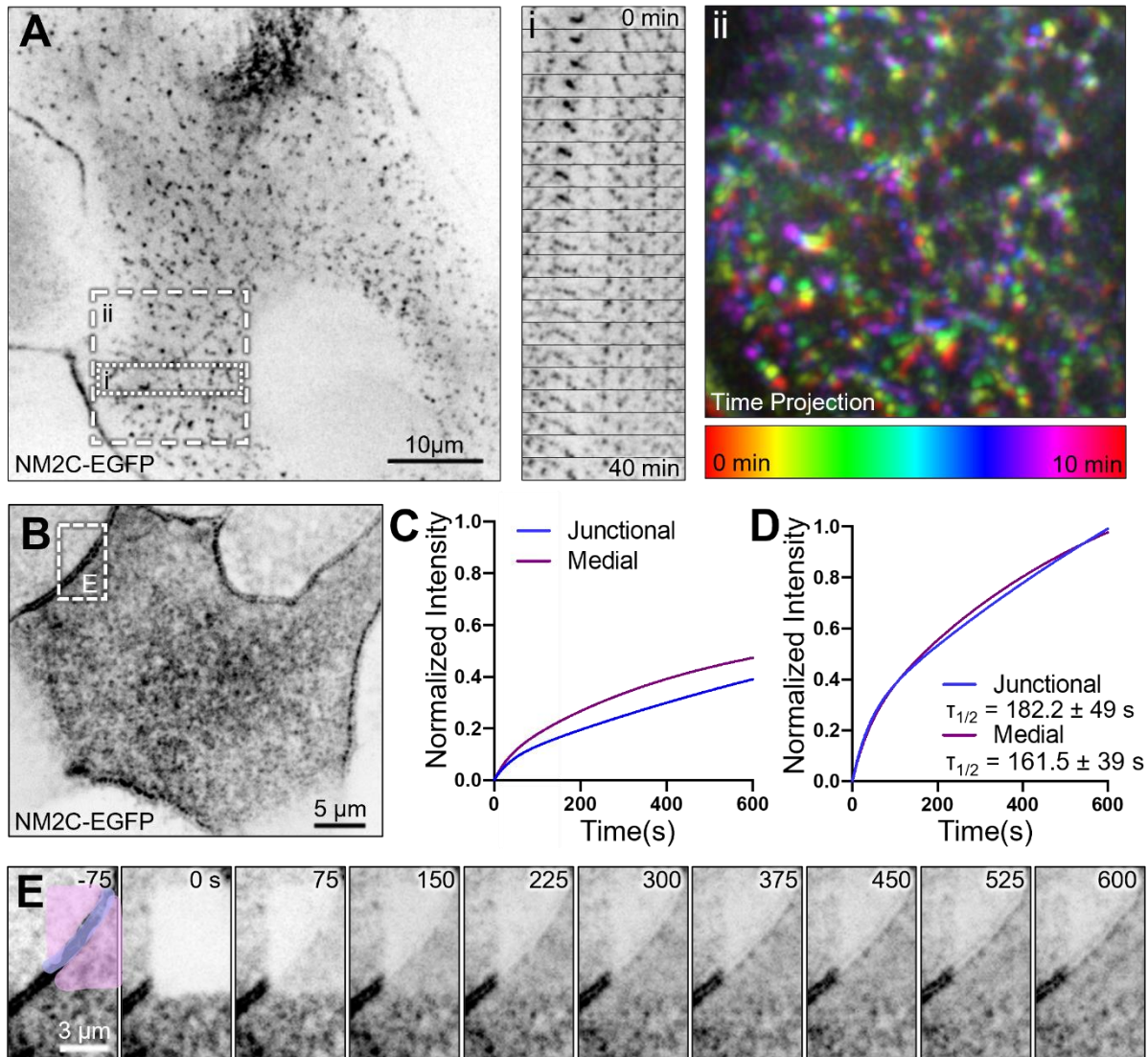


Figure 3-3: Medial and junctional populations NM2C puncta exhibit similar dynamics. **A**, Live spinning disk confocal imaging of an organoid monolayer (i.e. 2D) derived from EGFP-NM2C expressing mouse small intestinal tissues; signal is inverted to facilitate visualization of dim structures. Zoom 1 shows a montage sampled at 2-minute intervals that reveals extensive remodeling of medial NM2C puncta over 40 minutes; puncta marked with yellow asterisk at $t = 0$ min exhibits striking expansion stretching/expansion during the time-lapse. Zoom 2 shows a color-coded time projection that reveals large-scale motion of medial NM2C network over 10 minutes. **B**, FRAP analysis was performed on EGFP-NM2C puncta in 2D organoid monolayers to determine turnover rates in the junctional vs. medial populations. **C**, FRAP recovery curves for junctional and medial NM2C populations normalized to pre-bleach intensity, show that both populations exhibit large immobile fractions ($\sim 50\%$). **D**, Kinetic analysis of datasets normalized to peak post-bleach intensities indicates that junctional and medial NM2C signal recovers at comparable rates; $\tau_{1/2}$ for both populations are shown on the plot. **E**, Image montage of FRAP time-lapse data shown in B; junctional population is highlighted in purple, whereas medial NM2C is shown in pink.

turnover kinetics that are similar to junctional puncta. Given that the circumferential junctional belt of NM2 is an established contractile array [83], these data suggest that terminal web NM2C might also hold the potential to exert mechanical force.

Activation of NM2 leads to shortening of microvilli

To further investigate the function of NM2C in the terminal web, we sought an

appropriate cell

culture model that

recapitulates the

terminal localization

observed in native

tissue. Based on

previous studies

from our laboratory

and others [175,

[176], Ls174T-W4

(W4) cells mimic

partially

differentiated

intestinal epithelial

cell and thus,

provide a model for

studying actively

growing microvilli [36, [155]. This cell line is derived from human colonic epithelium and

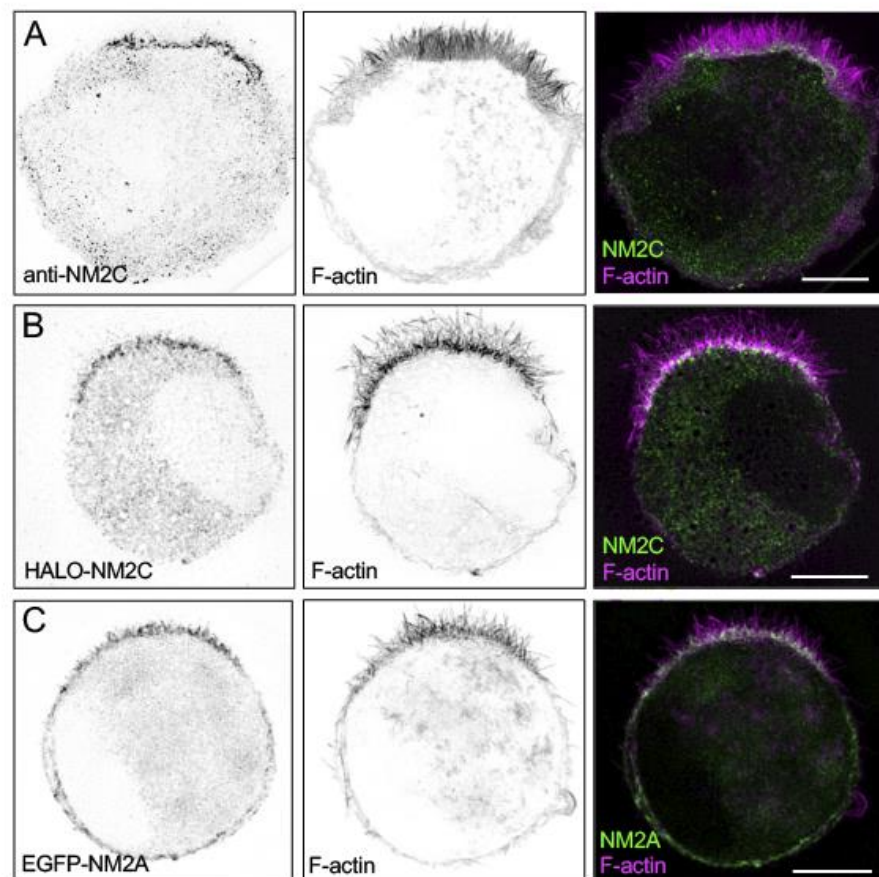
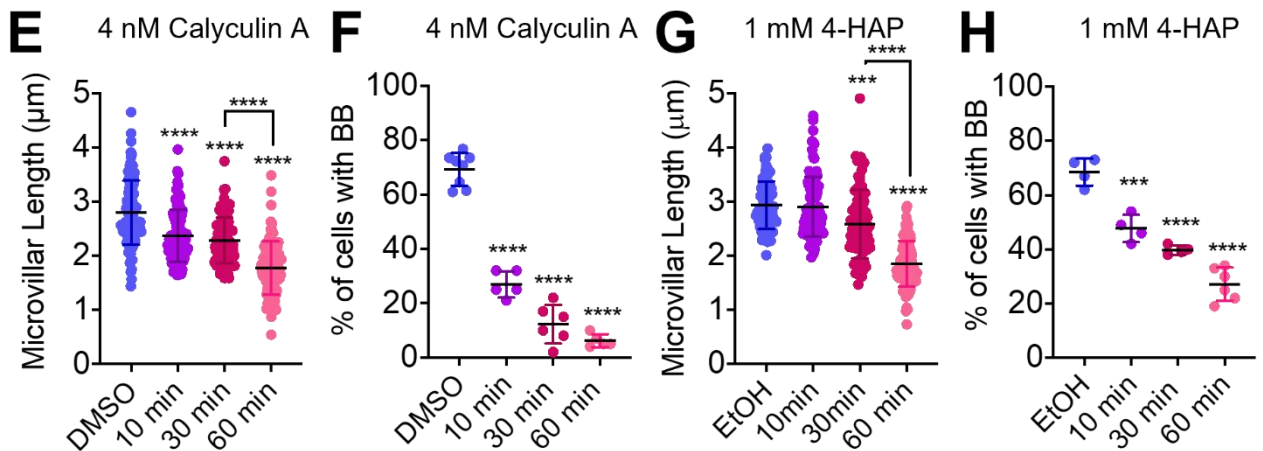
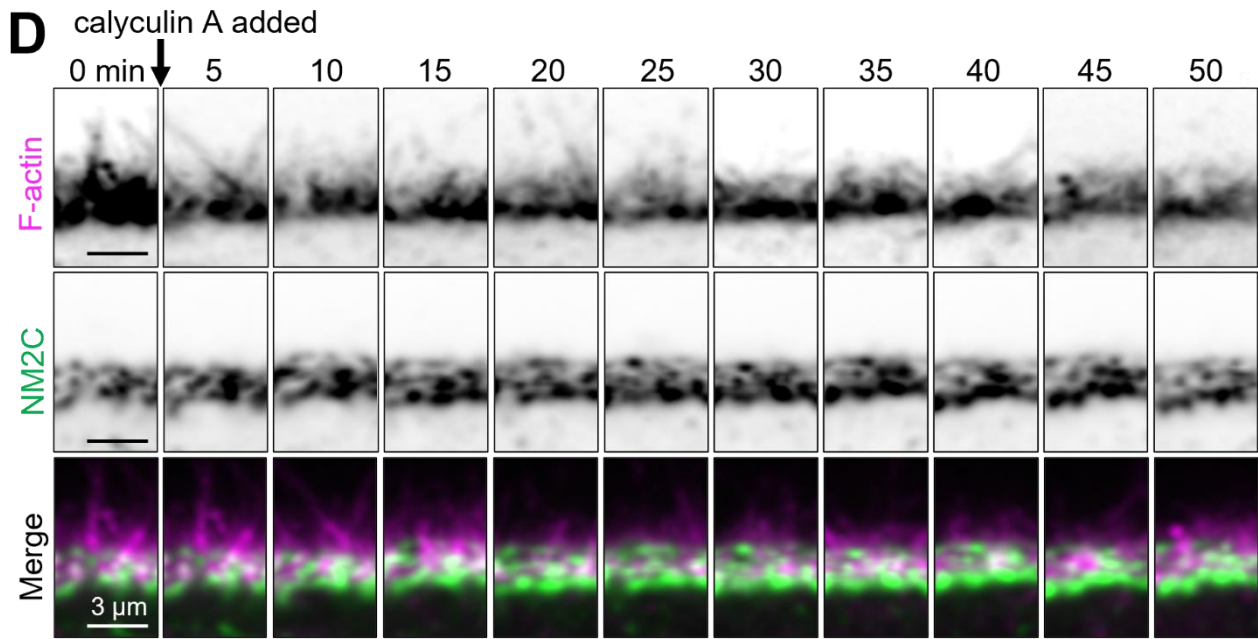
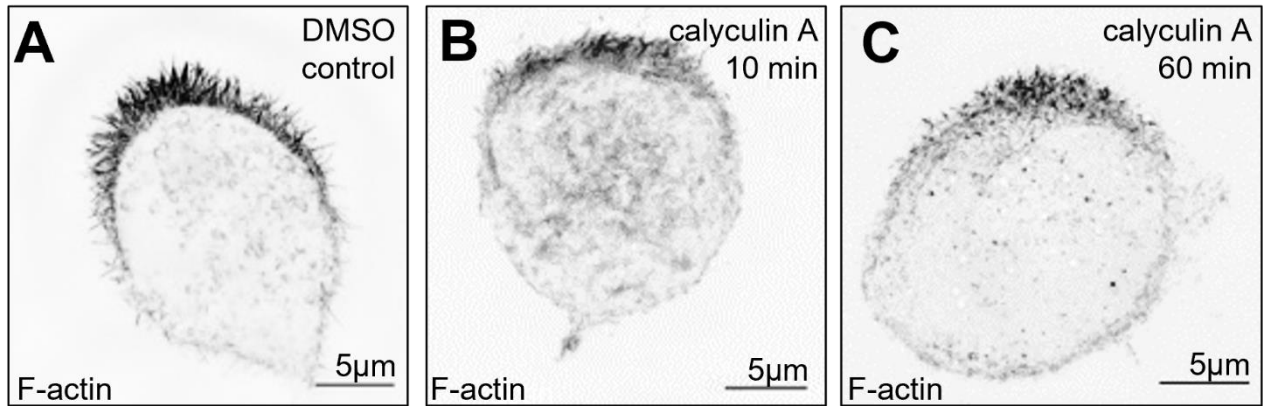


Figure 3-4: NM2C localizes specifically to the terminal web of W4 cells. SIM MaxIP of representative phalloidin-stained (F-actin, magenta) Ls175T-W4 cells displaying: **A**, endogenous NM2C staining, **B**, overexpression of Halo-NM2C labeled with JF585, or **C**, overexpression of EGFP-NM2A. Scale bars are 5 μm .

can be induced via doxycycline treatment to acquire apical-basolateral polarity and assemble a brush border [175, [177]. In this model, microvilli extend from the cell surface parallel to the focal plane, which facilitates length measurements and assessment of protein localization along the protrusion axis. Of critical importance, W4 cells do not grow in monolayers and polarize as single cells. This unique advantage allowed us to specifically interrogate the function of the terminal web population of NM2C in the absence of the circumferential actin-myosin belt that normally assembles when cell-cell junctions are formed. SIM imaging of anti-NM2C stained W4 cells revealed striking localization at the base of microvilli, in a band that resembled the terminal web observed in native tissue samples (Figure 3-4A). Importantly, an NM2C construct with a C-terminal HaloTag also demonstrated similar terminal web enrichment in W4 cells (Figure 3-4B). Thus, both native and over-expressed NM2C localization in W4 cells are comparable to that observed in native intestinal tissue.

To probe NM2 function in the W4 cell terminal web, we first treated polarized W4 cells with calyculin A, a threonine/serine phosphatase inhibitor that is commonly used to elevate levels of phosphorylated myosin RLC and thus, increase active motor units [72,

[178, [179, [180]. While calyculin A does not specifically target NM2C activity, antibody staining experiments in W4 cells (Figure 3-4) indicate that this isoform specifically enriches in the terminal web relative to the other major isoform, NM2A; this is also



consistent with previous proteomic analysis [165] and scRNAseq data presented in this paper (Figure 3-1), which allude to NM2C as the dominant terminal web isoform. Strikingly, treatment with 4 nM calyculin A resulted in marked shortening of microvilli

Figure 3-5: Activation of NM2 shortens epithelial microvilli. SIM MaxIP images of representative phalloidin-stained (F-actin) Ls174T-W4 cells fixed after **A**, 60 min exposure to DMSO vehicle control, **B**, 10 min exposure to 4 nM calyculin A, or **C**, 60 min exposure to 4 nM calyculin A; signals are inverted to facilitate visualization of dim structures. **D**, Image montage from spinning disk confocal time-lapse data shows the impact of calyculin A treatment on apical microvilli in a Ls174T-W4 cell expressing F-actin probe EGFP-UtrCH (magenta) with Halo-NM2C (green) labeled with JF585. **E**, Quantification of microvillar length in Ls174T-W4 cells fixed after 10 min, 30 min, and 60 min in 4 nM calyculin A; each data point is a single microvillus, at least 10 microvilli per cell, minimum of 10 cells per condition. **F**, Quantification of the percentage of brush border positive cells as a function of time in calyculin A. Each data point is percentage of cells with a brush border in a stitched 5x5 40x image. **G**, Quantification of microvillar length in Ls174T-W4 cells fixed after 10 min, 30 min, and 60 min in 1 mM 4-HAP; each data point is a single microvillus, minimum of 10 cells per condition, at least 10 microvilli per cell. **H**, Quantification of the percentage of brush border positive cells as a function of time in 4-HAP. Each data point is percentage of cells with a brush border in a stitched 5x5 40x image. E, F, G, and H were tested using ordinary one-way ANOVA with Dunnett's multiple comparisons; ***, $p < 0.0002$; ****, $p < 0.000$ vs. DMSO/EtOH negative controls unless otherwise noted.

over the course of 60 min ($2.8 \pm 0.6 \mu\text{m}$ control vs. $1.8 \pm 0.5 \mu\text{m}$ calyculin A, Figure 3-3A-E, Movie 2). In calyculin A-treated W4 cells expressing Halo-NM2C, microvillar shortening was temporally paralleled by increased enrichment of NM2C in the terminal web (Figure 3-3D, Movie 2). In some cases, W4 cells appeared to lose nearly all surface microvilli following calyculin A treatment (Figure 3-4C). Indeed, the fraction of W4 cells that exhibited F-actin enriched brush borders also decreased significantly over the 60 min course of these experiments (Figure 3-4F). These drug treatment studies suggest that increased NM2 activity is linked to microvillar shortening over time, and at longer time points, complete loss of the apical brush border. To further confirm that microvillar shortening was due to NM2 activation, we performed similar experiments using 4-hydroxyacetophenone (4-HAP), a small molecule that preferentially increases the activity of NM2B and NM2C, but not NM2A (52). In previous studies, 4-HAP was shown to increase NM2 motor activity and also enhance cortical enrichment of this

motor [181, [182]. Similar to calyculin A-treated cells, W4 cells treated with 4-HAP exhibited increased terminal web enrichment of NM2C, and significant time-dependent shortening of microvilli and reduction in the percentage of cells presenting a brush border (Figure 3-5G-H, Figure 3-6). Together these drug treatment studies indicate that increased NM2 activity and enrichment in the terminal web is linked to microvillar shortening over time, and at longer time points, complete loss of the apical brush border.

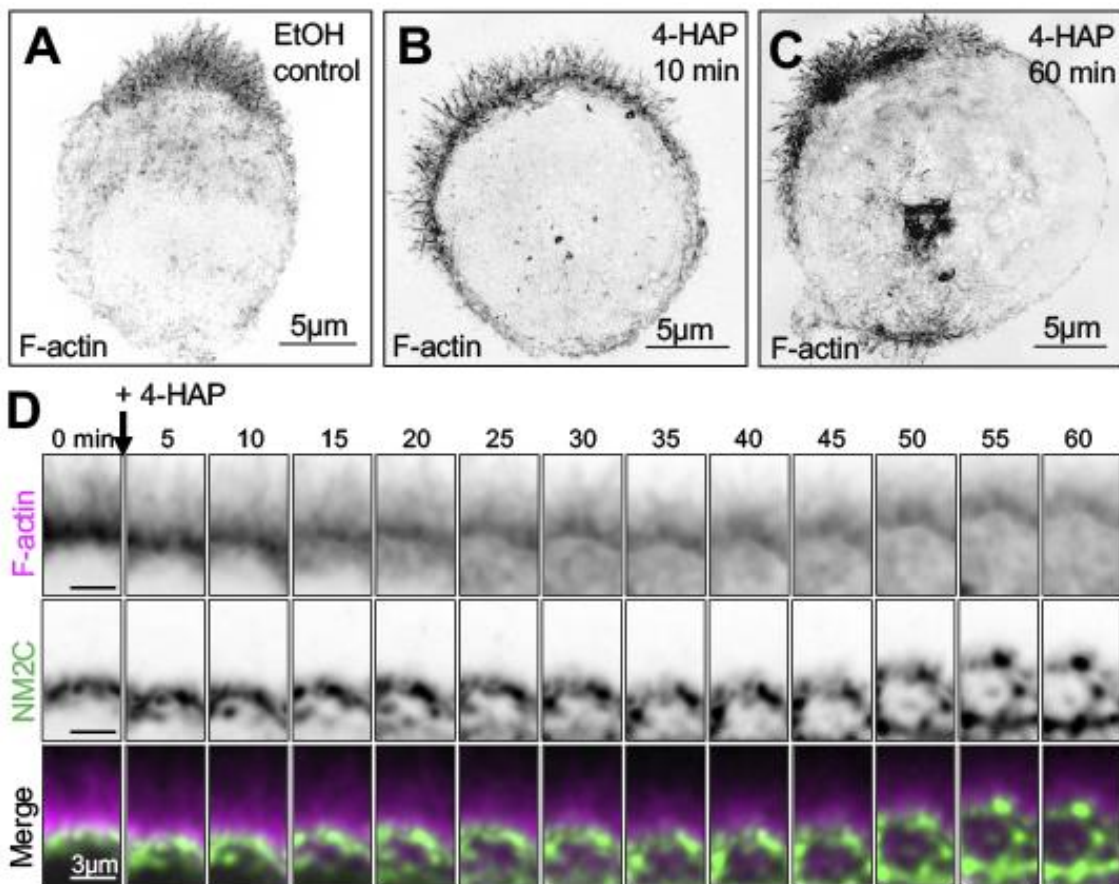


Figure 3-6: Activation of NM2C with 4-HAP shortens epithelial microvilli. SIM MaxIP images of representative phalloidin-stained (F-actin) Ls174T-W4 cells fixed after: **A** 60 min exposure to EtOH vehicle control, **B**, 10 min exposure to 1 mM 4-HAP, or **C**, 60 min exposure to 1 mM 4-HAP; signals are inverted to facilitate visualization of dim structures. **D**, Image montage from spinning disk confocal time-lapse data shows the impact of 4-HAP treatment on apical microvilli in a Ls174T-W4 cell expressing F-actin probe EGFP-UtrCH (magenta) with Halo-NM2C (green) labeled with JF585.

Inhibition of NM2 leads to microvillar elongation

To investigate the impact of NM2 loss-of-function on the brush border actin cytoskeleton, we treated W4 cells with the well characterized NM2 inhibitor, blebbistatin, which binds to and locks the NM2 motor domain in a non-force producing state [183, [184]. After treating polarized W4 cells with 20 μ M blebbistatin, we noted that microvilli became significantly less dynamic and subsequently exhibited a marked elongation, in some cases doubling their length ($2.8 \pm 0.6 \mu\text{m}$ control vs. $5.2 \pm 1.3 \mu\text{m}$ blebbistatin treated) over the 60 min experimental time course (Figure 3-7A-E). In contrast the accumulation of NM2C observed in response to treatment with NM2 activators, inhibition with blebbistatin promoted a relatively static population of NM2C in the terminal web (Figure 3-7F). Moreover, although W4 cell microvilli normally extend from a single clearly defined apical 'cap', we noted that blebbistatin induced the dispersion of protrusions across the cell surface (Figure 3-7C). Thus, inhibition of NM2 leads to unregulated microvillar growth and disorganization of the brush border on the epithelial cell surface.

Blebbistatin reverses the impact of calyculin A on microvillar length

Blebbistatin is a well-established and specific inhibitor of NM2, whereas calyculin A has broader effects on a group of threonine/serine phosphatases [178, [179, [183, [184]. To determine if the microvillar shortening effects we observed with calyculin A could be countered with blebbistatin treatment, polarized W4 cells were subject to serial drug treatments. Cells were first treated with 4 nM calyculin A for 50 min until microvillar length was significantly diminished. At the 50 min mark, calyculin A was chased with 20 μ M blebbistatin. These

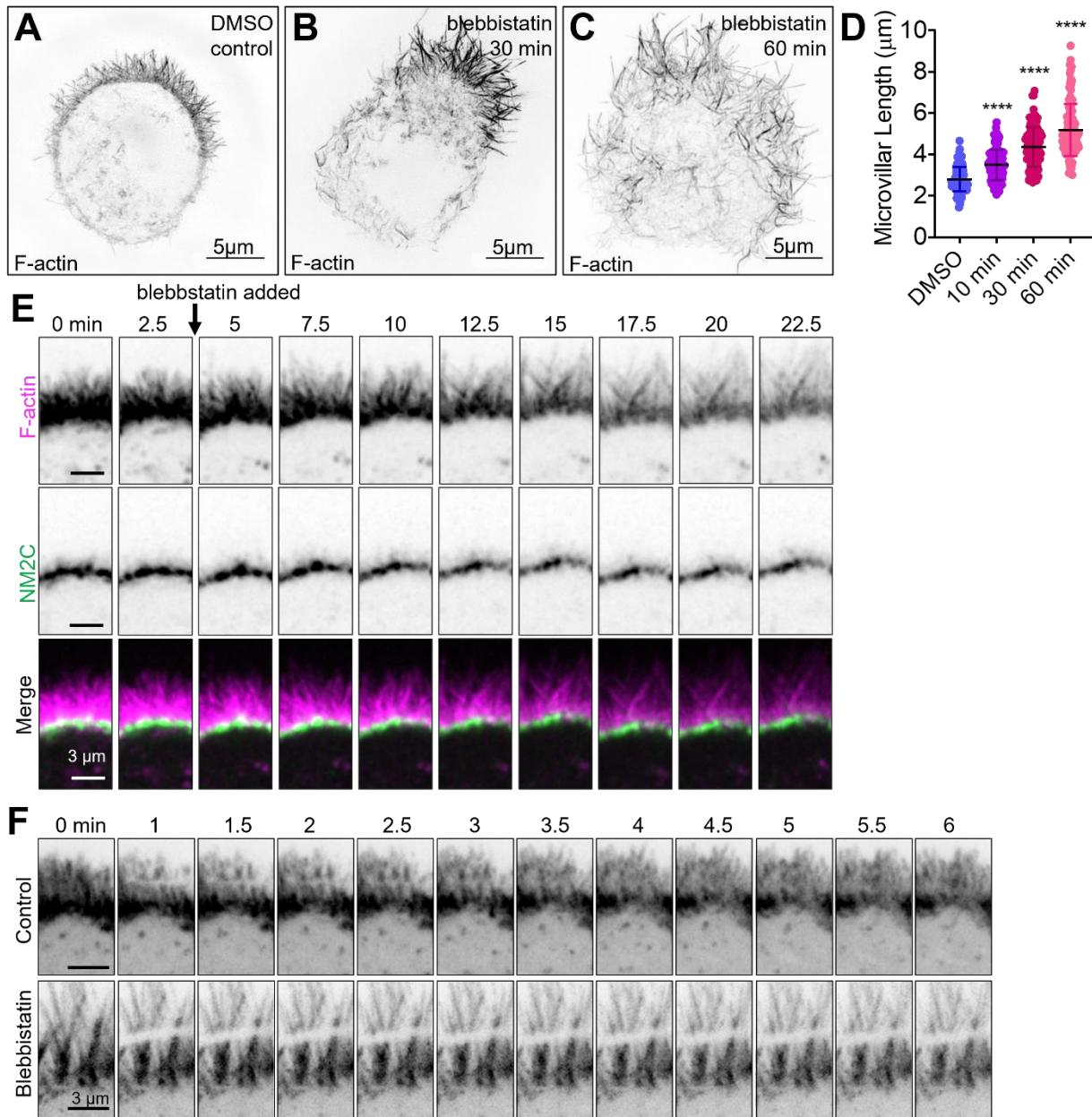


Figure 3-7: Inhibition of NM2 elongates microvilli and limits actin turnover. SIM MaxIP images of representative phalloidin-stained (F-actin) Ls174T-W4 cells fixed after **A**, 60 min exposure to 20 mM DMSO vehicle control, **B**, 10 min exposure to 20 mM blebbistatin, or **C**, 60 min exposure to 20 mM blebbistatin; signals are inverted to facilitate visualization of dim structures. **D**, Quantification of microvillar length from Ls174T-W4 cells fixed after 10 min, 30 min, and 60 min in 20 µM blebbistatin; each data point is a single microvillus, minimum of 10 cells per condition, at least 10 microvilli per cell. Ordinary one-way ANOVA with Dunnett's multiple comparisons test; ****, $p < 0.0001$ vs. DMSO control. **E**, Image montage of the brush border of a Ls174T-W4 cell expressing EGFP-UtrCH (magenta) and Halo-NM2C labeled with JF585 (green), imaged for 22.5 min after the addition of blebbistatin using spinning disk confocal microscopy; 2.5 min interval between frames. **F**, Image montage of FRAP analysis of Ls174T-W4 cells expressing mNeon-Green β -actin in the absence (top row) or presence of 20 µM blebbistatin (bottom row) for 15 minutes prior to imaging.

time-lapse data revealed that specific inhibition of NM2 with blebbistatin was sufficient to drive rapid elongation of the shortened microvilli that result from calyculin A treatment. Based on these data we conclude that the impact of calyculin A on microvillar length is most likely mediated by an increase in terminal web NM2 activity. In combination with the calyculin A and 4-HAP experiments described above, these data strongly suggest that under normal conditions, terminal web localized NM2C plays a role in limiting the length of microvilli and promoting their confinement in the apical domain.

NM2 promotes actin turnover in brush border microvilli

How does terminal web NM2C limit the length of microvilli under normal conditions?

Time-lapse analysis of W4 cells treated with 20 μ M blebbistatin revealed that microvilli, which normally exhibit striking dynamics on the apical surface (e.g. elongation, shortening, and waving or pivoting around the base) immediately become static and subsequently begin to elongate. A previous study from our group established that the parallel actin bundles that support microvilli exhibit robust treadmilling (i.e. retrograde flow), where actin monomer incorporation at tip oriented barbed-ends is balanced by subunit removal from the pointed-ends that emerge from the base of these structures [52]. Early in differentiation this treadmilling activity is coupled to directed motion of microvilli across the apical surface, which in turn promotes the adherent packing and organization of these protrusions [52]. In treadmilling actin structures, steady-state length can be increased by raising the incorporation rate at the barbed-ends, lowering the disassembly rate at the pointed-ends, or some combination of the two [185, [186, [187]. To examine the possibility that NM2C mechanical activity promotes the

treadmilling of microvillar cores by driving the disassembly of actin bundles in the terminal web (where the pointed-ends reside), we performed FRAP on W4 cells transfected with mNeonGreen-b-actin, in the absence and presence of 20 μ M blebbistatin. In control W4 cells, a rectangular ROI was bleached across the brush border and recovered rapidly, within < 4 minutes, presumably due to treadmilling of individual actin cores (Figure 3-7F). However, in W4 cells treated with 20 μ M blebbistatin, bleached ROIs remained almost completely static and showed little to no recovery, even after up to 10 minutes (Figure 3-7F). Based on these findings, we conclude that under normal conditions, NM2C promotes the disassembly of the pointed-ends of core actin bundles within the terminal web. Without this activity (e.g. in response to blebbistatin treatment), treadmilling stalls and core bundles elongate as a result.

Knockdown of NM2C results in aberrant actin structures and limited viability

In order to further assess the role of NM2C in microvilli, we chose to perform a knockdown (KD) using short hairpin RNA (shRNA). Using western blotting, we determined that sh#26 (Figure 3-8A) provided the highest KD efficiency and proceed with preliminary studies using this KD line. All results presented in the following Figure 3 are preliminary and should not be interpreted as statistically significant, as they lack the numbers for such conclusions. Interestingly, a variety of phenotypes were observed in these KD cells: many cells formed ruffles, and appeared to lose their “epitheliality”, never forming any actin structure that resembled a BB (Figure 3-8B). However, other cells did form a BB, but with very short, nubby microvilli. Finally, some KD cells had a mass of actin signal on the Z-projecting face of cell, which is abnormal for the W4 cell line. Given the variety of cellular phenotypes, it was not possible to qualify values such

as BB length. We did attempt to

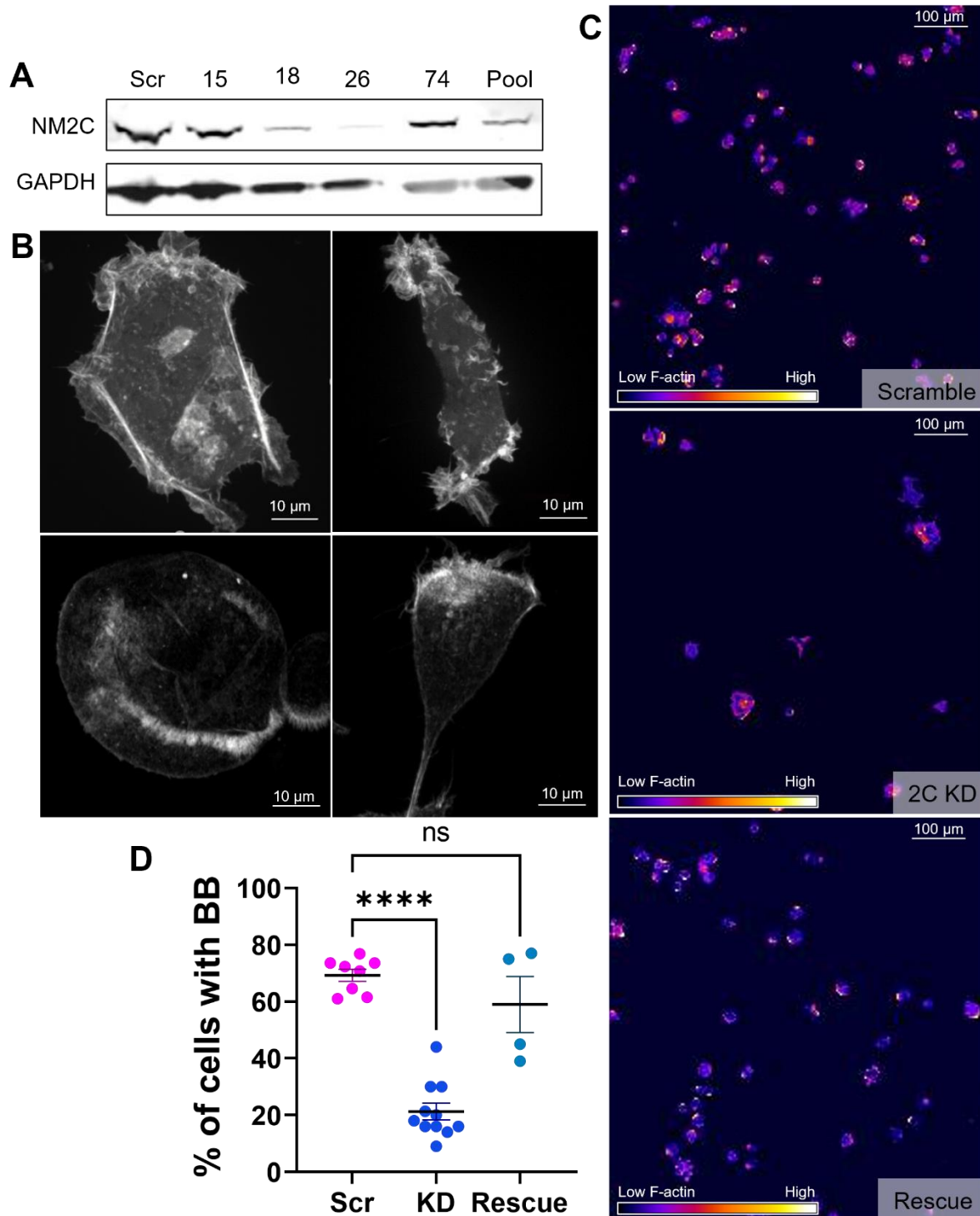


Figure 3-8: NM2C KD results in aberrant actin structures. **A**, Representation western blot showing GAPDH (loading control) and NM2C with varying shRNA constructs. **B**, Representative confocal MaxIP images of various 2C KD cell phenotypes **C**, Large image stitches representative of scramble, KD, and WT rescue cells. **D**, Quantification of percentage of cells presenting with a BB. Each data point is a 3x3 large image stitch. Testing was performed using an ordinary one-way ANOVA with Dunnett's multiple comparisons test; ****, $p < 0.0001$ vs. Scramble.

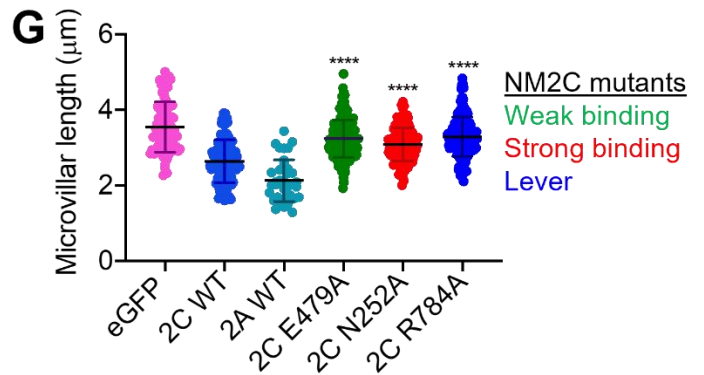
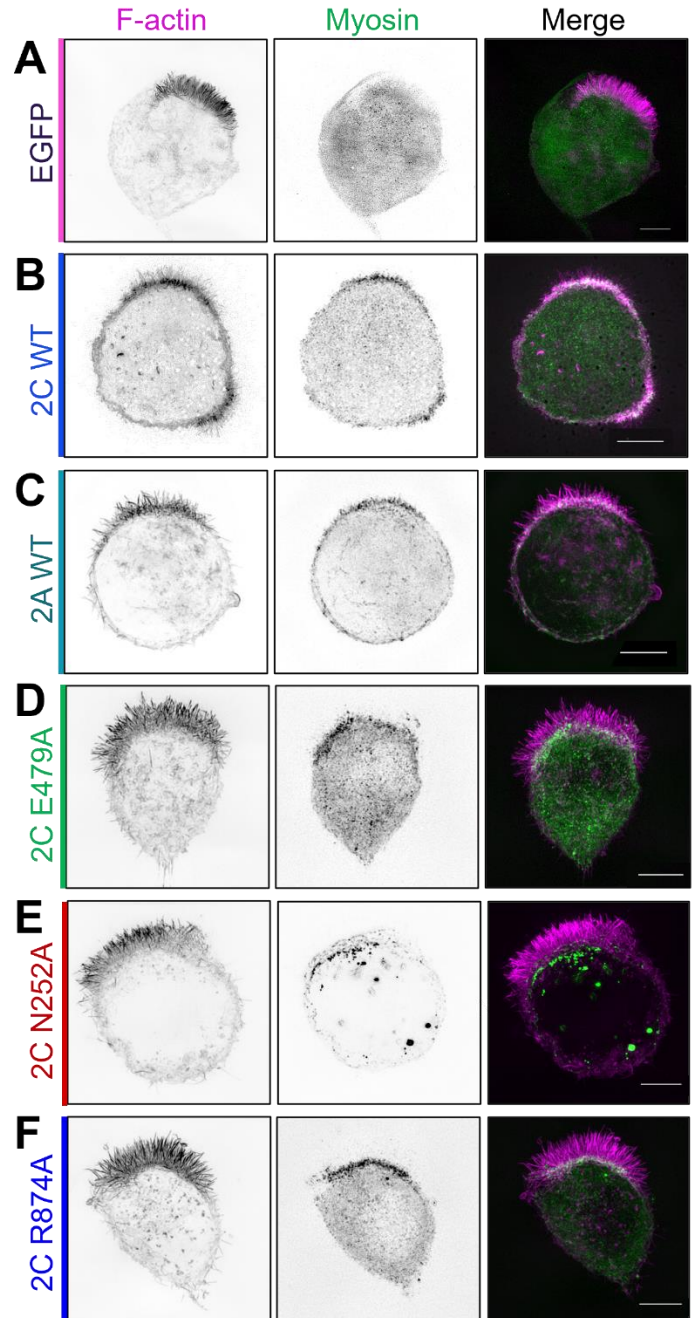
qualify the amount of cells presenting a brush border, using large 3 x 3 stitched images taken with a 20x objective (Figure 3-7C). However, here we found that both KD and rescue cells had substantially lower numbers than the scramble control (140 KD cells vs 152 rescue cells vs 671 control cells, data in Figure 3-7D), despite imaging the same number of fields, and attempting to plate the cells at similar densities. We did find that KD cells formed significantly less BB than scramble control cells, and that rescuing with WT NM2C was sufficient for obtaining control levels of BB development (Figure 3-7D). However, due to the difficulty with cell viability, and the confounding 2C KD cell phenotypes, we did not pursue using KD-rescue studies for structure-function of the NM2C motor. Instead, we chose to use overexpression, which produced robust and reproducible phenotypes.

NM2C motor domain activity is required for limiting microvillar length

All myosin motor domains contain highly conserved residues that participate directly in actin and ATP binding, as well as ATP hydrolysis and force production [65, [161]. Previous studies established that mutations to these residues disrupt myosin activity in predictable ways [188, [189, [190, [191]. To determine which facets of motor activity are

needed for limiting microvillar length in W4 cells, we generated variants of NM2C with mutations predicted to lock the motor domain in weak or strong binding states (E497A or N252A, respectively; [188, [192]. We also targeted R784, which was identified as a critical residue in the NM2C crystal structure [193]. R784 rests at the interface of the

converter, N-terminal subdomain, and lever arm in the NM2C motor domain, and mutation of this residue leads to failure of converter rotation and impaired nucleotide binding, hydrolysis, and release [193]. This general structure/function approach has been employed by our laboratory and others in the past to examine the requirement for myosin motor activity in different biological contexts [38,



[194, [195]. Typically, we would employ a KD/rescue strategy to first eliminate endogenous NM2C expression and then re-express NM2C mutant variants to assess their function. However, NM2C KD was not well tolerated by W4 cells (Figure 3-8) as stable NM2C KD cells lines using lentiviral transduction of shRNAs were often multinucleated and lacked a clearly defined apical brush border, which obscured analysis of microvillar morphology. As an alternate approach for assaying the impact of NM2C motor domain perturbations, we turned to an over-expression approach. Indeed, Halo-NM2C over-expression significantly shortened W4 cell microvilli (3.6 μm control vs 2.6 μm Halo-NM2C; Figure 3-9A,B,G). As a point of comparison, we also overexpressed EGFP-NM2A, which exerted an even more potent length reduction effect (3.6 μm control vs 2.3 μm in NM2A; Figure 3-9C,G). Strikingly, all three NM2C variants

Figure 3-9: A functional NM2C motor domain is required for microvillar length regulation. SIM MaxIP images of representative Ls174T-W4 cell overexpressing **A**, EGFP as a negative control, **B**, WT Halo-NM2C, **C**, WT EGFP-NM2A, **D**, Halo-NM2C-E479A, **E**, Halo-NM2C-N252A, or **F**, Halo-NM2C-R874A. All Halo-NM2 constructs are labeled with JF585 (green) and cells are also co-stained with phalloidin to visualize F-actin (magenta). **G**, Microvillar length quantification for each over-expression condition; measurements were made from 10 cells per construct, 8-10 microvilli measured per cell. Each data point is a single microvillus. Testing was performed using an ordinary one-way ANOVA with Dunnett's multiple comparisons test; ****, $p < 0.0001$ vs. WT NM2C.

with function-disrupting mutations in the motor domain were unable to significantly reduce microvillar length when over-expressed in W4 cells (Figure 3-9D-G). From these data, we conclude that normal motor domain catalytic and mechanical activities are needed for NM2C to exert a length limiting effect on microvilli.

DISCUSSION

NM2C activity limits the length of dynamic epithelial microvilli

In this work, we establish that the poorly studied NM2C isoform, which is highly expressed in transporting and sensory epithelia, not only localizes to the well-characterized junctional network, but is also enriched in a second network that spans the full diameter of the cell at the level of the sub-apical terminal web. Our super-resolution imaging studies show that terminal web NM2C is ideally positioned to interact directly with the rootlets of parallel actin bundles that support apical microvilli. Using a combination of chemical and genetic perturbations to increase or decrease the activity of this motor, we observed striking elongation or shortening of microvilli, respectively (Figure 3-10). We found the treadmilling dynamics, which are characteristic of nascent growing microvilli [52], are almost completely abolished upon treatment with the NM2 inhibitor, blebbistatin. In that context, inhibition of NM2 did not impair forward movement of microvilli, which was found to be driven by actin incorporation into core bundle filaments, although it did lead to the elongation of motile protrusions from their trailing ends [52]. Thus, in two entirely different cellular contexts, blebbistatin exerts similar elongating effects on microvillar morphology. We note here that the time courses of the blebbistatin effects in these two cell culture models are quite different, and the slower onset in the W4 system is most likely explained by higher expression levels of efflux pumps in intestinal epithelial cells (e.g., MDR1; [74]; [196]). Nevertheless, together these findings lead us to conclude that NM2C activity limits the length of microvilli, most likely by promoting disassembly of core bundle actin filaments near or at their pointed ends, which are embedded in the subapical terminal web. Because microvillar length

control mechanisms are still poorly defined, these findings represent an important first step toward understanding how the dimensions of these structures are controlled.

Organization of NM2C in the terminal web

The presence of a filament forming myosin in the terminal web was first suggested

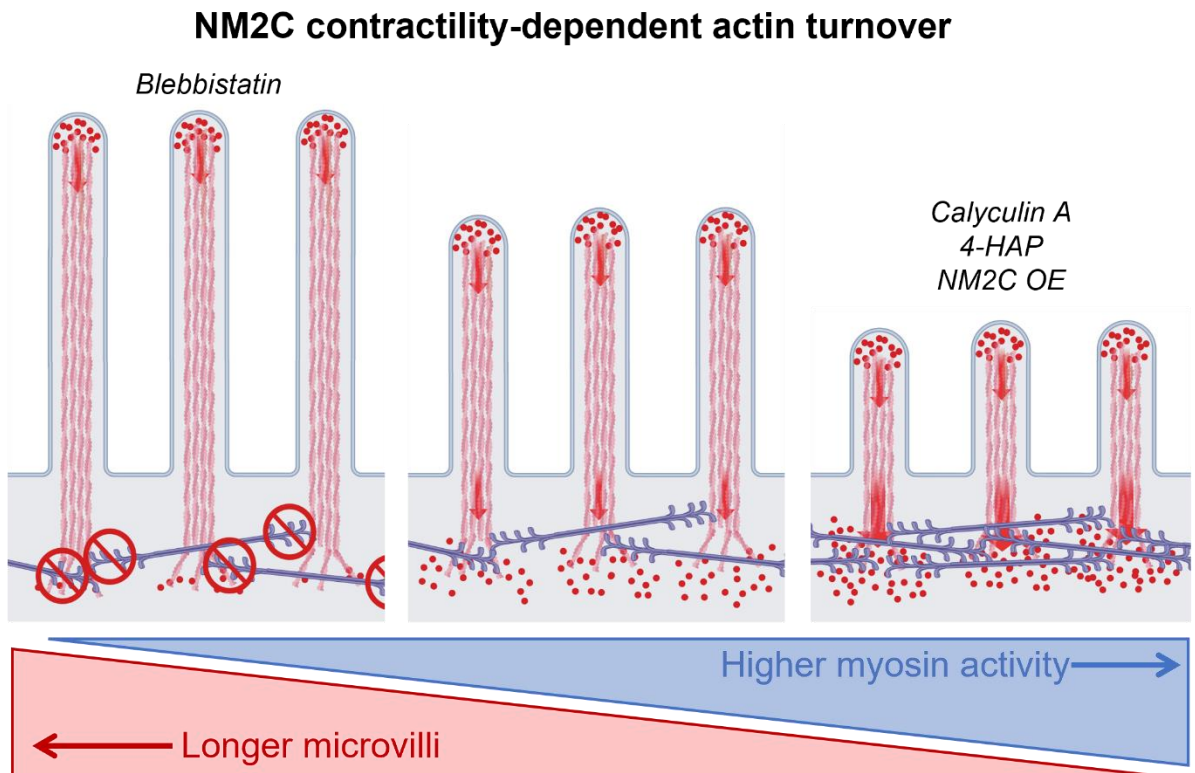


Figure 3-10: Model of contractility-dependent actin turnover in brush border microvilli. Cartoon summarizing the phenotyping observations linking NM2 inhibition, activation, and overexpression to perturbations to microvillus length. NM2C might also play a role in physically sequestering microvilli on the apical surface, a function that is not captured in this graphic summary

decades ago in high-resolution transmission electron microscopy (TEM) images of microvillar rootlets [34]. These iconic images revealed that the space between core bundle rootlets is spanned by small filaments with dimensions comparable to those of thick filaments found in muscle. On the basis of these early observations, Mooseker and Tilney (1975) postulated that adjacent microvilli were physically linked by a filament-

forming myosin, in a manner analogous to the organization of muscle sarcomeres. Indeed, the ability of NM2 to generate force at functionally significant levels is linked to its capacity to form bipolar filaments reminiscent of the thick filaments found in muscle sarcomeres [95, [100, [197, [198, [199]. Based on in vitro studies with purified motor, NM2 filaments are composed of relatively small numbers (~10s) of molecules, which self-associate via their long coiled-coil tail domains, leaving their N-terminal motor domains grouped at either end; the resulting structures extend 290–320 nm end-to-end [1]. In this configuration, NM2 motor groups are capable of generating opposing forces of equal magnitude on actin structures bound by opposite ends of the bipolar filament, such as the rootlets of microvillar core bundles.

Our super-resolution imaging studies of native intestinal tissues revealed striking networks of NM2C puncta in the circumferential/junctional band [83], as well as the medial terminal web (Figure 3-2). Given that NM2C in the mouse model employed here is tagged on its C-terminus with EGFP, these puncta likely mark the center positions of bipolar filaments. Nearest neighbor measurements indicate that adjacent puncta in both junctional and medial populations are separated by comparable mean distances (204 vs. 212 nm, respectively; Figure 3-2), suggesting that these networks may be organized in similar ways. This is further supported by our FRAP studies of NM2C-EGFP dynamics in organoid monolayers, which showed that the turnover kinetics for these two populations are comparable. These similarities in spatial organization and turnover kinetics suggest that the junctional and medial populations of NM2C may be functionally analogous. Because the junctional band of NM2C is an established contractile array [44, [83, [200], these points might additionally argue that medial/terminal web NM2C is

also capable of exerting force on the rootlets of microvillar actin core bundles. We also note here that the interpuncta NM2C spacing measured in our samples (~210 nm) is shorter than the mean length of NM2C filaments measured in vitro (~290 nm) but comparable to the length of the NM2C filament bare zones [1]. The super-resolution measurements of puncta spacing reported here are also smaller than previous measurements on the NM2C junctional network in intestinal or stomach epithelial tissues (~400–500 nm; [83]). The large range of spacing measurements from distinct biological contexts suggests a high degree of plasticity in NM2 contractile network organization, which probably reflects specific mechanical needs in these different environments.

Contractility-dependent actin turnover as a conserved function for NM2

Our experiments with NM2 activation (calyculin A, 4-HAP) and inhibition (blebbistatin) demonstrate that tuning the level of myosin contractility in polarized epithelial cells has a profound impact on microvillar length, with higher activity leading to shorter protrusions. Although calyculin A and blebbistatin both exert effects on all NM2 isoforms [179, [184], previous proteomic characterizations of brush borders isolated from mouse small intestine indicate that NM2C is by far the most abundant isoform in this system (~3-fold greater than NM2A, ~12-fold greater than NM2B; [165]); this is further confirmed by the scRNAseq data we present here (Figure 3-1). Moreover, our localization studies performed in W4 cells demonstrate that NM2C specifically enriches in the terminal web, whereas NM2A exhibits a nonpolarized distribution over the entire cell cortex (Figure 3-4, A vs. C). Taken together with our overexpression studies that establish NM2C is capable of shortening microvilli when present at high levels (Figure 3-9, B and G), we

conclude that the effects of drug treatments reported here primarily reflect an impact on NM2C activity in the terminal web.

The idea that NM2 activity can promote actin network turnover is broadly consistent with findings from other diverse systems. Indeed, previous studies on mechanisms of neuronal growth cone motility showed that the rate of actin turnover (i.e., the treadmilling/retrograde flow rate) at the leading edge decreases by ~50% when cells are treated with blebbistatin [201]. In this system, blebbistatin exposure also resulted in a striking elongation of filopodial actin bundles from their basal ends, which are normally embedded in a meshwork of lamellipodial actin filaments. NM2 contractility has also been implicated in the disassembly of actin filaments at the apical junctional complex in response to Ca²⁺ depletion [202] and in the recycling of filaments that is required for normal contractile ring constriction during cytokinesis [112, [113]. Thus, the NM2C-dependent microvillar length control mechanism that we identify here represents a new facet of a broadly conserved class of function for filament-forming NM2 isoforms.

Potential mechanisms for NM2-driven contractility-dependent actin turnover

How does NM2C activity promote the shortening of microvillar actin bundles? Previous work established that growing and nascent microvilli are supported by highly dynamic core bundles of parallel actin filaments, which collectively exhibit robust treadmilling [52, [203]. In treadmilling actin networks, new subunits incorporate at filament barbed ends, whereas disassembly dominates at the pointed ends. If assembly and disassembly rates are matched, the steady-state length of the structure can remain

constant. To shorten a treadmilling bundle, the assembly rate must decrease, or the disassembly rate must increase (or some combination of the two). On the basis of its localization, we propose that NM2C activity shortens microvilli by accelerating, either directly or indirectly, core actin bundle disassembly in the terminal web; under normal conditions this activity would contribute to actin bundle treadmilling and turnover. This is consistent with our observations showing that the robust turnover dynamics of W4 microvillar actin bundles is attenuated following blebbistatin treatment (Figure 3-7F).

NM2C might act directly on microvillar actin filament pointed ends to drive their disassembly in the terminal web. Previous *in vitro* studies with purified actin and myosin-2 established that motor activity alone is capable of promoting filament disassembly [204]. Interestingly, NM2C does exhibit kinetic properties (a moderate duty ratio and potentially strain-sensitive catalytic cycle) that would allow it to strain actin filaments [1]. NM2C could also function indirectly by promoting the activity of other factors capable of disassembling filaments. This would be supported by recent studies on *Aplysia* growth cones that revealed that NM2 contractility can enhance the localization and severing activity of the severing protein cofilin [205]. The proposed mechanisms by which NM2 might promote cofilin activity are based on its competition with cofilin binding, which creates distinct stiff and compliant zones (cofilin undecorated vs. decorated, respectively) along the filament, which are mechanically susceptible to severing at the boundaries of these regions [206, [207, [208]. Although there are currently no data to support a role for cofilin in controlling the length of epithelial microvilli, this could be one area of focus for future studies.

Additional roles for NM2C in polarized epithelia

In addition to promoting the turnover of actin filaments that constitute the microvillar core bundles, NM2C might also participate in other roles critical for normal epithelial cell polarization and function. For example, we noticed that microvilli undergo a striking dispersion across the cell surface in response to blebbistatin treatment (Figure 3-7, A–C). Thus, by binding directly to core actin bundles, NM2C might play a role in apicobasal polarity reinforcement and constraint of the size of the apical domain [202]. NM2C could also contribute to the organelle exclusion properties of the terminal web. The high density of cytoskeletal (actin and intermediate) filaments in the terminal web creates a zone of organelle exclusion that prevents endomembrane compartments from making direct contact with the apical surface. If NM2C forms filaments that span the gaps between microvillar rootlets, these structures might participate in regulating the movement of vesicles through this region. Interestingly, the presence of a terminal web meshwork is a unique feature of the intestinal epithelium; other brush border–presenting cells, such as those lining the kidney proximal tubule, lack a terminal web and zone of organelle exclusion [24, [25]. Importantly, these organs also lack strong NM2C localization, suggesting that NM2C may play a specific role in the compartmentalization of subcellular space in the intestinal epithelium [166].

Deeper insight into how NM2C contributes to epithelial physiology will come from careful analysis of in vivo loss-of-function models. Although a mouse model null for MYH14 expression was previously described, the authors reported no overt physiological phenotypes [81]. Other studies with the same KO mouse model revealed that in the absence of NM2C, NM2A and NM2B exhibit elevated levels in the intestinal epithelium as assessed by immunofluorescence signal [83]. Thus, an apparent lack of

overt phenotypes at the whole animal level may be due to functional compensation by NM2A and NM2B. Phenotypic characterization of the NM2C KO mouse represents an exciting direction for future studies and might also provide a unique opportunity to investigate how the epithelium responds to higher levels of NM2 contractility, as would be expected based on the accelerated kinetic properties of NM2B and NM2A relative to NM2C [1, [161].

CHAPTER 4

NON-MUSCLE MYOSIN-2C CONSTRAINS CELL- AND TISSUE-SCALE MORPHOLOGY IN THE SMALL INTESTINAL EPITHELIUM

INTRODUCTION

The vertebrate intestinal tract has an elaborate morphology, evolved to maximize the area available for nutrient absorption and allow for the plasticity required to recover from disease and infection, which can destroy the integrity of the epithelium [122, [125]. Beyond solute uptake, the intestinal epithelium also serves as an important barrier to luminal microbes and pathogens that might gain access to this space. Maintenance of the epithelial barrier is critical, as any breaches in the barrier will result in infection and inflammation, resulting in poor health outcomes [209, [210, [211]. Unlike the skin, another prominent epithelial barrier, the intestine only contains one layer of polarized cells, which must ultimately serve as both the first and last line of defense against invading luminal pathogens [209].

The small intestine contains finger-like villi, fed by crypts of Lieberkühn, which contain LGR5+ stem cells [212, [213]. Both of these features are highly specialized, and their development has been studied in detail. In vertebrates and other model organisms, crypt morphogenesis and villus formation (i.e., villification) occur separately [127, [128]. Villification, the process in which villi emerge from the previously smooth luminal surface of the embryonic gut tube, occurs in early embryonic development, driven by compressive stress that leads to tissue buckling [127]. The exact process and timeline

vary by species. In contrast to the embryonic development of villi, crypts are known to develop postnatally. Indeed, the natal inter-villus regions undergo myosin-2 driven apical constriction, resulting in the development of tissue invaginations that form crypts [128].

Migration is a critical component of development, and in the intestine, migration persists throughout an organism's lifespan. As the LGR5+ stem cells differentiate, they migrate out of the crypt, up the villi, and finally undergo apoptosis and shed off at the tips [123]. This process of crypt to villus migration is critical for intestinal homeostasis and regenerative renewal of the epithelium. Additionally, the constant turnover of cells resulting from crypt to villus migration enables the intestine to remain a dynamic organ, which is vital for its function. For example, it has been shown in a variety of animal models that changes in villus length occur as a result of fasting and feeding behaviors [142, [146, [147, [148, [149, [150, [151, [214]. Villi can regain lost length in as little as two hours after refeeding [151]. Classically, it was assumed that these changes in length occur due to increased cell shedding rate (to shorten) or increased cell proliferation rate (to lengthen) [215]. However, it was previously found that the rate of cell production did not increase until 12hrs after refeeding, suggesting that there may be additional mechanisms that allow for villus lengthening shortly after refeeding [151]. Related to this, the entire crypt to villus migration process was thought to be driven by mitotic pressure from dividing transit-amplifying cells in the crypt [132, [216]. Additionally, recent studies have demonstrated that crypt-villus migration is driven by active Arp2/3 driven cell protrusion at the basolateral surface of enterocytes [131]. Despite recent progress, crypt-villus migration remains poorly understood, despite its

critical role in tissue homeostasis. To date, it has been assumed that once villi emerge during embryogenesis, they passively maintain their somewhat cylindrical shape, and no studies have investigated if active mechanisms are required for villi to keep their stereotyped appearance during the continuous process of crypt to villus migration.

Migration of epithelial sheets has been well-described using model organisms such as *Drosophila melanogaster*, as well as cultured systems such as MDCK cells [217, [218]. Inhibition of cell adhesion has been noted to disrupt migration, and modulation of molecules such as epithelial cell adhesion molecule (EPCAM) can change the rate of epithelial cell migration [219, [220]. Well-defined cell junctions are considered a key feature of epithelial sheets, necessary for morphogenesis [221]. Indeed, early work noted that stable cell adhesion was required to maintain crypt-villus migration and thus maintain homeostasis of the intestinal epithelium [222]. Additionally, changes in the expression levels or localization of cell-adhesion molecules such as E-cadherin and α -catenin have been noted in a variety of gastrointestinal diseases, such as Crohn's disease and ulcerative colitis [222, [223]. Indeed, it has been shown that cell-cell interactions are a critical facet of the dynamic processes required for maintenance of the intestinal epithelium and pathophysiological situations that require repair of the epithelium [222].

Intestinal epithelial cells have three functional junctions on their lateral surface: the zonula occludens (also known as tight junction), the zonula adherens (also known as the adherens junction), and the desmosome [224]. Tight junctions are closest to the apical surface and maintain the intestinal barrier while allowing for selective permeability of small ions, nutrients, and water [223]. A variety of pathogens also target the tight

junctions; thus, changes in the stability or permeability of the tight junctions can result in disease and inflammation of the underlying submucosa [225]. The adherens junction lays below the tight junction and is known to play an important role in anchoring cells together during morphogenesis or migration [117]. Desmosomes underlay the adherens junction and serve to couple cell-cell adhesion to the intermediate filament network [226]. Due to these multifaceted roles that the intestinal epithelium must perform, cellular junctions are critical points that must maintain selective permeability for ions [210] while simultaneously holding a sheet of continuously migrating cells together [227]. A defect in junctional stability results in a tissue that is vulnerable to pathogen invasion [228] and potentially structurally unstable and unable to support the migration required for intestinal homeostasis. Importantly, cell-cell junctions are known to be mechano-regulated [229]. Tension is generated by class 2 myosins in an actomyosin contractile ring that is coupled to the adherens junction. This tension is required for junctions to mature during development, and previous work has demonstrated that modulating myosin activity is sufficient for generating changes in junctional stability and permeability [83, [110, [202, [230].

Class 2 myosins comprise a family of actin-based motor proteins that provide the contractile force necessary for a variety of biological processes, including cytokinesis, cell migration, and adhesion. In a variety of model organisms, including *Drosophila*, *C. elegans*, and vertebrates, myosin-2 is implicated in a wide range of critical morphogenesis events that occur during development. In *Drosophila*, non-muscle myosin-2 (NM2, encoded by zipper) plays an important role in wing disk development [231] and convergent extension [232]. In vertebrates, the three paralogs of NM2 are

known to have developmental roles and play a role in a variety of human diseases [65, [73]. NM2 paralogs are known to play a critical role in the formation and stability of cell-cell junctions, as well as the three-dimensional organization of a variety of epithelial tissues [108, [109, [232]. Additionally, myosin light chain kinase (MLCK), a key regulator of M2 activity, has been implicated in a variety of gastrointestinal ailments, including irritable bowel disease [230, [233].

Non-muscle myosin-2C (NM2C) is the most recently described member of the myosin-2 family. NM2C has remarkably specific expression, particularly in comparison to non-muscle myosin-2A (NM2A) and non-muscle myosin-2B (NM2B), which are expressed ubiquitously in higher-order mammals [1]. In contrast, NM2C is expressed primarily in the intestinal epithelium and the sensory epithelium of the inner ear [166]. In the inner ear, NM2C and NM2A were found to be asymmetrically distributed between cell types, and disruption of NM2 activity resulted in defects in cellular patterning, suggesting that NM2A and NM2C play various roles in cochlear development, particular in convergent extension of the sensory epithelium in embryogenesis, and the establishment of cell-cell boundaries [84]. Early work on NM2C established that it forms a sarcomeric array at cell junctions in both the small intestine and the inner ear [83]. Using the myosin-2 inhibitor blebbistatin, they determined that under homeostatic conditions, this junctional band of NM2C is under tension [83]. Indeed, this is confirmed by more recent work that demonstrated that the villus epithelium is always under tension at cell-cell junctions [131]. Recently, we demonstrated that NM2C is localized to the terminal web of enterocytes and implicated NM2C in the control of microvillar length via contractility-dependent actin turnover [234]. Using super-resolution microscopy, we

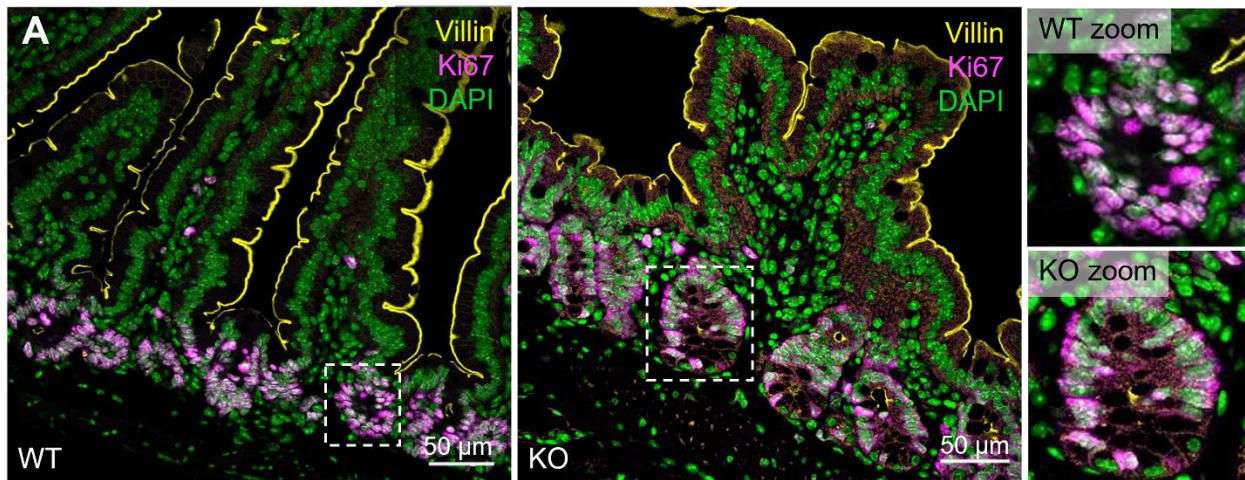
revealed that the plate of terminal web myosin is continuous with the circumferential population of NM2C that has been previously studied.

In this paper, we report that knockout of NM2C results in abnormal intestinal morphology, a phenotype that increases in severity as the animals age. This finding is of particular interest, as mutations in NM2C have been found to cause progressive hearing loss, and it has been noted in the past that sensory loss is often comorbid with gastrointestinal symptoms [235, [236], but the sensory loss is more likely to capture the attention of patients and clinicians. We find that NM2C KO mice display ruffled ZO-1 signal via immunofluorescence, suggesting malformed cell-cell junctions. Consistent with loss of junctional integrity and a loss of barrier function, NM2C KO animals display tuft cell and goblet cell hyperplasia. Interestingly, intestinal organoids generated from NM2C KO animals also display tuft cell hyperplasia. These intestinal organoids display abnormal morphology when compared to wild-type (WT). We performed high-resolution live imaging of KO and WT organoids and found that cells in the “villus domain” of NM2C KO organoids display aberrant actin dynamics. These data demonstrate that NM2C plays a unique role in maintaining intestinal morphology, possibly due to its role in maintaining tension across cells in the epithelial sheet. Additionally, these studies reveal that villus shape is not inherently stable, and we propose that it must be actively maintained as cells undergo crypt-villus migration.

RESULTS

NM2C KO mice display abnormal gross intestinal morphology.

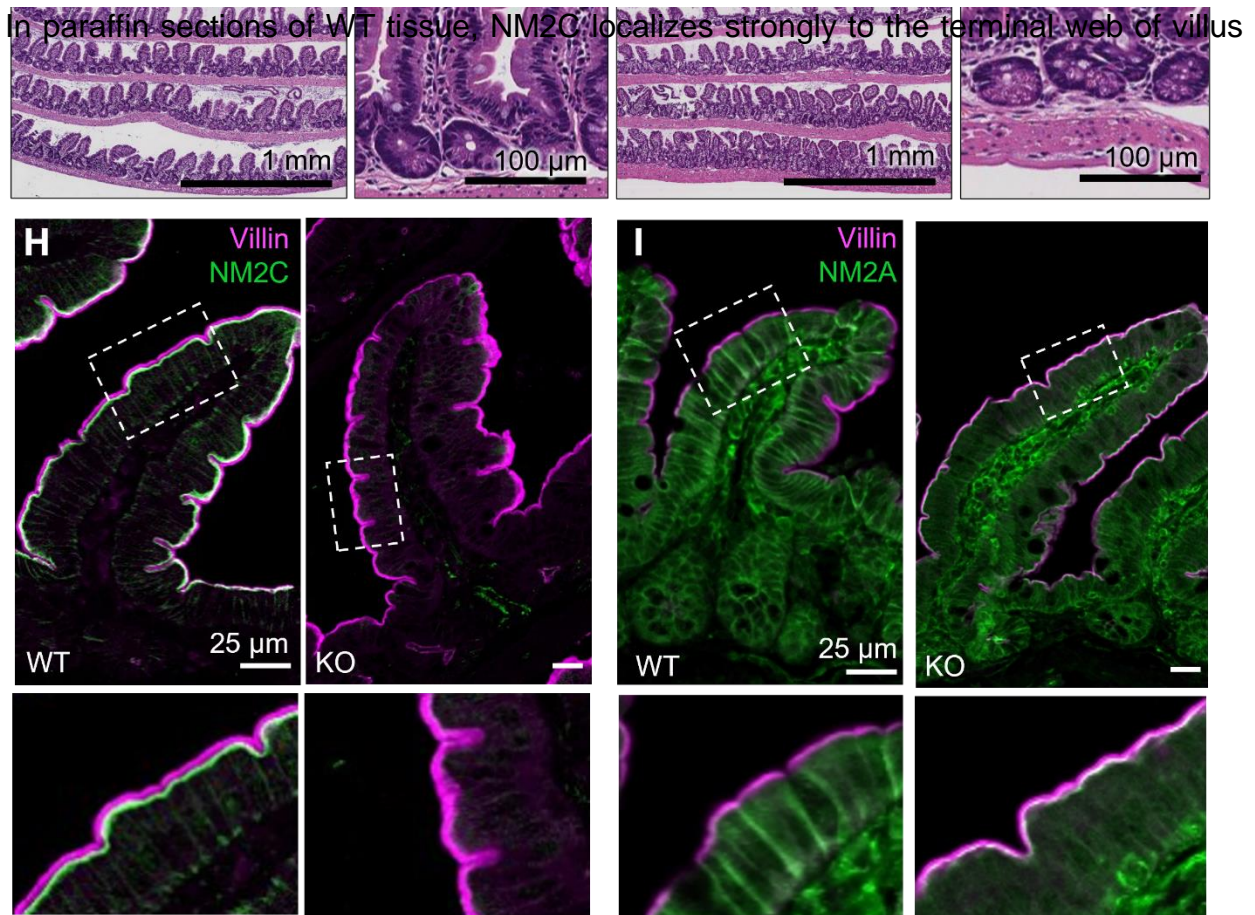
We used NM2C KO mice that had been previously generated and briefly described in Ma et al. 2010. Despite previous work stating these mice has no “gross morphological changes” [81, [128], we found that homozygous NM2C KO mice trend towards being smaller than their wild-type C57/B6J (WT) counterparts, and differences in weight become more significant as the animals age (Figure 4-2A and 4-2B). Haemotoxylin and eosin staining of NM2C KO and WT small intestinal swiss rolls reveal that NM2C KO animals have abnormal villus morphology, including “forked” villi (Figure 4-2F and 4-2G). Additionally, KO animals have significantly larger villi compared to WT animals (Figure 4-2E), fewer villi per mm of intestine (Figure 4-2C), and deeper crypts (Figure 4-



2D), which contain Ki67+ cells, indicating they are proliferative (Figure 4-1A).

Figure 4-1 Crypts of WT and KO mice are positive for proliferative marker, Ki67. A, Comparative images of FFPE tissue stained for villin (yellow), Ki67 (magenta) and DAPI (green). Far-right, zooms of crypts from WT tissue and KO tissue, respectively. Ki67 is present in all crypts, indicating that they are proliferative.

Figure 4-2: NM2C KO mice display abnormal gross intestinal morphology. **A**, representative image of 2-month-old WT and KO mice. **B**, Quantification of weight of KO vs WT mice at 2 months and 4 months. All other quantifications are done using tissue from 2-month-old animals, unless explicitly stated. **C**, Quantification of villi per mm of intestine, as measured on H&E stained swiss rolls. **D**, Quantification of crypt depth in WT and KO animals, measured from H&E swiss rolls. **E**, Quantification of villus area, measured from H&E stained swiss rolls. **F**, representative zooms of H&E stained swiss roll of entire WT intestine, demonstrating homogenous morphology as expected in the small intestine. **G**, representative zooms H&E stained swiss roll of entire KO intestine, demonstrating unusually shaped villi. **H**, FFPE tissue stained for NM2C and villin to mark the brush border. As expected, NM2C lays underneath the villin signal in WT tissue, and is completely absent in KO tissue. Scale bars are 25 μ m, KO villi scaled in order to fit entire villus in single image. **I**, FFPE tissue stained for NM2A and villin to mark the brush border. NM2A primarily localizes to the basolateral surfaces in WT tissue, and redistributes to the terminal web in NM2C KO tissue. Scale bars are 25 μ m, KO villi scaled in order to fit entire villus in single image. Unpaired t-test with Welch's correction (B) or unpaired t-test (C,D,E) used to determine significance. * = $p=0.0109$, **= $p=0.0079$, ***= $p=0.0002$, ****= $p<.0001$



enterocytes (Figure 4-2H, first column), whereas NM2A, which has been implicated in crypt morphogenesis [128], is enriched in the lateral membranes and basolateral domain of villus enterocytes (Figure 4-2I, first column), as well as demonstrating strong localization in crypt cells. Terminal web labeling of NM2C is completely lost in KO mice, further confirming the loss of expression (Figure 4-2H, second column). Due to the high levels of similarity in sequence and function of NM2A and NM2C, we sought to examine if NM2A compensates for the loss of NM2C in the terminal web. As expected, in KO animals, NM2A appears to compensate for the loss of 2C in the terminal web, but interestingly, it no longer displays a strong localization to the lateral surfaces (Figure 4-1I, second column). This suggests that the presence of a force-generating motor in the terminal web is the priority for the cell, and when presented with a limited supply of myosin, the cell will place these motors at the apical surface rather than the lateral contacts.

Whole-mount imaging reveals the extent of three-dimensional morphology changes.

Upon observation of abnormal villus shape in paraffin-embedded sections, we sought to ensure that these perceived shape changes were not due to sectioning artifacts. For this, we turned to whole-mount imaging of the intestinal epithelium. Whole-mount imaging provides three-dimensional data that is otherwise lost in sectioning while also allowing for immunofluorescent staining that would not be possible using scanning electron microscopy (SEM), which also allows for visualization of the intestine in its native three-dimensional state.

We sought to determine if the abnormal villus shape observed in paraffin sections from 8-week-old animals was due to an initial developmental defect. We chose to use P10

animals as an initial early time point, as these animals should have completed crypt morphogenesis [128]. Interestingly, no major differences in shape could be seen when P10 WT and KO intestines were evaluated (Figure 4-3A). Indeed, previous work by Sumigray et al. also examined this KO mouse line, but only during early post-natal stages, where no differences were noted between WT and KO animals. However, we found that by 8 weeks, differences could clearly be observed between WT and KO intestine, included shortened villi with abnormal levels of folding (Figure 4-3A). Indeed, in 4-month-old animals, it was also observed that KO animals had exceptionally wide, shortened villi when compared to WT age-matched animals (Figure 4-3A). These data suggest that NM2C KO mice develop normally and exhibit morphological changes as a function of age.

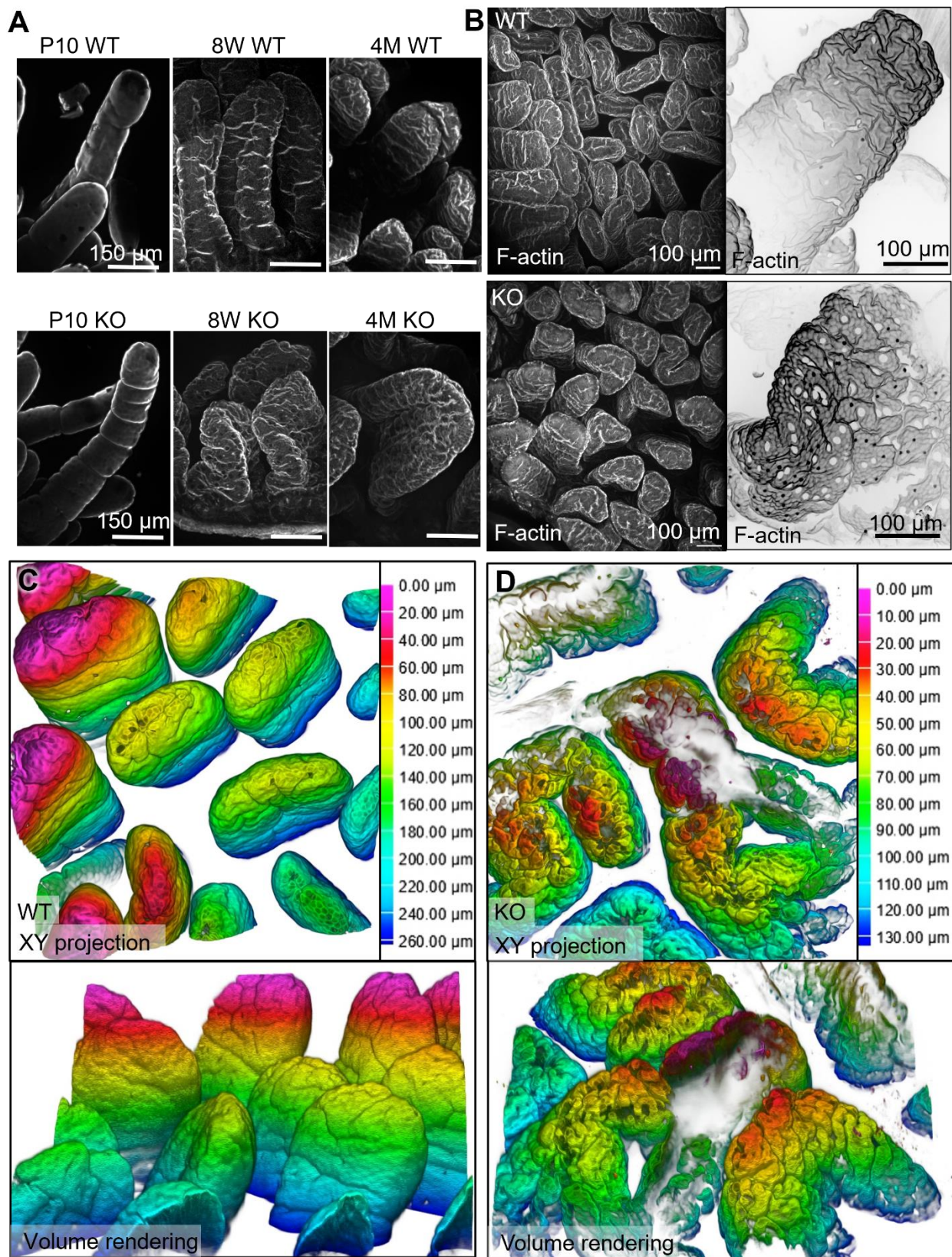


Figure 4-3 :Whole mount imaging reveals extent of three-dimensional morphology changes. **A**, comparative maximum intensity projection images of WT and KO whole mount tissue from post-natal day 10, 8 weeks (2 months) and 4 months. All scale bars are 150 μ m. KO villi continue to enlarge after time points at which WT villi maintain a consistent size. **B**, representative 10x (first column) and 25x (second column) maximum intensity projections of WT and KO whole mount tissue. 10x images demonstrate the variety of KO villus morphology, while 25x images demonstrate changes in the scale and morphology of a single villus. **C**, ,Top, depth-coded F-actin signal from WT tissue projected in the XY-plane, bottom, depth-coded f-actin signal rotated and viewed as a volume rendering using Nikon Elements. **D**, ,Top, depth coded F-actin signal from KO tissue projected in the XY-plane, bottom, depth code f-actin signal rotated and viewed as a volume rendering using Nikon Elements. Note that depth coding is different between **C** and **D**.

In low magnification images, it is evident that KO villi display a greater degree of heterogeneity compared to WT villi (Figure 4-3B, first column). In addition, there are fewer KO villi per field of view, which confirms the phenotype noted in H&E sections. Interestingly, in higher magnification images, it is apparent that the KO villi appear somewhat blunted and wide, in addition to being extraordinarily pitted compared to those of WT animals (Figure 4-3B, second column). Indeed, depth-coded maximum intensity projections emphasize that the KO villi are shorter than those of the WT (Figure 4-3C vs. 4-3D, top row). Furthermore, the KO villi display a variety of odd shapes, including the triangular orientation seen in Figure 4-3D. Rotated volume renderings emphasize the homogenous nature of WT villi, whereas the KO villi display a variety of geometries and orientations (Figure 4-3C vs. 4-3D, bottom row). Thus, we conclude that loss of NM2C alters the ability of the intestinal epithelium to maintain its complex shape during aging, leading to defects in villus shape.

NM2C forms a continuous layer across the apical surface.

Previously, we demonstrated that NM2C is enriched in the terminal web of enterocytes, which spans the medial apical surface of the cell. Additionally, we confirmed that NM2C is a component of the junctional actomyosin contractile belt, which had been observed previously [83]. Here, we sought to confirm, using whole-mount imaging, that the NM2C population found in the junctional actomyosin belt was in the same plane as the medial population. We found that the junctional population of NM2C appears to be continuous with the terminal web population (Figure 4-4A). Indeed, in cases where epithelial cells had begun to separate from the sheet, we observed that the NM2C signal was present in a single sheet, even once the cells appeared entirely separated from their neighbors (Figure 4-4B). Thus, from these data and those already in the literature, we conclude that the entire apical population of NM2C is continuous, which would result in continuous tension being propagated across the cell surface, and indeed, across the entire epithelial sheet.

We sought additional information about the physical location of NM2C compared to other junctional proteins, such as ZO-1. Here, we use whole-mount imaging and oversampling on a point scanning confocal to precisely localize both NM2C and ZO-1. Indeed, junctional NM2C and ZO-1 colocalize slightly (Figure 4-4C, top), with more NM2C localized below the ZO-1 signal (Figure 4-4C, bottom), indicating the NM2C is physically located such that it may be able to directly control the amount of tension on the tight junction (Figure 4-4D).

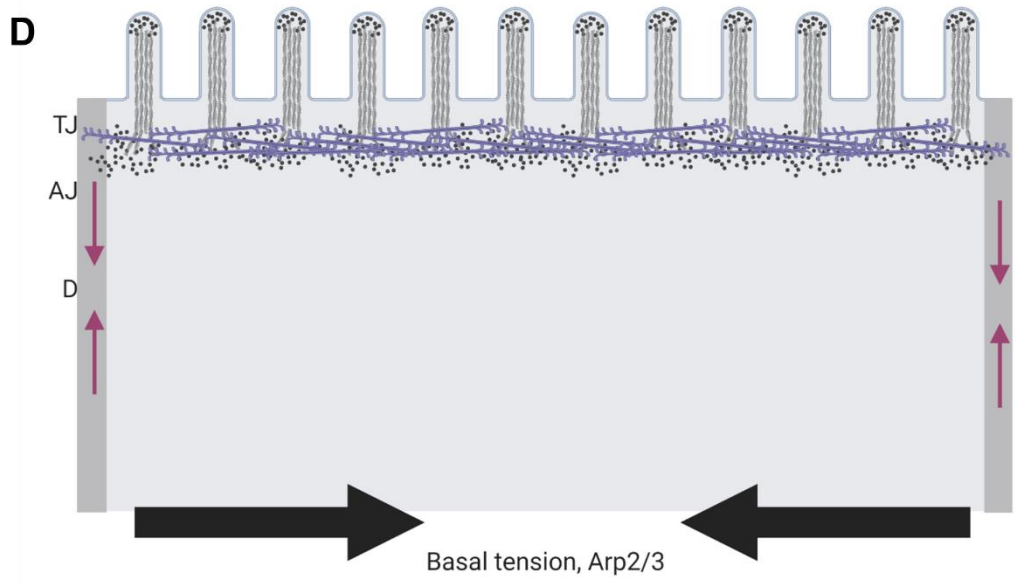
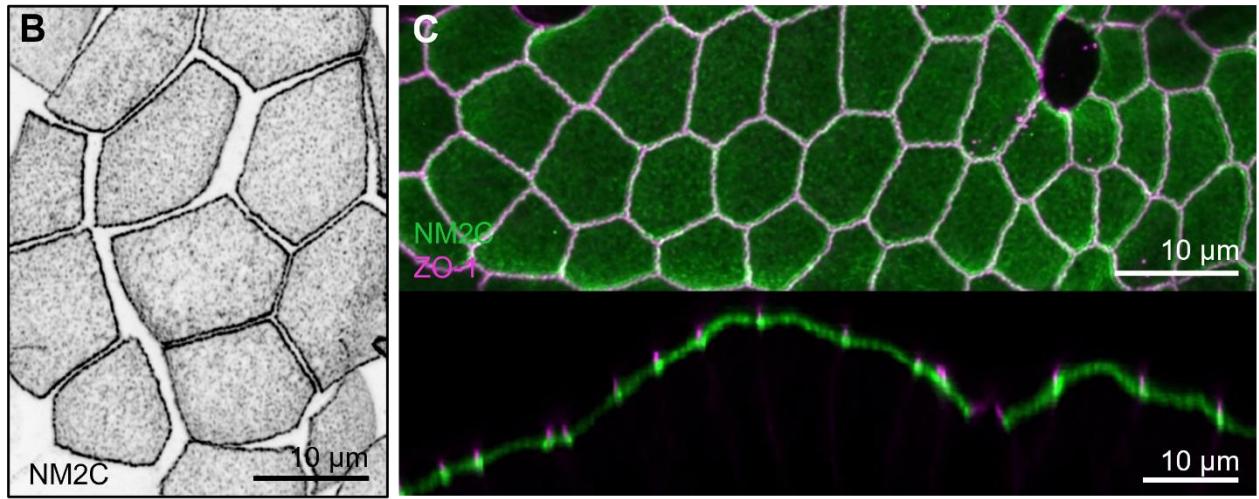
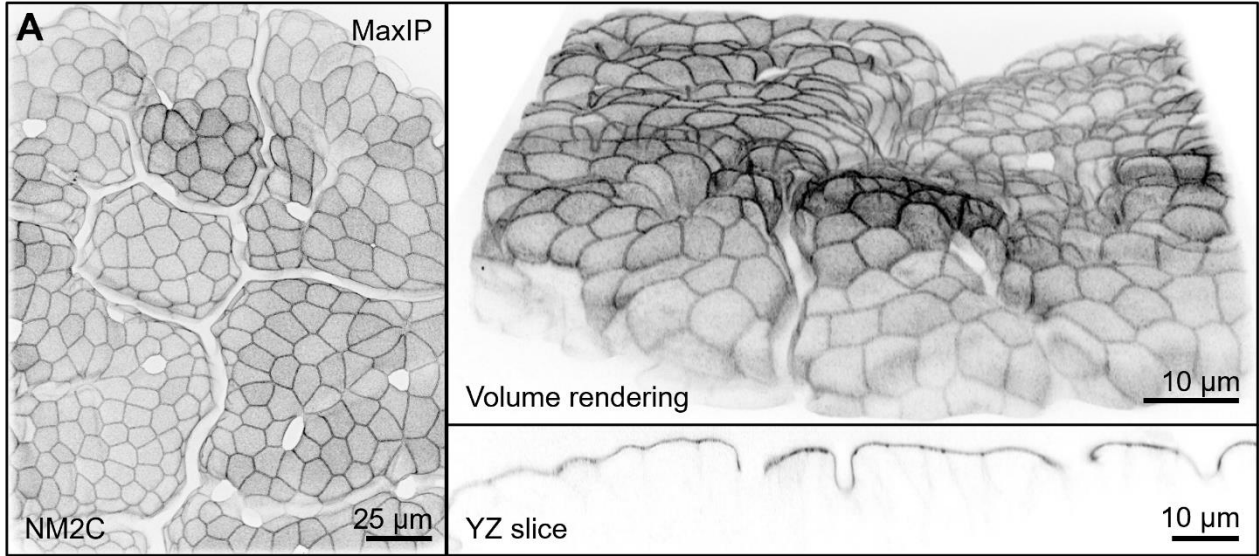


Figure 4-4: NM2C forms a continuous layer. **A**, first row, maximum intensity projection of whole mount imaging of villus surface from NM2C-GFP mouse, second row, when rotated in a volume rendering (top), NM2C signal appears to be continuous across the epithelial surface of the villus. An YZ slice of this image reveals the bright junctional puncta are in line with the medial NM2C population, indicating that they likely interact and influence each other. **B**, Disassociated enterocytes from NM2C-GFP mouse, demonstrating how entire NM2C signal stays in a sheet even once the cells have physically separated from each other, and no longer have junctional contacts with neighboring cells. **C**, maximum intensity projection (top) of NM2C-GFP (green) whole mount tissue stained with a ZO-1 antibody (magenta), YZ slice (bottom) displays location of NM2C and ZO-1 in Z, where classic ZO-1 spot wells appear to be sitting on a “cup” of junctional NM2C signal. **D**, cartoon schematic of NM2C that reaches across the terminal web and ties in the junctions right below the tight junction. Large arrows indicate basal forces, small arrows indicate lateral forces.

Loss of NM2C disrupts apical ultrastructure.

The terminal web population of NM2C has been previously implicated in the control of microvillar length; thus, we chose to investigate if loss of NM2C impacts apical ultrastructure using transmission electron microscopy (TEM). TEM sections of WT and KO were acquired parallel to the microvillar axis in order to allow for evaluation of microvillar length and terminal web architecture (Figure 4-5A and 4-5B). Here, we define a microvillus as the portion of the actin bundle wrapped in membrane (Figure 4-5C). Strikingly, microvilli in NM2C KO brush borders were significantly shorter than those in the WT (Figure 4-5E, 0.7740 ± 0.26 vs. $0.9899 \pm .17$). Furthermore, KO microvilli length varied much more than WT microvilli, with KO microvilli having a range of 1.25 vs. .66 in WT brush borders (Figure 4-5E). Next, we examined the length of actin rootlets, which are the portion of the microvillar actin bundle that extends into the terminal web and is not wrapped in membrane (Figure 5-4C). Interestingly, KO brush borders had significantly longer actin rootlets than those of WT animals (Figure 4-5D, 0.2678 ± 0.083 vs. 0.2114 ± 0.062). Overall, KO brush borders were composed of shorter actin bundles

than WT brush borders (Figure 4-5F, 0.9790 ± 0.21 vs. 1.146 ± 0.18), again, with KO actin bundles have a much larger range of lengths (Figure 4-5F, 1.151 vs. 0.634).

To further analyze the ultrastructural defects, present in NM2C KO brush borders, we used a nearest neighbor distance calculation on en face TEM sections (Figure 4-5H and 4-5I) to obtain the intermicrovillar distance in KO and WT animals. KO brush borders exhibited a slightly larger intermicrovillar distance on average (Figure 4-5G, 132.6 ± 8.3 vs. 130.8 ± 5.3 , $p = 0.0091$). Furthermore, similar to the length measurements performed on parallel sections, KO brush borders had a much larger range of intermicrovillar distances (Figure 4-5G, 55.91 vs. 24.97 in WT animals). To further examine the impact of the increased range of intermicrovillar distances, we calculated fast Fourier transforms (FFT) of these images, as previously described [155, [237]. As expected, the FFT generated from WT brush borders exhibit a hexagonal pattern with six prominent first-order spots, indicating that WT microvillar are organized in hexagonal arrays, as expected (Figure 4-5H, last row). However, FFT generated from KO brush borders exhibit less distinct first-order spots, although they are still present (Figure 4-5I, last row). These data indicate that loss of NM2C disrupts the packing of enterocyte brush borders. Indeed, loss of NM2C results in a lack of homogenous brush border ultrastructure, with KO brush borders exhibiting extreme amounts of variability in microvillar packing, actin bundle length, and the portion of the actin bundle that is wrapped in membrane.

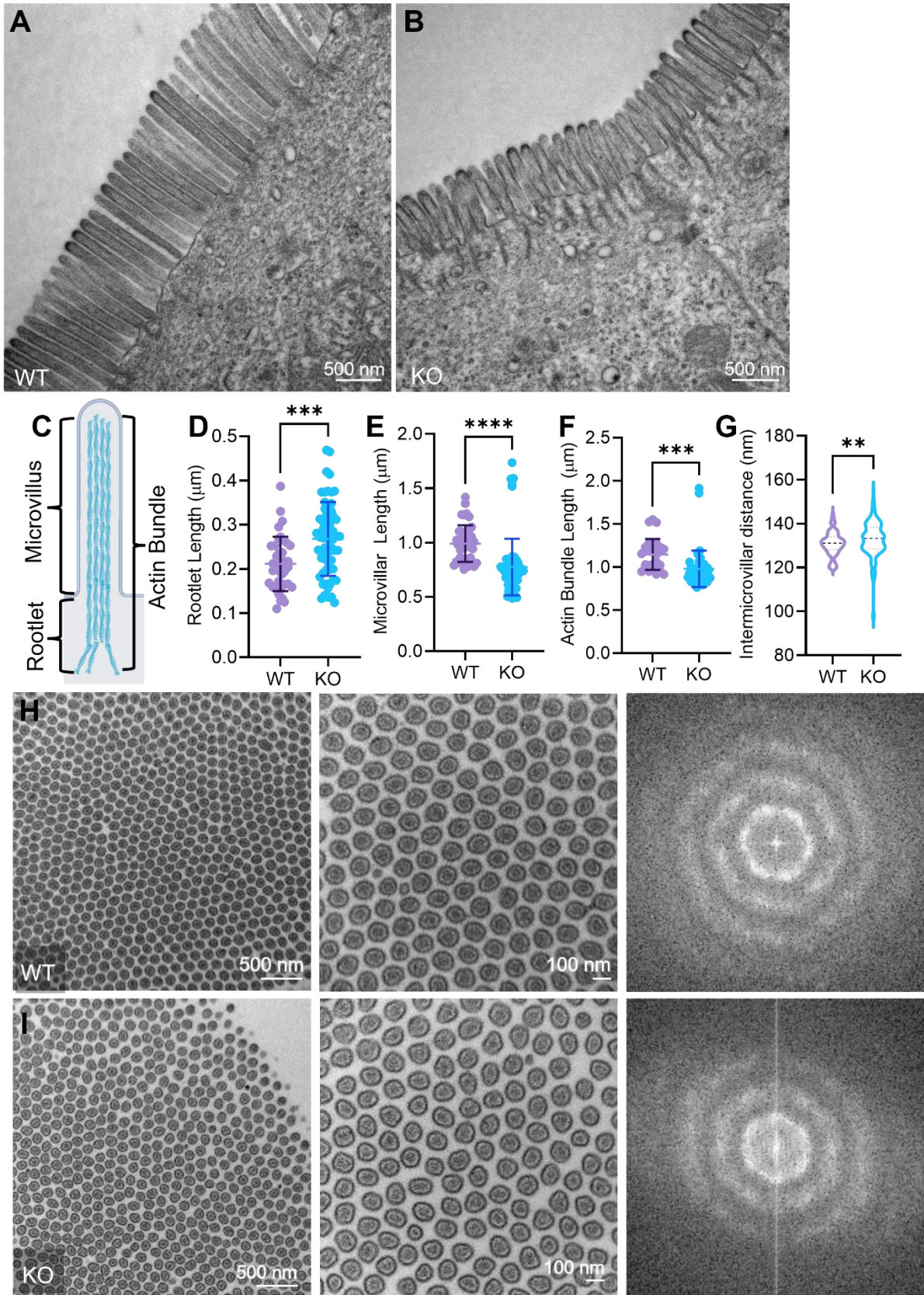


Figure 4-5: Loss of NM2C perturbs ultrastructure. **A**, representative TEM of WT microvilli in parallel. **B**, representative TEM of KO microvilli in parallel. **C**, cartoon schematic of how quantifications correspond to parts of the brush border. **D**, quantification of rootlet length. **E**, quantification of microvillar length. **F**, quantification of total actin bundle length. **G**, quantification of intermicrovillar distance. **H**, representative TEM of WT microvilli en face (first and second row), FFT of WT microvilli (last row), note that the first order spots are six distinct spots in a hexagonal pattern, indicating hexagonal packing. **I**, representative TEM of KO microvilli en face (first and second row), FFT of KO microvilli, note that the first order spots are less distinct indicating a possible packing defect. Unpaired t-test with Welch's correction used to calculate significance. **= $p=0.0091$, ***= $p=0.0002$, ****= $p<.0001$

Absence of NM2C alters cell shape and tissue integrity.

Frozen sections cut to 5 μ m thickness were stained with phalloidin to visualize F-actin. Using high-resolution confocal microscopy, we observed that enterocytes in the KO tissue displayed abnormal cellular morphology, including pointed apical domains and compressed and elongated lateral profiles (Figure 4-6A). Using full crypt-villus axis images of WT and KO tissue, we measured lateral cell area (Figure 4-6B) and aspect ratio (length/width) (Figure 4-6C). Importantly, cells that were measured were judged to be parallel to the imaging plane, to minimize the effects of any sectioning artifact. Previous data has shown that cell area and aspect ratio change along the crypt-villus axis [131]; thus, these measurements were only compared to cells located on a specific third of the villus. Even with this specification, cells in KO sections were significantly larger than the WT counterparts; this was consistent across all regions of a villus (Figure 4-6B). Additionally, KO cells had a significantly higher aspect ratio than matched WT cells, indicated that KO cells tended to be elongated and compressed on all parts of the villus (Figure 4-6C), although the difference between WT and KO cells was somewhat diminished at the top of the villus ($p = 0.0193$).

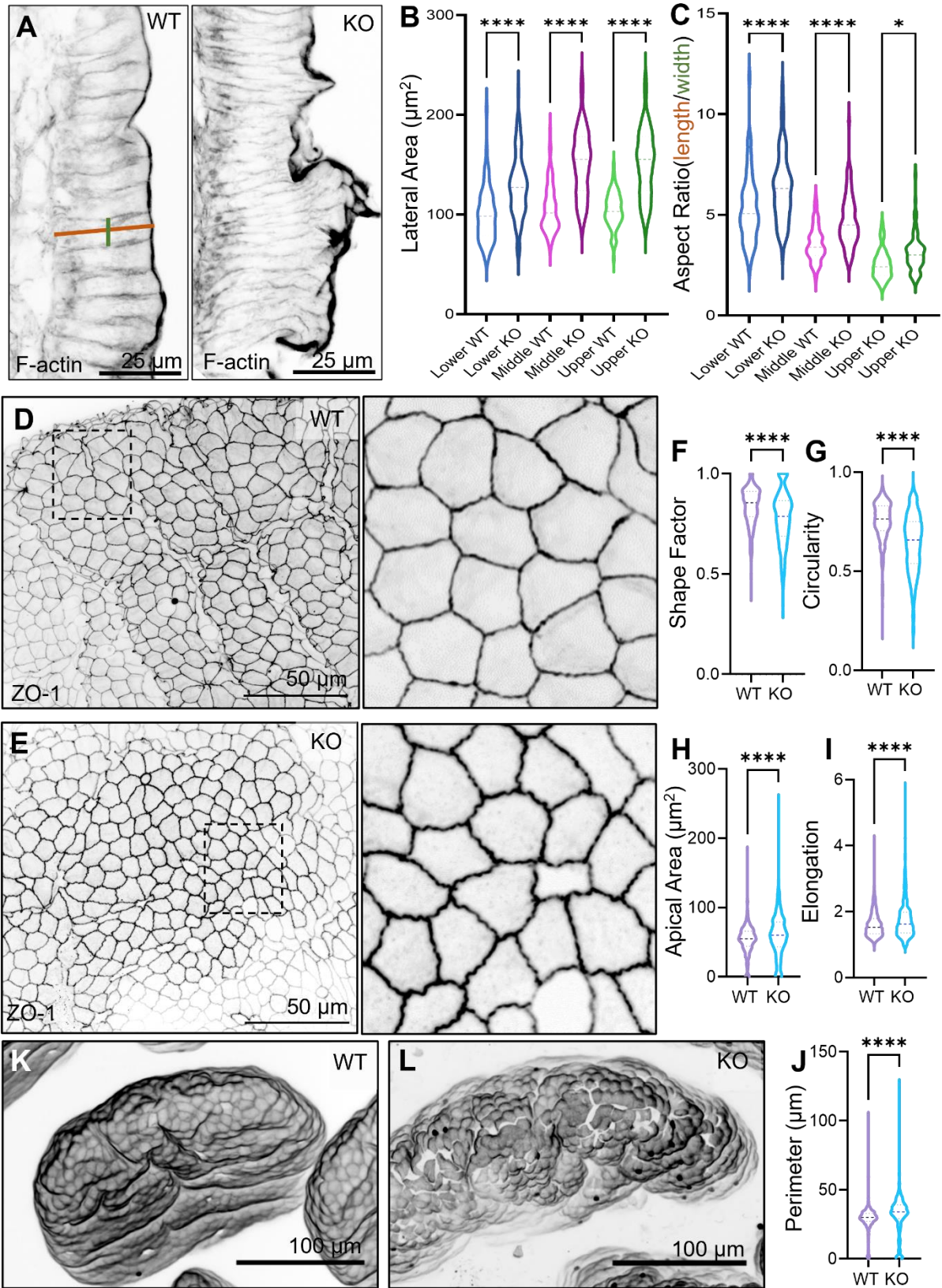


Figure 4-6: Loss of NM2C results in changes to cell shape and tissue integrity..

A, maximum intensity projections of parallel frozen sections, demonstrating the different in cell size and shape in WT and KO samples. **B**, Quantification of lateral area of cells on the villus, measured in thirds known to correspond with changes in cell size. **C**, Quantification of aspect ratio (length/width) of cells on the villus, measured in thirds known to correspond with changes in cell size. **D**, maximum intensity projection of WT villus surface, stained for ZO-1. Zoom demonstrates the relative straightness of cell boundaries. **E**, maximum intensity projection of KO villus surface, stained for ZO-1. Zoom demonstrates the irregular features of cell boundaries. The following quantifications were obtained from maximum intensity projections using thresholded ZO-1 signal to create a binary of the boundary of the cells, and measurements were done automatically in Nikon Elements. **F**, quantification of shape factor, which indicates how rough the outline of a cell is. A shape factor of 1 would indicate a completely smooth cell. **G**, quantification of circularity, a value of 1 would indicate a perfectly circular cell. **H**, quantification of apical area. **I**, quantification of apical area. **J**, quantification of cell perimeter. **K**, maximum intensity projection of whole mount WT villus that was allowed to sit in solution for 10 days prior to imaging. **L**, maximum intensity projection of whole mount KO villus that was allowed to sit in solution for 10 days prior to imaging. Note the cracking that is beginning to happen in the KO sample. Unpaired t-test with Welch's correction used to calculate significance. * $p=0.0193$, **** $= p<.0001$

To further investigate cellular morphology in KO animals, we turned again to whole-mount imaging. Here, we use an antibody targeted to ZO-1 to mark the margins of the cell (Figure 4-6D). Interestingly, we observed that ZO-1 signal in KO animals has a ruffled appearance, similar to a phenotype that is observed in other epithelial sheets when tension is misregulated or lacking (Figure 4-6E). We thresholded images using the ZO-1 signal and performed automatic measurements on the resulting binary objects using Nikon Elements. Here, shape factor is used as a measurement of an objects roughness: this is defined as $\frac{4 \times \pi \times \text{Area}}{\text{convex hull perimeter}^2}$ with a value closest to 1 indicating minimal roughness. Indeed, the shape factor measurement confirms that cells in KO tissue present with a rougher shape than those in the WT (Figure 4-6F, 0.77 ± 0.14 vs. 0.84 ± 0.09). Additionally, we found that KO cells were less circular than their WT counterparts (Figure 4-6G, 0.64 ± 0.15 vs. 0.75 ± 0.10), where a circularity

measurement of 1 would imply a perfectly circular object. Similar to the variation in lateral area, KO tissue displayed cells with, on average, a larger apical area than WT tissue (Figure 4-6H, 60.28 ± 31.73 vs. 53.76 ± 19.70), although KO tissue samples did demonstrate more variability in apical area than WT samples (Figure 4-6H, range of 249 vs. 178). Additionally, KO tissue contained cells that were more elongated (Figure 4-6I, 1.74 ± 0.55 vs. 1.61 ± 0.38) with larger perimeters compared to WT cells (Figure 4-6J, 32.10 ± 13.58 vs. 29.29 ± 7.89).

A small disadvantage of using whole-mount tissue is due to the storage conditions of the sample (in solution vs. frozen or paraffin-embedded); the usable lifespan of the tissue, once it is fixed, is somewhat limited when compared to more traditional tissue preparation methods. Typically, fixed whole-mount tissue has a usable lifespan of ~2 weeks post-fixation; after this point, the tissue is more liable to be mechanically damaged when handled. Curiously, we found that KO tissue was more delicate than tissue collected from WT animals. In Figure 4-6K and Figure 4-6L, we present a WT and a KO tissue sample that were fixed within 15 minutes of each other and allowed to remain in solution for 10 days. While the WT sample still appears completely intact (Figure 4-6K), the epithelial cells of the KO have begun to separate from each other, with the sample displaying large cracks (Figure 4-6L). This phenotype was consistent with KO samples that had been stored for greater than a week. Taken together, these data indicate that KO animals suffer from a loss of junctional integrity and that loss of NM2C alters cell morphology in addition to tissue morphology and brush border ultrastructure.

Aberrant growth and junctional defects are epithelial cell-autonomous.

To further understand the phenotype of the NM2C KO mouse, we turned to intestinal organoids. Our intent with these organoid cultures was to eliminate possible interaction with the mucosal immune system and investigate if those phenotypes observed in NM2C KO tissue could be recapitulated in a cell-autonomous manner, as intestinal organoids have few methods of compensation, unlike native tissue.

Beginning with low magnification phase microscopy, we observed that KO organoids (Figure 4-7B) grew to a much larger size than WT counterparts (Figure 4-7A), and frequently, KO organoids presented with aberrant morphology, such as split crypts. We then performed high magnification immunofluorescence imaging of fixed and live WT and KO organoids using spinning disk confocal microscopy. Typically, intestinal organoids present a luminal villus-like domain, in which enterocytes demonstrate a cobblestone-like brush border, with variable actin expression between cells (Figure 4-7C). However, even with the variation in actin expression in WT organoids, clear cell boundaries can still be distinguished using an F-actin marker such as phalloidin (Figure 4-7C, zoom). Interestingly, this stereotypical actin morphology was lost in organoids generated from KO mice (Figure 4-7D). No clear cell boundaries were able to be distinguished in the actin channel, and KO brush borders appeared extremely disorganized (Figure 4-7D, zoom).

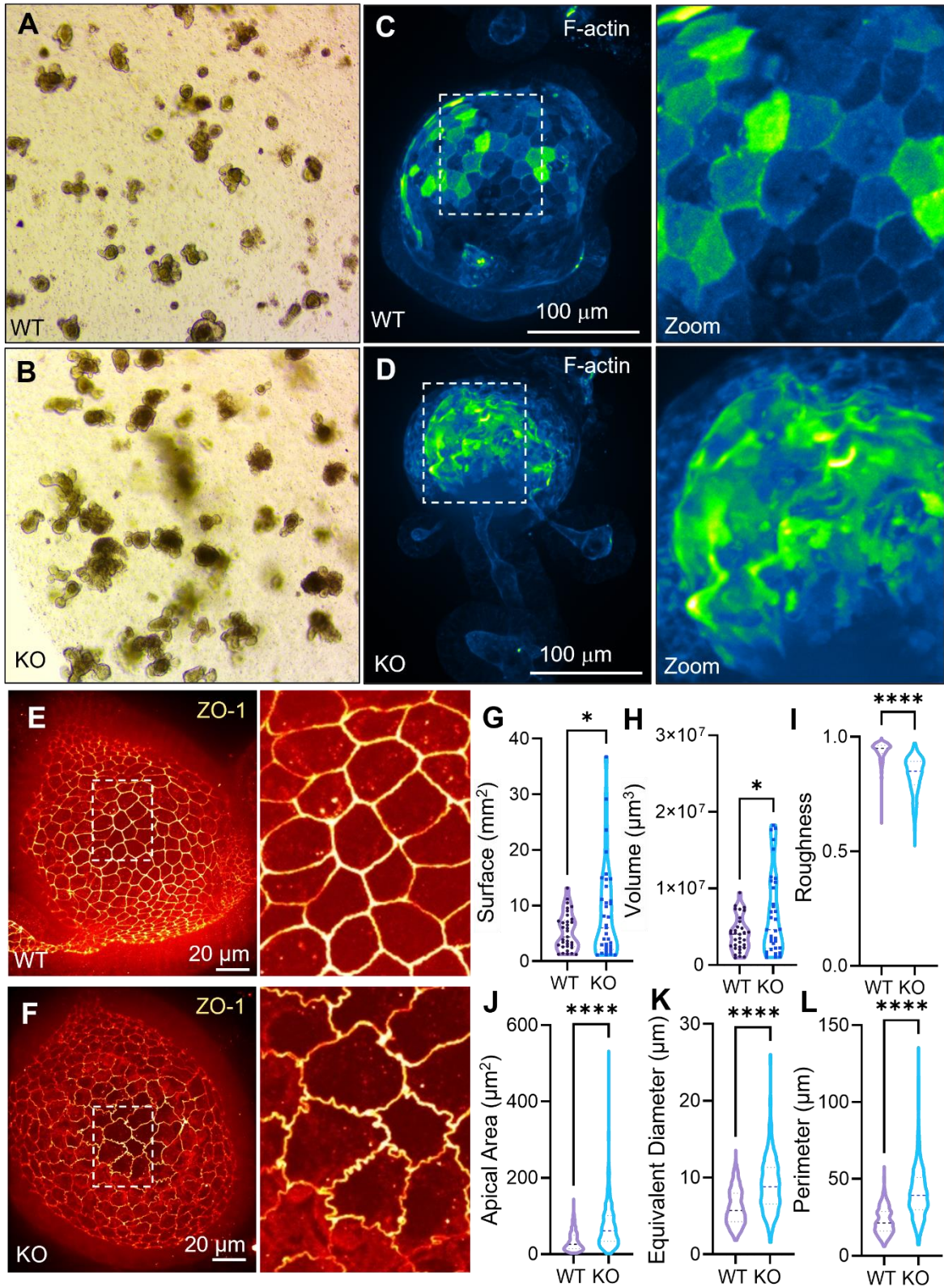


Figure 4-7: KO phenotypes are present in organoids and epithelial cell autonomous. **A**, representative image taken on a phase microscope of WT organoids in culture, taken 3 days after they were passaged. **B**, representative image taken on a phase microscope of KO organoids in culture, taken 3 days after they were passaged. **C**, still frame from live cell movie of WT organoid expressing eGFP-LifeAct. Zoom demonstrates that clear cell boundaries can be seen in the LifeAct channel. **D**, microscope of KO organoids in culture, taken 3 days after they were passaged. **E**, still frame from live cell movie of KO organoid expressing eGFP-LifeAct. No clear cell boundaries can be observed in the zoom. **F**, maximum intensity projection of WT organoid stained with ZO-1 to visualize cell junctions. Zoom demonstrates the smoothness of WT junctions. **G**, maximum intensity projection of KO organoid stained with ZO-1 to visualize cell junctions. Zoom emphasizes aberrant cell shapes. The following quantifications were obtained from three-dimensional thresholding of F-actin signal to create a 3D threshold, measurements were done automatically in Nikon Elements. **H**, quantification of the 3D surface area, **I**, quantification of organoid volume. The following quantifications were obtained from maximum intensity projections using thresholded ZO-1 signal to create a binary of the boundary of the cells, and measurements were done automatically in Nikon Elements. **J**, quantification of roughness, 1 would indicate a smooth cell. **K**, quantification of apical area. **L**, quantification of equivalent diameter. **M**, quantification of cell perimeter.. Unpaired t-test with Welch's correction used to calculate significance. * values noted in text, ****= p<.0001

To further characterize gross morphological differences between WT and KO organoids, we utilized the three-dimensional thresholding available in Nikon Elements. F-actin signal was used for thresholding. After an accurate object threshold was created, morphological measurements were obtained using the automatic measurements available within the software. Indeed, these measurements confirmed our visible observation that KO organoids tended to be larger than WT organoids of equivalent age. KO organoids displayed a significantly larger surface area than WT (Figure 4-7G, $8.71 \pm 8.49 \text{ mm}^2$ vs. $5.30 \pm 3.296 \text{ mm}^2$, $p= 0.0327$), as well as a significantly larger volume (Figure 4-7H, $6.6 \times 10^6 \pm 5.4 \times 10^6 \text{ }\mu\text{m}^3$ vs. $4.0 \times 10^6 \pm 2.2 \times 10^6 \text{ }\mu\text{m}^3$, $p= 0.0134$).

Given the lack of clear cell boundaries in the actin channel, we next investigated the junctions of WT and KO organoids. Immunofluorescence staining with an antibody

targeted against ZO-1 reveals that, similar to the native tissue, KO organoids have remarkably ruffled cell junctions (Figure 4-7F vs. WT in Figure 4-7E). Indeed, given the similarity of the phenotype, we chose to perform analysis of cell shape in the same manner as the native tissue samples (Figure 4-6). Primarily, we measured cells on the villus-like lumen region, as the extreme curvature of cells in the crypt made it difficult to threshold accurately. However, we did observe that cells in the crypt region did not visually appear different between KO and WT organoids. Here, a roughness measurement was performed using the automated measurements available in Nikon Elements: a value of 1 would indicate a smooth cell. We found that KO cells were significantly rougher than WT cells (Figure 4-7I, 0.83 ± 0.08 vs. 0.94 ± 0.03). KO cells presented with an area that was double that of WT cells (Figure 4-7J, $75.74 \pm 64.49 \mu\text{m}^2$ vs. $33.92 \pm 24.96 \mu\text{m}^2$), and KO cells had remarkably more variability in their apical area (Figure 4-7J, a range of $529.7 \mu\text{m}^2$ vs. $141.3 \mu\text{m}^2$). Additionally, a value of “Equivalent Diameter” was measured, which computes the diameter of a circle with the same area as the measured object. Indeed, KO cells had a larger equivalent diameter than those in a WT sample (Figure 4-7K, $9.12 \pm 3.66 \mu\text{m}$ vs. $6.14 \pm 2.35 \mu\text{m}$). Finally, we found that cells in KO organoids had a perimeter nearly double that of cells in WT organoids (Figure 4-7L, $41.31 \pm 17.89 \mu\text{m}$ vs. $22.70 \pm 8.51 \mu\text{m}$). Collectively, these data indicate that the morphological defects observed in vivo are epithelial cell-autonomous and occur solely due to the loss of NM2C rather than developmental or immune compensation.

Loss of NM2C induces tuft cell hyperplasia in a cell-autonomous manner.

Interestingly, in low magnification images of KO tissue, we observed bright spots of the F-actin signal (Figure 4-3, bright puncta of actin signal). Upon performing high-

resolution imaging of these samples, we found that these bright regions of signal appeared to be actin “tufts”, large microvillar-like structures with extensive actin rootlets extending into the cell body. Such actin tufts are hallmarks of tuft cells, a rare cell type that typically makes up approximately 1% of all cells in the intestinal epithelium. Tuft cells are thought to be chemosensory cells and are known to interact with the mucosal immune system to play a role in type 2 immunity. To confirm that these “tufty” cells were bonafide tuft cells, we stained WT and KO samples with an antibody targeted to doublecortin-like kinase 1 (DCLK1), a protein only expressed in tuft cells in the intestine (Figure 4-8A and 4-8B). Indeed, all cells that presented with an actin tuft were also positive for DCLK1. Using DCLK1 as a marker, we measured the number of tuft cells per villus using IMARIS. We found that KO villi had nearly 5x the number of tuft cells as WT villi (Figure 4-8C, 51 ± 16 tuft cells/villus vs. 11 ± 5 tuft cells/villus). To further investigate how the loss of NM2C might cause tuft cell hypertrophy, we stained NM2C KO organoids for DCLK1 and compared the number of tuft cells per organoid to WT organoids (Figure 4-8D and 4-8E). Interestingly, we found that tuft cell hypertrophy was present in KO organoids (Figure 4-8F, 8 ± 6 tuft cells/organoid vs. 4 ± 3 tuft cells/organoid). This result is of particular interest because tuft cell hypertrophy has classically been connected to a mucosal immune response after damage or infection. However, organoids lack an immune system, indicating that the generation of excess tuft cells is autonomous to epithelial cells lacking NM2C and not dependent on immune signaling for differentiation cues.

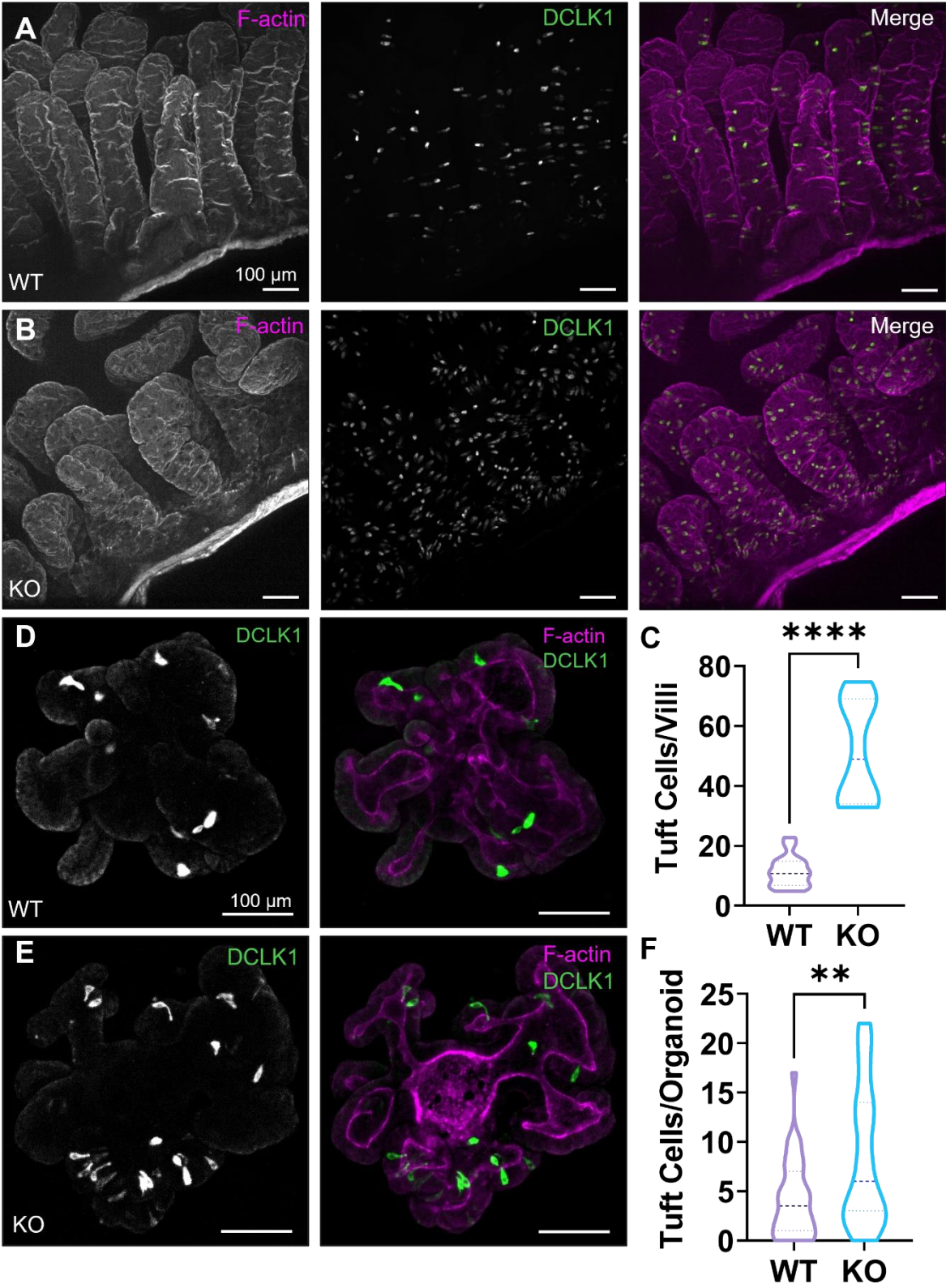


Figure 4-8: KO of NM2C results in tuft cell hyperplasia in vivo and in organoid cultures. **A**, representative 10x maximum intensity projection image of WT tissue, stained with phalloidin to visualize F-actin, and an antibody targeted to intestinal tuft cell marker DCLK1. **B**, representative 10x maximum intensity projection image of KO tissue, stained with phalloidin to visualize F-actin, and an antibody targeted to intestinal tuft cell marker DCLK1. **C**, quantification of the number of tuft cells per villus, done with IMARIS. **D**, maximum intensity projection of WT organoid stained for DCLK1 and F-actin. **E**, maximum intensity projection of KO organoid stained for DCLK1 and F-actin. **F**, quantification of the number of tuft cells per villus. Note that the violin appears cut off because some organoids had zero tuft cells. Unpaired t-test with Welch's correction was used to determine significance. **, $p=0.0013$, ****, $p<.0001$

DISCUSSION

In a previous study by our group, we reported that NM2C is the terminal web myosin 2 described in early descriptions of intestinal brush border [3, [238]. We demonstrated that NM2C works to control the length of microvilli via contractility-dependent actin turnover. In this current study, we report that NM2C KO mice demonstrate gross morphological changes and that NM2C is required to constrain cell and tissue morphology as animals age. These findings provide a new role for myosin-2 in enterocytes and indicate that an ability to propagate tension is a prerequisite for normal intestinal morphology, connecting several decades' worth of data that have demonstrated that changes in myosin light chain kinase (MLCK) are associated with various gastrointestinal disease [239].

Role of known NM2C mutations in disease

NM2C is the most understudied of the non-myosin 2 paralogs expressed in mammals. Likely, this is due to NM2C's extremely specific localization, whereas NM2A and NM2B are expressed ubiquitously. Despite the relatively little published work on NM2C, a variety of mutations with clinical manifestations have been identified. Mutations in MYH14, the gene that encodes the heavy chain of NM2C, have resulted in autosomal dominant nonsyndromic deafness-4A (DFNA4), distal hereditary motor neuropathy

(dHMN), and recto-perineal fistulas [86, [88, [89, [93, [94, [167, [169]. Notably, nearly all documented mutations in NM2C result in symptoms that present later in life or worsen with age. This is of particular interest, as we found that NM2C KO mice did not have any noticeable phenotype in neonatal stages, and morphological defects only presented in adult animals. This may explain published results from other groups that found no gross morphological defects—those previous results only contain data from animals ranging from P4-P13.5 [81, [128]. Interestingly, one group generated NM2C KO mice in a CBA/CaJ background and found that those animals only exhibited hearing loss after five months [92].

Maintenance of villus shape

It has been well-established that villi are capable of changing their morphology; this is a homeostatic response in the case of fasting and feeding periods, and also a response that can occur as a result of infection or chronic diseases, such as Crohn's and Coeliac disease [120, [121, [240]. However, there has been little discussion of the mechanism by which villi maintain their flattened cylindrical shape in homeostatic conditions. Our results here demonstrate that in the absence of NM2C, villi are capable of taking a wide variety of shapes, independent of excess inflammation that is seen in chronic gastrointestinal diseases. This indicates that in typical conditions, NM2C plays a role in constraining villus morphology and restricting the intestinal epithelium to its stereotyped shape.

Tension in the intestinal epithelium

Continuous regenerative renewal is critical for the health of the intestinal tract. Thus, migration of the epithelial sheet is key to maintain homeostasis. It has been previously demonstrated that apical myosin 2 present in cell-cell junctions is under tension along

the villus length [131]. Here, we identify that a force producing cytoskeletal element, NM2C plays an important role in constraining intestinal morphology and ultrastructure. We found that lack of NM2C results in a larger apical area and ruffled ZO-1 signal. Taken together, this indicates that less tension is present at the cell-cell contacts. Previous studies have found that ruffled ZO-1 signal can occur in cases of both increased and decreased tension [241, [242]. However, expansion of the apical area is typically associated with a lack of myosin activity; thus, we believe that there is less tension present in the epithelium of NM2C KO animals. This is of particular interest, as it has been well established that tension across cell-cell contacts plays an essential role in regulating barrier function [210, [223, [239]. Additionally, in order for an epithelial sheet to migrate, cell-cell contacts must be well-maintained while withstanding the forces required for migration. Cell-cell contacts play a key role in regulating the structural integrity of a tissue. This is true in both homeostasis and instances of inflammation or infection where tissue remodeling is required [227]. Indeed, it has been demonstrated that apical cell-cell junctions transmit contractile actomyosin force [243]. Particularly, cell-cell junctions retain a linear appearance as migration occurs. In drosophila embryos, upon stress to the junctions, myosin will relocate from a medial array to junctional sites in order to protect junctions from rupture, and this myosin-generated tension is thought to ensure the linearity of junctions during migration [8]. In addition to migration, intestinal cells are subject to a variety of exogenous mechanical forces [244]. For decades, researchers have been encouraged to investigate further the role of exogenous and endogenous forces within the intestinal epithelium, but relatively little work has been done in this area.

A variety of open questions on the role of non-muscle myosins in the gastrointestinal tract remain. Indeed, understanding why the compensation by NM2A, which relocates to the terminal web in NM2C KO animals, is not sufficient for constraining cell and tissue morphology would be key to understanding what kind of force needs to be applied to the intestinal epithelium. In addition, further investigation into the precise organization of the NM2C minifilaments present at the level of the terminal web would allow for a more precise understanding of how force propagates across the apical surface. Given the various changes in villus morphology observed in chronic illnesses affecting the upper GI tract, it would be of potential interest to localize NM2C in various patient populations to understand if this motor is up or downregulated in disease. Potentially, understanding of NM2C in disease could lead to new therapeutic targets and a better overall understanding of disease progression.

CHAPTER 5

FUTURE DIRECTIONS

Role of cofilin in regulating BB length

ADF/Cofilin is a ubiquitous actin regulatory protein that is widely implicated for its severing activity [17, [245]. With a known affinity for actin in the ADP-bound state, cofilin binds to structural weaknesses in the actin filament and facilitates severing at the pointed end, which promotes pointed end depolymerization [4] (Figure 5-1). Cofilin severing events also lead to new barbed ends being exposed, which can result in rapid increases in local actin assembly (Figure 5-1). A cycle of phosphorylation and dephosphorylation is responsible for regulating the activity of cofilin; however, the relative activity of regulatory factors that cap barbed ends or acceleration filament disassembly is equally important in determining if cofilin activation results in net increases or decreases of local actin filament density. It has also been demonstrated that cofilin activity can be biomechanically regulated, in particular, that increasing actin filament strain tends to promote cofilin activity [207]. Torsional stress on actin filament networks has also been implicated in increased cofilin activity.

The term “contractility-dependent actin turnover” was first coined following a study in neuronal growth cones, which demonstrated that the turnover of actin at the leading edge was dependent on M2 activity [201]. This study also found that M2 contractile activity produces actin bundle strain. Given the potential for actin filament strain to increase cofilin severing, this group followed up on their initial study by investigating the role of cofilin activity and how it relates to NM2C activation in neurite

growth [205]. This study found that M2 contractility serves as a catalyst for cofilin activity, which results in increased actin network turnover. Indeed, inhibition of M2 resulted in decreased cofilin dynamics. From this study, the authors proposed four distinct mechanisms by which M2 activity could affect cofilin activity. (1) myosin contractility could strain filaments and bundles, which would promote filament severing by localizing elastic energy at boundaries between bare and cofilin-decorated segments. (2) myosin-binding could displace cofilin from decorated filament segments, which would create decorated/undecorated boundaries, which are favorable sites for severing. (3) cofilin could mechanically destabilize filaments by inducing buckling. (4) M2 tethering alone could enhance severing [205].

Figure 5-1: Cofilin influences actin dynamics in a variety of ways. Cartoon schematic demonstrating the roles of cofilin. Adapted from Ohashi 2015 [4].

Our previous results, shown in Chapter III, indicate that NM2 contractile activity controls the length of microvilli, particularly our result that inhibition of NM2 results in elongated microvilli parallels those results seen in the growth cone, where NM2 inhibition results in elongated actin bundles. Given the results in growth cones that demonstrate the mechanical activity of NM2 can enhance cofilin-dependent actin bundle turnover, investigating the

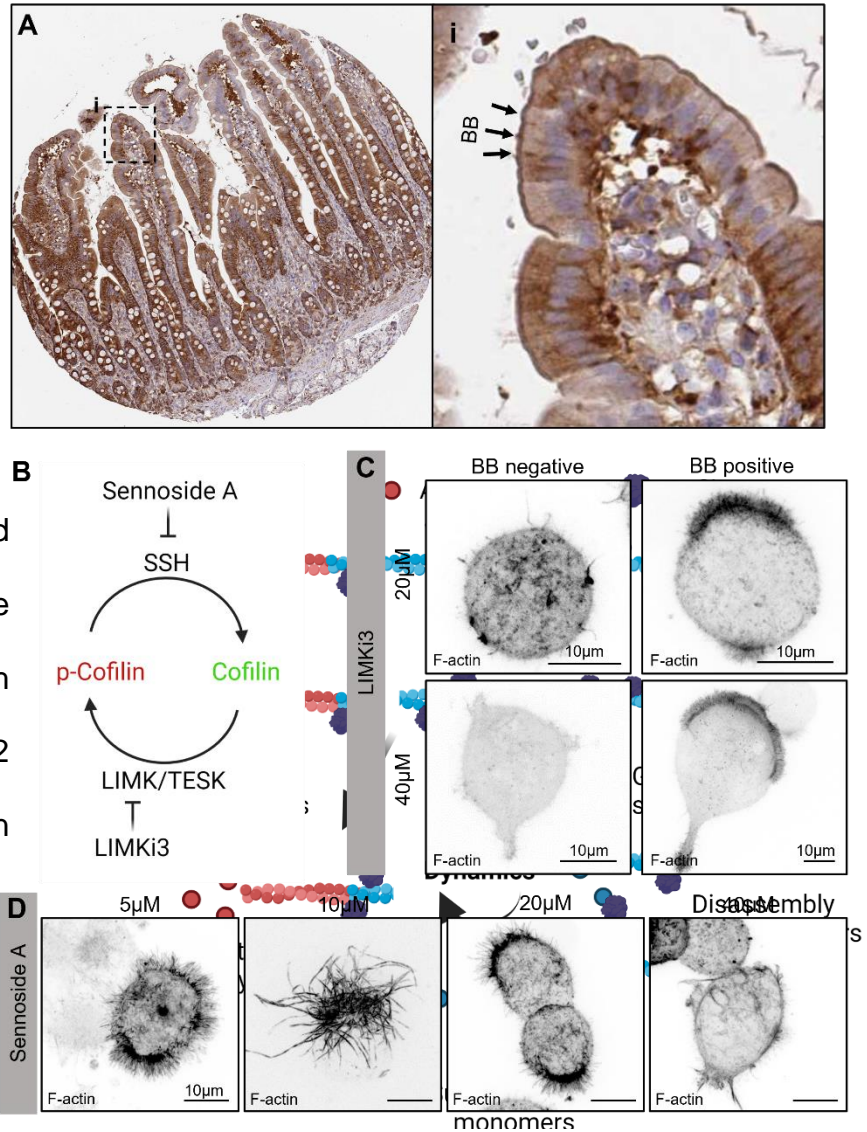


Figure 5-2: Potential role of cofilin in the brush border. **A**, data from the Human Protein Atlas showing Cofilin 1 localization in the small intestine. **i.** zoom of **A**, arrows point to brush border signal. **B**, schematic of cofilin, its regulatory proteins, and known inhibitors. Red indicates the inactive state and green the active state. **C**, representative maximum intensity projection images of the effects of various concentration of LIMKi 3 treatment on W4 cells. **D**, representative maximum intensity projection images of the effects of various concentration of sennoside A treatment on W4 cells.

potential role of cofilin in the brush border would provide further insight into how NM2 regulates brush border length. Data from the Human Protein Atlas shows the cofilin is

expressed in the small intestine [74, [75] (Figure 5-2A). While cofilin expression is rather ubiquitous through the cell, there is a noticeable intensity in signal intensity in the BB (Figure 5-2Ai). Thus, we chose to investigate pharmacological perturbations of cofilin in W4 cells, similar to those experiments done in Chapter III. Cofilin is phosphorylated on Ser3 and is considered inactive in its phosphorylated state and active in its dephosphorylated state [4] (Figure 5-1B). The slingshot (SSH) family of proteins catalyzes the removal of the phosphate group from Ser3, while LIM-kinases (LIMKs) and testicular protein kinases (TESKs) are responsible for the phosphorylation of cofilin (Figure 5-2B) [246]. Sennoside A, a compound derived from rhubarb, was recently found to increase cofilin phosphorylation in vitro and in vivo by inhibiting SSH (Figure 5-2B) [247]. Similarly, LIMKi 3 has been described as an inhibitor of LIMK1/2 (Figure 5-2B) [248]. It is important to note that LIMKs are implicated in the regulation of a variety of cytoskeletal elements, including actin polymerization mediated by the Rho family of proteins [249].

Here, we treated doxycycline-induced W4 cells with either LIMKi 3 or Sennoside A for 24hrs, as previous studies done with these compounds all used relatively long-time scales (12-44hrs). In order to determine if there was any noticeable effect on the brush border, we experimented with a variety of compound concentrations and imaged fixed cells at each concentration. In the LIMKi 3 condition, we used 20 μ M and 40 μ M. Interestingly, in these preliminary experiments, we observed the presence of BB positive and BB negative cells (Figure 5-1C). At 40 μ M, BB negative cells had a very dim F-actin signal, as determined by phalloidin staining (Figure 5-1C). Interestingly, the cells treated with 40 μ M LIMKi 3 that remained BB positive were also substantially

larger than usual W4 cells. These preliminary results seem to suggest that increased cofilin activity might result in fewer cells presenting with a BB (hence the BB negative populations) and increased cell size due to positive intracellular pressure combined with a lacking actin cytoskeleton, as in the case of the BB positive cells.

Interestingly, the sennoside A treated cells presented with a variety of phenotypes dependent on the compound concentration. At 10 μM , cells displayed markedly elongated microvilli, similar to those seen in blebbistatin treated cells in Figure 3-6 (Figure 5-1D). Cells treated with 5 μM or 20 μM did not appear to have microvilli that are elongated to the same extent as the 10 μM treatment condition (Figure 5-1D). Interestingly, cells treated with 40 μM of sennoside A appeared to lose their brush borders completely (Figure 5-1D). It has been proposed that high concentrations of activated cofilin promote the nucleation of new actin filaments—perhaps, in the absence of activated cofilin that would occur at high sennoside A concentration, a critical mechanism of BB maintenance is disrupted.

However, it is important to emphasize that these interpretations are **preliminary results**, and as such, do not have any sort of statistical power needed to be more concrete conclusions. The role of cofilin is likely multifaceted and carefully regulated within BB expressing cell types. Indeed, the appearance of potential phenotypes indicates that further experimentation is necessary and that understanding the role of cofilin in the BB represents an important future direction to be explored.

Loss of NM2C may impact cell migration

During our investigation of the NM2C KO mouse, we wanted to investigate if the rate of cell migration was altered in these animals due to the changes in villus

morphology and the compressed lateral cell profiles. Recently, crypt-villus migration has been described using a model of collective cell migration that is driven by basolateral Arp2/3 actin protrusions oriented in the direction of migration, which resemble feet that are in contact with the basement membrane [217]. These new findings were in contrast to a decades' old assumption that crypt-villus migration was driven solely by mitotic pressure from dividing cells in the crypts. In this study, the authors used a 5-ethynyl-2'-

deoxyuridine (EdU) pulse-chase assay. EdU is injected into mice intraperitoneally (IP) and labels newly synthesized DNA, after which you apply a “click” chemistry reaction to detect the new thymidine analog [250]. For our investigation of cell migration in NM2C KO mice, we collaborated with the Williams lab at Vanderbilt to perform a 5-bromo-2'-deoxyuridine (BrdU) pulse-chase assay. Similar to EdU, BrdU is introduced using an IP injection. BrdU is incorporated in de novo-synthesized DNA as a substitute for thymine

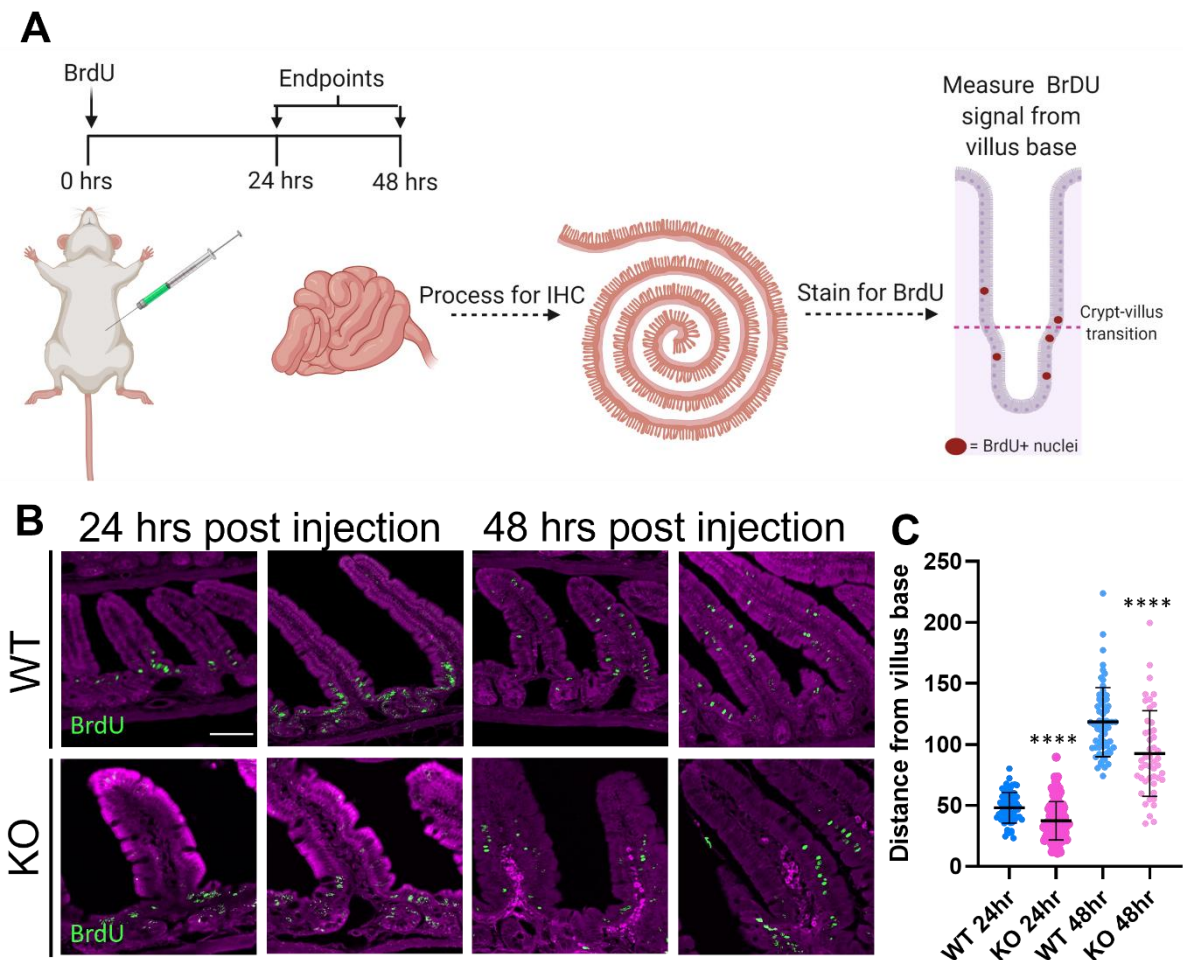


Figure 5-3: Preliminary data suggests cell migration is impaired with loss of NM2C. **A**, cartoon schematic of BrdU experimental timeline. **B**, representative images of WT and KO tissue from animals sacrificed 24hrs and 48hrs after BrdU injection. BrdU positive cells labeled in green, purple is background fluorescence. Scale bar is 50µm and applies to all images. **C**, quantification of the distance the leading BrdU positive cell is from villus base. Student's t-test used for significance, **** indicateds $p > .0001$

and thus permanently labels actively proliferating and daughter cells until it is diluted out after many rounds of cell division [250]. The BrdU signal is then detected using anti-BrdU antibodies. However, detection of the BrdU that has been inserted into the genomic DNA required harsh digesting or denaturing treatment of the tissue (trypsin, HCl, heat, and or DNase are commonly used). This, unfortunately, often results in tissue damage or incompatibility for staining with other antibodies.

For this set of experiments, we injected WT and KO mice with BrdU and sacrificed the animals at either 24 or 48hrs (Figure 5-3A). The entire length of the gut was rolled into a swiss roll and then processed for paraffin embedding and immunohistochemistry (Figure 5-3A). For a preliminary assessment of collective cell migration in KO animals, 2 animals from each group were sacrificed at 24hrs, and 1 animal from each group was sacrificed at 48hrs. BrdU or EdU experiments typically require large cohorts in order to have enough statistical power for obtaining significant results. In these preliminary studies, we stained for BrdU and used an anti-mouse 568 secondary to non-specifically label the villi (Figure 5-3B). Indeed, we found that in both the animals sacrificed at 24hrs and those sacrificed at 48hrs, the KO animals presented with BrdU positive cells closer to the crypt-villus transition zone (Figure 5-3C). This suggests that NM2C KO animals have some impairment in cell migration, and further investigation is warranted. There are a few features of the KO animals that obscure the typical BrdU measurement of labeled cells. The KO animals have significantly larger villi, which respectively results in KO animals having few villi per mm of intestine (Figure 4-1). Additionally, KO villi have a morphology that is markedly different from that of WT animals. These changes in the gross morphology of the KO intestine make measuring

the distance a cell is from the crypt-villus transition a potentially questionable readout. It may be more accurate to normalize the distance from crypt-villus transition to villus length. Indeed, the ideal experiment would be to observe collective cell migration in vivo using multiphoton microscopy and endogenously tagged fluorescent animals. However, developing the animal models and assay for such an experiment was out of the scope of this thesis.

Assessing the role of myosin-2 inhibition/activation in vivo

A variety of epithelial cell culture models display a brush border on their apical surface. The majority of these are derived from either kidney or colonic epithelial cells, with cancerous origins. While these cell culture models are incredibly useful for performing structure-function analysis and gaining insight into the role of a protein such as NM2C in an organ such as the intestine, which undergoes continuous regenerative renewal, important nuances may exist in vivo that cannot be recapitulated in culture. Previously, our lab has developed an assay for assessing the effects of cytoskeleton targeting pharmacologic compounds on the brush border in vivo [251]. In this assay, mice are put under anesthesia, and a small incision is made in the abdomen (Figure 5-4A). A loop of the intestine is then gently pulled out through the incision, and the jejunum is located (Figure 5-4A). The jejunum must be pulled away from the animal; in doing so, portions of the blood vessels that supply the small intestine might need to be severed and cauterized. Two small incisions, just large enough for a pipet tip, are cut in the jejunum, about two inches away from each other (Figure 5-4A). The compound of interest is then perfused through the section of intestine every 10 minutes for 4 hours (Figure 5-4A). In the following experiment, the compound of interest was manually

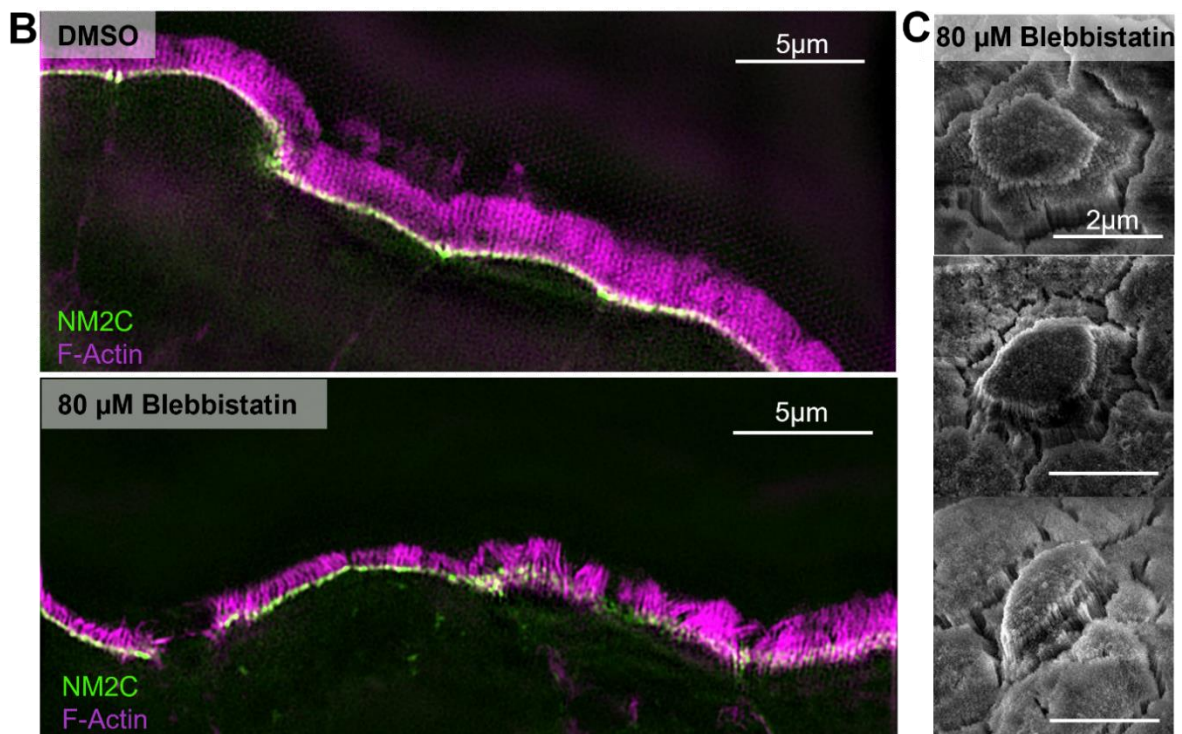
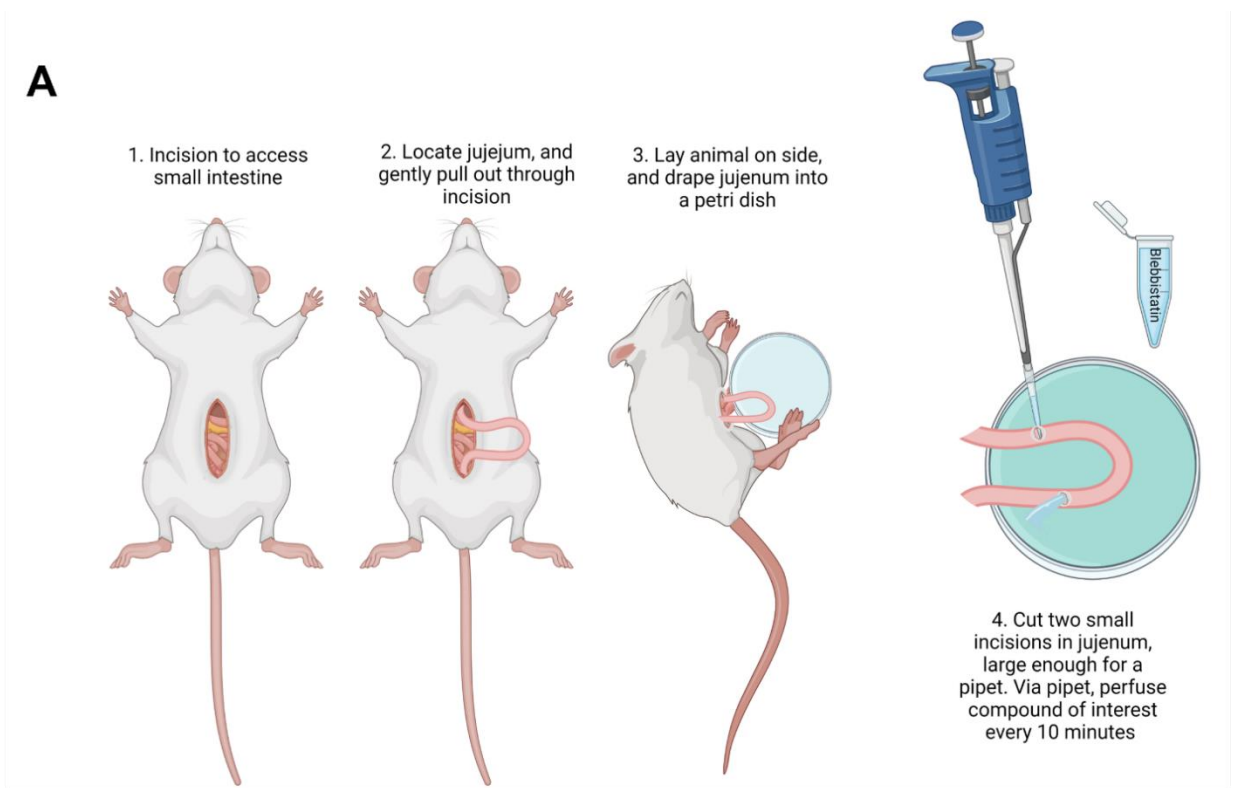


Figure 5-4: In vivo perfusion of Blebbistatin. **A**, experimental setup for in vivo drug perfusion. **B**, Super-resolution maximum intensity projections of DMSO treated control and blebbistatin treated sample. **C**, Representative SEM images of tuft-like cell structures found in blebbistatin treated tissue.

perfused using a p200 pipet; however, this could be adapted to use a perfusion machine. After 4 hours, the animals were sacrificed, and the tissue that was exposed to the drug was harvested and processed for frozen sections and electron microscopy.

Here, we perfused 80 μ M of blebbistatin through the intestine of one animal and perfused an identical volume of DMSO through the intestine of another animal as the vehicle control. Interestingly, in frozen sections, intestine that has been treated with blebbistatin presented with a very heterogenous brush border, where microvilli varied in length within a single image field, as opposed to the DMSO control, where the brush border appeared to be approximately the same length, as would be expected (Figure 5-4B). Interestingly, we observed a similar phenotype in TEMs of NM2C KO brush border—some sections would have very short “nubby” microvilli, whereas other sections would have longer microvilli. Also of interest, in SEM of animals treated with the in vivo Blebbistatin assay, villi had frequent “tufts” of microvilli, which appeared to be the area of approximately one cell, with microvilli that were substantially longer than the surrounding cells (Figure 5-4C). Only one such tuft was observed in DMSO control samples. It is unclear if these “tufty” cells simply have elongated microvilli or if they are true tuft cells. If they were true tuft cells, this would be an extremely interesting finding, as these animals were only treated with drug for 4hrs, which is not a long enough time scale for new tuft cells to differentiate in the crypts and migrate out to the villus where they can easily be visualized with SEM. This would open the possibility of enterocytes or another intestine epithelial cell transdifferentiating into a tuft cell-like state, which in itself would be a fascinating finding. This would also indicate that there is some inherent function of myosin and its force-producing abilities that play a role in controlling cell fate

within the small intestine. This in vivo perfusion experiment would need to be repeated a handful of times to make any concrete conclusions but provides a relatively simple way to disturb myosin dynamics in vivo and visualize the effects on the brush border and intestinal morphology.

Role of NM2C in tuft cells

Interestingly, we found that the NM2C KO mouse displayed tuft cell hyperplasia. While this could be due to a lack of junctional integrity causing an upregulation in immune response, we also observed tuft cell hyperplasia in organoids generated from NM2C KO mice. This organoid phenotype would indicate that the tuft cell hyperplasia is occurring independent of the broader mucosal immune system and is instead epithelial cell-autonomous and directly related to the loss of NM2C. After observing this tuft cell hyperplasia in KO animals, we went back into the NM2C-GFP mouse model to investigate the native expression of NM2C in tuft cells. Due to their rarity within the intestinal epithelium, little is understood about how specific protein expression in tuft cells compares to enterocytes or other intestinal epithelial cells. In particular, there is currently no published work investigating if tuft cells have a terminal web. Tuft cells are known for their extended actin rootlets, which would almost certainly leave little physical space for the complex meshwork that is the terminal web of enterocytes.

Here, we use the tuft cell marker DCLK1 to mark tuft cells in NM2C-GFP small intestine (Figure 5-5A). The tuft cells were confirmed to have an actin tuft and extended rootlet using phalloidin to mark F-actin. Interestingly, in tuft cells, there is essentially no NM2C in the medial portion of the cell and only a very faint band of NM2C signal at the actomyosin junctional belt (Figure 5-5B). It might be that another NM2C paralog, such as

NM2A or NM2B, is the dominant paralog in the tuft cell junction belt. However, it certainly does appear that tuft cells do not have an M2-rich terminal web.

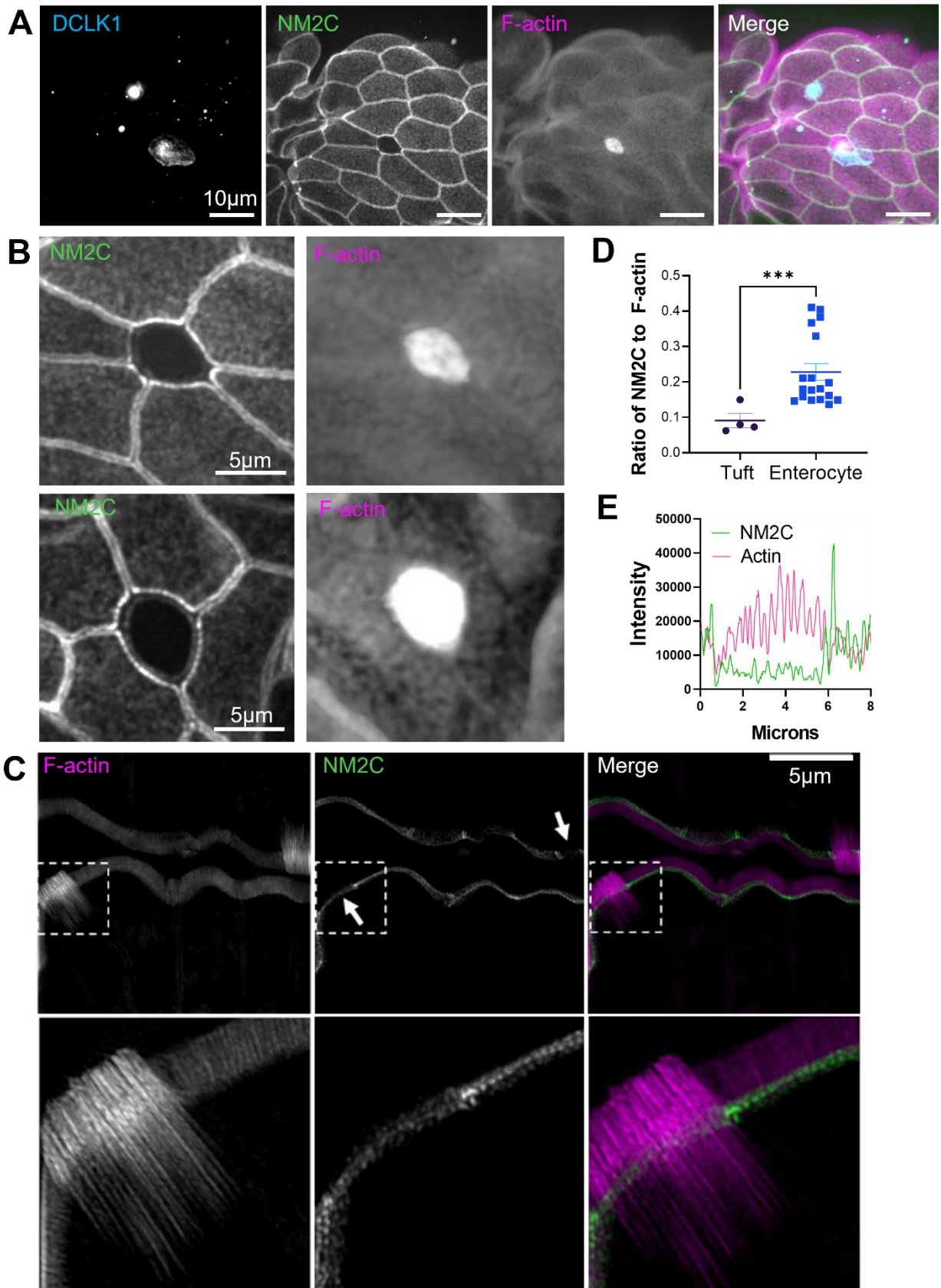


Figure 5-5: Tuft cells lack medial NM2C expression. **A**, in mount whole tissue from endogenous NM2C-GFP tagged mice, DCLK1 clearly marks cells with a bright, F-actin tuft. **B**, two examples of NM2C signal in tuft cells, maximum intensity projection images taken with spinning disk confocal. **C**, Super-resolution maximum intensity projection images of two tuft cells, indicated with white arrows. Within the highlighted tuft cells, there is a obvious lack of NM2C intensity. **D**, Tuft cells have a lower NM2C to F-actin ratio. **E**, Line scan from single plane of the image shown in **C**, demonstrating that NM2C decreases to levels below that of enterocytes as F-actin signal increases within a tuft cell.

Investigating molecular organization of NM2C in the terminal web

One of the persistent unanswered questions from the study detail in Chapter III is the molecular organization of NM2C in the terminal web. NM2C paralogs are known for forming ordered arrays of myosin “stacks” in other models, including migrating cells and cardiomyocytes. These ordered myosin arrays tell us important information about force distribution within a cell. However, in the case of the medial array of terminal web NM2C, there was no immediately obvious ordered structure, although it was possible to find regions that appeared somewhat ordered.

There are several strategies that could be used to investigate the molecular

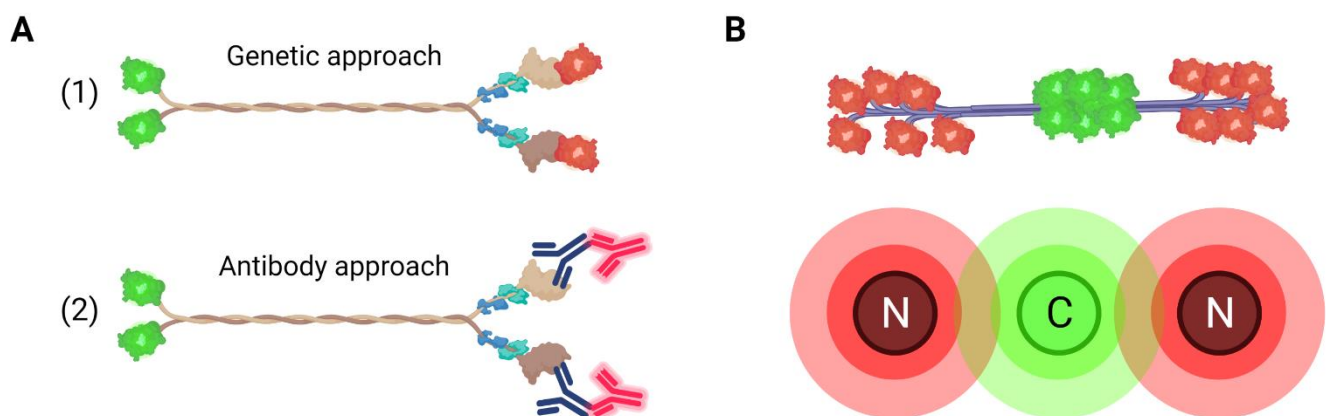


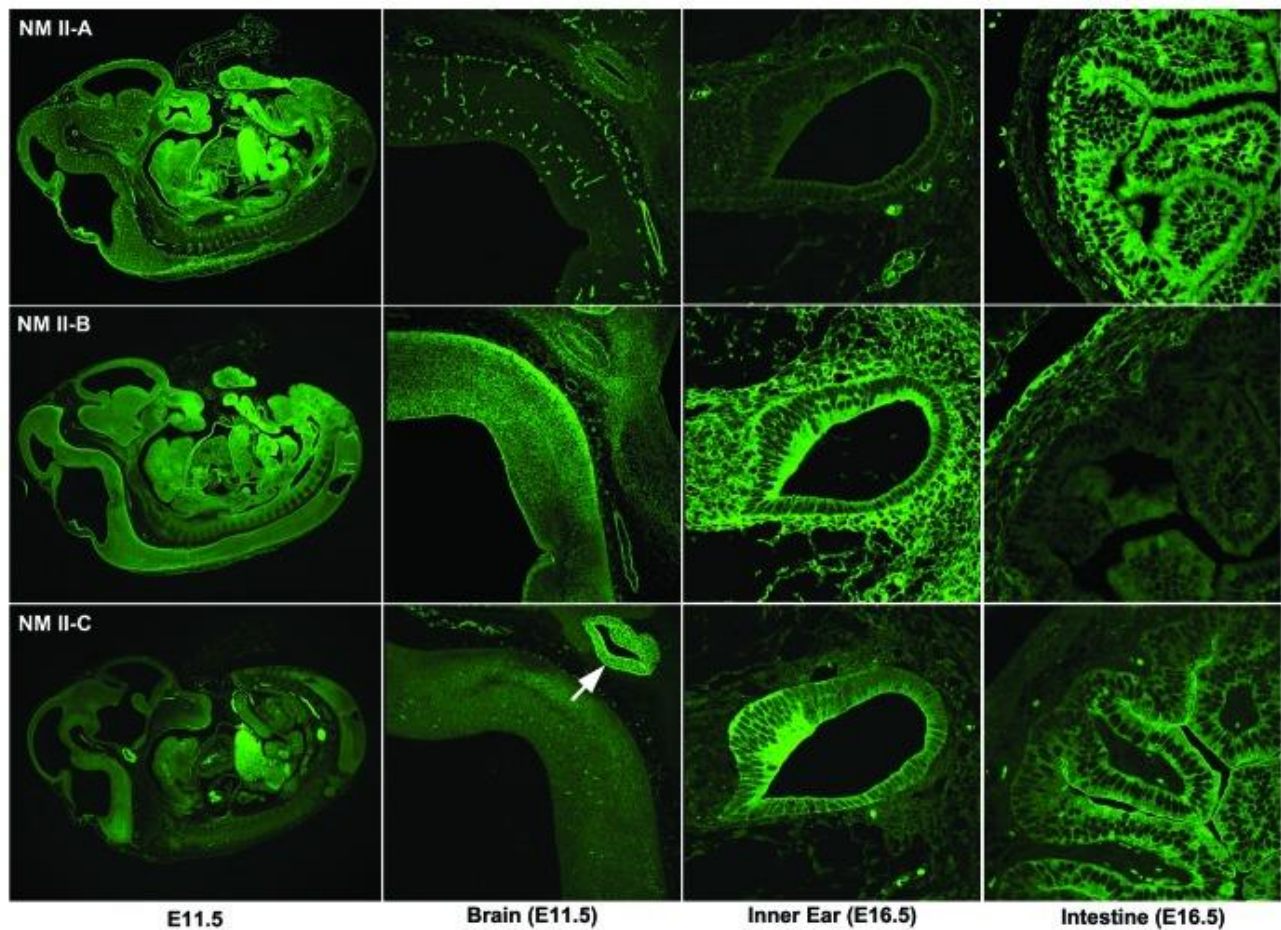
Figure 5-6: Determining orientation of NM2C filaments in the terminal web. **A**, diagram of strategies for labels both ends of NM2C. **B**, cartoon of the appearance of a dual-labeled minifilament (top), and how the signal would appear under the microscope (bottom).

organization of terminal web NM2C, as diagramed in Figure 5-6A. (1) an NM2C construct for transfection with a GFP on the N-terminus and a HaloTag/mCherry on the C-terminus (or vice versa). This construct would allow for understanding the orientation of NM2C minifilaments within cultured cells. However, cultured cells are not subject to the same levels of curvature that exist in the native small intestine, so the force distribution in cultured cells may not be equivalent to what it is in vivo. (2) label the N-terminus of NM2C minifilaments within native NM2C-GFP tissue with an N-terminally targeted NM2C antibody, an RLC antibody, or similar antibody that could accurately label the motor head of terminal web NM2C. Unlike the NM2A-GFP mouse and the NM2B-GFP mouse, which both have the fluorescent probe inserted onto the N-terminal end of the respective myosin heavy chain, the NM2C-GFP mouse has the fluorescent probe on the C-terminal end, such that it labels the middle of the NM2C minifilaments. Given that these animals were all generated by the Adelstein group at the NIH, it is unclear what is the reason for the C-terminal tag in the NM2C animals. This does present a technical challenge since most myosin antibodies are targeted towards sequences in the C-terminus, so a light chain targeted antibody may be more suitable. If successful, minifilaments should be dual-labeled, with the middle of the filament fluorescing in one color, and the ends fluorescing in another color (Figure 5-6B)

Role of NM2C in other organ systems

One of the unique characteristics of NM2C is that it has very tissue-specific expression, unlike the other two NM2 paralogs, which are expressed in almost every cell type, although the ratio varies (Figure 5-7). Interestingly, during the start of this dissertation work, we transfected LLC-PKL1-CL4 (CL4), a porcine kidney cell line commonly used in the lab to investigate BB development and dynamics, with NM2C. In

this cell line, NM2C was rarely localized to the apical surface and instead was found decorating the actin stress fibers at the bottom of the cell. However, NM2A would readily localize to the apical surface of CL4 cells. While it is unclear if the kidney has a terminal web that is as intricate as that of the small intestine, there does seem to be a specific role for NM2C that does not depend on if a cell type has a brush border. Indeed, these observations are supported by published work that specified that NM2A



localized to the apical membrane, while NM2C could be found at both the apical and basolateral surfaces.

The other two regions that are known to have high NM2C expression are the cochlea, where NM2C has been implicated in convergent extension, and the pituitary gland and glial cells of the brain (Figure 5-7) [6]. Certain neuropathies have been associated with a mutation in NM2C, suggesting that WT NM2C has a specific role within the brain [91, [94, [252, [253]. Exploring the roles of NM2C in other organs will allow for greater insight as to why NM2C has such specific expression and if it plays any unique roles that cannot be compensated for by NM2A or NM2B

Conclusions

These data and hypotheses within this dissertation represent a continuation of nearly two centuries of research on myosin, which began in 1868 with Wilhelm Kühne, with NM2C being the most recently discovered myosin motor. The work here answers a decades' old question about the identity and role of an early identified BB myosin-2. Here, we have established that NM2C is localized to the terminal web of intestinal enterocytes, where it works to control the length of apical microvilli via contractility-dependent actin turnover (Chapter III). Additionally, we found that NM2C plays a unique role in constraining villus and cell morphology as organisms age and that this

Figure 5-7: NM2C displays tissue specific localization. From Ma and Adelstein 2014, Bioarchitecture [6]. Whole mount images of mice embryos demonstrating localization of NM2A, NM2B and NM2C.

cannot be effectively compensated by the redistribution of NM2A to the terminal web (Chapter IV). We also found that NM2C KO mice display an exceptional amount of tuft

cell hyperplasia (Chapter IV), which is of particular interest as tuft cells appear to natively express less NM2C. The future directions and experiments detailed in this chapter will be critical to gaining further understanding of the biological function of NM2C and understand the role of propagating force across a complex epithelial sheet, such as the small intestine.

REFERENCES

1. Billington, N., et al., *Characterization of three full-length human nonmuscle myosin II paralogs*. J Biol Chem, 2013. **288**(46): p. 33398-410.
2. Crawley, S.W., M.S. Mooseker, and M.J. Tyska, *Shaping the intestinal brush border*. J Cell Biol, 2014. **207**(4): p. 441-51.
3. Hirokawa, N., et al., *Organization of actin, myosin, and intermediate filaments in the brush border of intestinal epithelial cells*. Journal of Cell Biology, 1982. **94**: p. 425-443.
4. Ohashi, K., *Roles of cofilin in development and its mechanisms of regulation*. Development, Growth & Differentiation, 2015. **57**(4): p. 275-290.
5. Kodera, N. and T. Ando, *The path to visualization of walking myosin V by high-speed atomic force microscopy*. Biophysical Reviews, 2014. **6**(3): p. 237-260.
6. Ma, X. and R.S. Adelstein, *The role of vertebrate nonmuscle Myosin II in development and human disease*. Bioarchitecture, 2014. **4**(3): p. 88-102.
7. Fletcher, D.A. and R.D. Mullins, *Cell mechanics and the cytoskeleton*. Nature, 2010. **463**(7280): p. 485-492.
8. Sumi, A., et al., *Adherens Junction Length during Tissue Contraction Is Controlled by the Mechanosensitive Activity of Actomyosin and Junctional Recycling*. Dev Cell, 2018. **47**(4): p. 453-463.e3.
9. Alberts, B., et al., *Molecular Biology of the Cell*. 2015: W.W Norton & Company.
10. Huxley, H.E., *ELECTRON MICROSCOPE STUDIES ON THE STRUCTURE OF NATURAL AND SYNTHETIC PROTEIN FILAMENTS FROM STRIATED MUSCLE*. J Mol Biol, 1963. **7**: p. 281-308.
11. Neuhaus, J.M., et al., *Treadmilling of actin*. J Muscle Res Cell Motil, 1983. **4**(5): p. 507-27.
12. Pollard, T.D., *Rate constants for the reactions of ATP- and ADP-actin with the ends of actin filaments*. J Cell Biol, 1986. **103**(6 Pt 2): p. 2747-54.
13. Pollard, T.D. and J.A. Cooper, *Actin, a central player in cell shape and movement*. Science, 2009. **326**(5957): p. 1208-12.
14. Pollard, T.D., *Polymerization of ADP-actin*. Journal of Cell Biology, 1984. **99**(3): p. 769-777.
15. Lee, S.H. and R. Dominguez, *Regulation of actin cytoskeleton dynamics in cells*. Mol Cells, 2010. **29**(4): p. 311-25.
16. Firat-Karalar, E.N. and M.D. Welch, *New mechanisms and functions of actin nucleation*. Curr Opin Cell Biol, 2011. **23**(1): p. 4-13.
17. Bernstein, B.W. and J.R. Bamburg, *ADF/cofilin: a functional node in cell biology*. Trends Cell Biol, 2010. **20**(4): p. 187-95.
18. Pena, J.F., et al., *Conserved expression of vertebrate microvillar gene homologs in choanocytes of freshwater sponges*. Evodevo, 2016. **7**: p. 13.
19. Karpov, S.A. and B.S.C. Leadbeater, *Cytoskeleton Structure and Composition in Choanoflagellates*. Journal of Eukaryotic Microbiology, 1998. **45**(3): p. 361-367.
20. Svitkina, T., *The Actin Cytoskeleton and Actin-Based Motility*. Cold Spring Harb Perspect Biol, 2018. **10**(1).
21. Kerber, M.L. and R.E. Cheney, *Myosin-X: a MyTH-FERM myosin at the tips of filopodia*. J Cell Sci, 2011. **124**(Pt 22): p. 3733-41.

22. Petersen, K.J., et al., *MyTH4-FERM myosins have an ancient and conserved role in filopod formation*. Proc Natl Acad Sci U S A, 2016. **113**(50): p. E8059-e8068.
23. Yang, C. and T. Svitkina, *Filopodia initiation: focus on the Arp2/3 complex and formins*. Cell Adh Migr, 2011. **5**(5): p. 402-8.
24. Coudrier, E., D. Kerjaschki, and D. Louvard, *Cytoskeleton organization and submembranous interactions in intestinal and renal brush borders*. Kidney Int, 1988. **34**(3): p. 309-20.
25. Mooseker, M.S., *Organization, chemistry, and assembly of the cytoskeletal apparatus of the intestinal brush border*. Annu Rev Cell Biol, 1985. **1**: p. 209-41.
26. Bartles, J.R., et al., *Small espin: a third actin-bundling protein and potential forked protein ortholog in brush border microvilli*. J Cell Biol, 1998. **143**(1): p. 107-19.
27. Bretscher, A. and K. Weber, *Villin: the major microfilament-associated protein of the intestinal microvillus*. Proc Natl Acad Sci U S A, 1979. **76**(5): p. 2321-5.
28. Bretscher, A. and K. Weber, *Fimbrin, a new microfilament-associated protein present in microvilli and other cell surface structures*. J Cell Biol, 1980. **86**(1): p. 335-40.
29. Tyska, M.J., et al., *Myosin-1a is critical for normal brush border structure and composition*. Mol Biol Cell, 2005. **16**(5): p. 2443-57.
30. Ameen, N. and G. Apodaca, *Defective CFTR apical endocytosis and enterocyte brush border in myosin VI-deficient mice*. Traffic, 2007. **8**(8): p. 998-1006.
31. Hegan, P.S., et al., *Myosin VI is required for maintenance of brush border structure, composition, and membrane trafficking functions in the intestinal epithelial cell*. Cytoskeleton (Hoboken), 2012. **69**(4): p. 235-51.
32. Chen, J., J.A. Cohn, and L.J. Mandel, *Dephosphorylation of ezrin as an early event in renal microvillar breakdown and anoxic injury*. Proc Natl Acad Sci U S A, 1995. **92**(16): p. 7495-9.
33. Saotome, I., M. Curto, and A.I. McClatchey, *Ezrin is essential for epithelial organization and villus morphogenesis in the developing intestine*. Dev Cell, 2004. **6**(6): p. 855-64.
34. Mooseker, M.S. and L.G. Tilney, *Organization of an actin filament-membrane complex. Filament polarity and membrane attachment in the microvilli of intestinal epithelial cells*. J Cell Biol, 1975. **67**(3): p. 725-43.
35. Tilney, L.G. and R.R. Cardell, *Factors controlling the reassembly of the microvillous border of the small intestine of the salamander*. J Cell Biol, 1970. **47**(2): p. 408-22.
36. Postema, M.M., et al., *IRTKS (BAIAP2L1) Elongates Epithelial Microvilli Using EPS8-Dependent and Independent Mechanisms*. Curr Biol, 2018. **28**(18): p. 2876-2888 e4.
37. Crawley, S.W., et al., *ANKS4B Is Essential for Intermicrovillar Adhesion Complex Formation*. Dev Cell, 2016. **36**(2): p. 190-200.
38. Weck, M.L., et al., *Myosin-7b Promotes Distal Tip Localization of the Intermicrovillar Adhesion Complex*. Curr Biol, 2016. **26**(20): p. 2717-2728.
39. Crawley, S.W., et al., *Intestinal brush border assembly driven by protocadherin-based intermicrovillar adhesion*. Cell, 2014. **157**(2): p. 433-446.

40. Hirokawa, N. and J.E. Heuser, *Quick-freeze, deep-etch visualization of the cytoskeleton beneath surface differentiations of intestinal epithelial cells*. J Cell Biol, 1981. **91**(2 Pt 1): p. 399-409.
41. Hull, B.E. and L.A. Staehelin, *The terminal web. A reevaluation of its structure and function*. J Cell Biol, 1979. **81**(1): p. 67-82.
42. Leblond, C.P., H. Puchtler, and Y. Clermont, *Structures corresponding to terminal bars and terminal web in many types of cells*. Nature, 1960. **186**: p. 784-8.
43. Drenckhahn, D. and U. Gröschel-Stewart, *Localization of myosin, actin, and tropomyosin in rat intestinal epithelium: immunohistochemical studies at the light and electron microscope levels*. J Cell Biol, 1980. **86**(2): p. 475-82.
44. Keller, T.C., 3rd, et al., *Role of myosin in terminal web contraction in isolated intestinal epithelial brush borders*. J Cell Biol, 1985. **100**(5): p. 1647-55.
45. Mooseker, M.S., T.D. Pollard, and K. Fujiwara, *Characterization and localization of myosin in the brush border of intestinal epithelial cells*. J Cell Biol, 1978. **79**(2 Pt 1): p. 444-53.
46. Glenney, J.R., Jr. and P. Glenney, *Fodrin is the general spectrin-like protein found in most cells whereas spectrin and the TW protein have a restricted distribution*. Cell, 1983. **34**(2): p. 503-12.
47. Glenney, J.R., Jr., et al., *An F-actin- and calmodulin-binding protein from isolated intestinal brush borders has a morphology related to spectrin*. Cell, 1982. **28**(4): p. 843-54.
48. Gaeta, I.M., et al., *Direct visualization of epithelial microvilli biogenesis*. Current Biology, 2021. **31**(12): p. 2561-2575.e6.
49. Pollard, T.D. and G.G. Borisy, *Cellular motility driven by assembly and disassembly of actin filaments*. Cell, 2003. **112**(4): p. 453-65.
50. Borisy, G.G. and T.M. Svitkina, *Actin machinery: pushing the envelope*. Curr Opin Cell Biol, 2000. **12**(1): p. 104-12.
51. Footer, M.J., et al., *Direct measurement of force generation by actin filament polymerization using an optical trap*. Proceedings of the National Academy of Sciences, 2007. **104**(7): p. 2181-2186.
52. Meenderink, L.M., et al., *Actin Dynamics Drive Microvillar Motility and Clustering during Brush Border Assembly*. Dev Cell, 2019. **50**(5): p. 545-556.e4.
53. Schwander, M., B. Kachar, and U. Müller, *Review series: The cell biology of hearing*. J Cell Biol, 2010. **190**(1): p. 9-20.
54. McGrath, J., P. Roy, and B.J. Perrin, *Stereocilia morphogenesis and maintenance through regulation of actin stability*. Semin Cell Dev Biol, 2017. **65**: p. 88-95.
55. Prost, J., C. Barbetta, and J.F. Joanny, *Dynamical control of the shape and size of stereocilia and microvilli*. Biophys J, 2007. **93**(4): p. 1124-33.
56. Furness, D.N., et al., *The dimensions and composition of stereociliary rootlets in mammalian cochlear hair cells: comparison between high- and low-frequency cells and evidence for a connection to the lateral membrane*. J Neurosci, 2008. **28**(25): p. 6342-53.

57. Seipel, K., et al., *Tara, a novel F-actin binding protein, associates with the Trio guanine nucleotide exchange factor and regulates actin cytoskeletal organization*. J Cell Sci, 2001. **114**(Pt 2): p. 389-99.
58. Zine, E.A. and R. Romand, *Expression of alpha-actinin in the stereocilia of hair cells of the inner ear: immunohistochemical localization*. Neuroreport, 1993. **4**(12): p. 1350-2.
59. Gillespie, P.G. and U. Müller, *Mechanotransduction by hair cells: models, molecules, and mechanisms*. Cell, 2009. **139**(1): p. 33-44.
60. Sakaguchi, H., et al., *Tip links in hair cells: molecular composition and role in hearing loss*. Curr Opin Otolaryngol Head Neck Surg, 2009. **17**(5): p. 388-93.
61. Iino, R., K. Kinbara, and Z. Bryant, *Introduction: Molecular Motors*. Chemical Reviews, 2020. **120**(1): p. 1-4.
62. Hartman, M.A. and J.A. Spudich, *The myosin superfamily at a glance*. J Cell Sci, 2012. **125**(Pt 7): p. 1627-32.
63. Foth, B.J., M.C. Goedecke, and D. Soldati, *New insights into myosin evolution and classification*. Proc Natl Acad Sci U S A, 2006. **103**(10): p. 3681-6.
64. Kühne, W., *Untersuchungen über das Protoplasma und die Contractilität*. 1864: W. Engelmann.
65. Chantler, P.D., et al., *Conventional myosins - unconventional functions*. Biophys Rev, 2010. **2**(2): p. 67-82.
66. Cope, M.J., et al., *Conservation within the myosin motor domain: implications for structure and function*. Structure, 1996. **4**(8): p. 969-87.
67. De La Cruz, E.M. and E.M. Ostap, *Relating biochemistry and function in the myosin superfamily*. Curr Opin Cell Biol, 2004. **16**(1): p. 61-7.
68. McNally, E.M., M.M. Bravo-Zehnder, and L.A. Leinwand, *Identification of sequences necessary for the association of cardiac myosin subunits*. J Cell Biol, 1991. **113**(3): p. 585-90.
69. Houdusse, A. and C. Cohen, *Target sequence recognition by the calmodulin superfamily: implications from light chain binding to the regulatory domain of scallop myosin*. Proc Natl Acad Sci U S A, 1995. **92**(23): p. 10644-7.
70. Krendel, M. and M.S. Mooseker, *Myosins: tails (and heads) of functional diversity*. Physiology (Bethesda), 2005. **20**: p. 239-51.
71. Atkinson, S.J. and M. Stewart, *Molecular interactions in myosin assembly. Role of the 28-residue charge repeat in the rod*. J Mol Biol, 1992. **226**(1): p. 7-13.
72. Dulyaninova, N.G. and A.R. Bresnick, *The heavy chain has its day: regulation of myosin-II assembly*. Bioarchitecture, 2013. **3**(4): p. 77-85.
73. Betapudi, V., *Life without double-headed non-muscle myosin II motor proteins*. Front Chem, 2014. **2**: p. 45.
74. Lizio, M., et al., *Gateways to the FANTOM5 promoter level mammalian expression atlas*. Genome Biol, 2015. **16**(1): p. 22.
75. *The Genotype-Tissue Expression (GTEx) project*. Nat Genet, 2013. **45**(6): p. 580-5.
76. Heissler, S.M. and D.J. Manstein, *Nonmuscle myosin-2: mix and match*. Cell Mol Life Sci, 2013. **70**(1): p. 1-21.
77. Shutova, M.S. and T.M. Svitkina, *Common and Specific Functions of Nonmuscle Myosin II Paralogs in Cells*. Biochemistry (Mosc), 2018. **83**(12): p. 1459-1468.

78. Beach, J.R., et al., *Nonmuscle myosin II isoforms coassemble in living cells*. *Curr Biol*, 2014. **24**(10): p. 1160-6.
79. Fenix, A.M. and D.T. Burnette, *Assembly of myosin II filament arrays: Network Contraction versus Expansion*. *Cytoskeleton (Hoboken)*, 2018. **75**(12): p. 545-549.
80. Conti, M.A., et al., *Defects in cell adhesion and the visceral endoderm following ablation of nonmuscle myosin heavy chain II-A in mice*. *J Biol Chem*, 2004. **279**(40): p. 41263-6.
81. Ma, X., et al., *Ablation of nonmuscle myosin II-B and II-C reveals a role for nonmuscle myosin II in cardiac myocyte karyokinesis*. *Mol Biol Cell*, 2010. **21**(22): p. 3952-62.
82. Golomb, E., et al., *Identification and characterization of nonmuscle myosin II-C, a new member of the myosin II family*. *J Biol Chem*, 2004. **279**(4): p. 2800-8.
83. Ebrahim, S., et al., *NMII forms a contractile transcellular sarcomeric network to regulate apical cell junctions and tissue geometry*. *Curr Biol*, 2013. **23**(8): p. 731-6.
84. Norio, Y., et al., *Myosin II regulates extension, growth and patterning in the mammalian cochlear duct*. *Journal of Cell Science*, 2009.
85. Ishan Sunilkumar, B., et al., *Association Analysis of Candidate Gene Polymorphisms and Audiometric Measures of Noise-Induced Hearing Loss in Young Musicians*. *Otology & Neurotology*, 2020.
86. Annelies, K., et al., *Candidate gene association study for noise-induced hearing loss in two independent noise-exposed populations*. *Annals of Human Genetics*, 2009.
87. Liang, W., et al., *Cochlear nerve canal stenosis association with myh14 and myh9 genes*. *Ear, nose, & throat journal*, 2021.
88. Bong Jik, K., et al., *Discovery of MYH14 as an important and unique deafness gene causing prelingually severe autosomal dominant nonsyndromic hearing loss*. *Journal of Gene Medicine*, 2017.
89. Sang-Joo, K., et al., *Genetic association of MYH genes with hereditary hearing loss in Korea*. *Gene*, 2016.
90. Mee Hyun, S., et al., *Genetic Inheritance of Late-Onset, Down-Sloping Hearing Loss and Its Implications for Auditory Rehabilitation*. *Ear and Hearing*, 2020.
91. Lerat, J., et al., *Hearing loss in inherited peripheral neuropathies: Molecular diagnosis by NGS in a French series*. *Mol Genet Genomic Med*, 2019. **7**(9): p. e839.
92. Fu, X., et al., *Loss of Myh14 Increases Susceptibility to Noise-Induced Hearing Loss in CBA/CaJ Mice*. *Neural Plast*, 2016. **2016**: p. 6720420.
93. Mingming, W., et al., *A novel MYH14 mutation in a Chinese family with autosomal dominant nonsyndromic hearing loss*. *BMC Medical Genetics*, 2020.
94. Stanley, I., et al., *Variable phenotypic expression and onset in MYH14 distal hereditary motor neuropathy phenotype in a large, multigenerational North American family*. *Muscle & Nerve*, 2017.
95. Huxley, A.F. and R.M. Simmons, *Proposed mechanism of force generation in striated muscle*. *Nature*, 1971. **233**(5321): p. 533-8.

96. Ebrahim, S., O. Milberg, and R. Weigert, *Isoform-specific roles of NMII drive membrane remodeling in vivo*. *Cell Cycle*, 2017. **16**(20): p. 1851-1852.
97. Newell-Litwa, K.A., R. Horwitz, and M.L. Lamers, *Non-muscle myosin II in disease: mechanisms and therapeutic opportunities*. *Dis Model Mech*, 2015. **8**(12): p. 1495-515.
98. Beach, J.R. and J.A. Hammer, 3rd, *Myosin II isoform co-assembly and differential regulation in mammalian systems*. *Exp Cell Res*, 2015. **334**(1): p. 2-9.
99. Gomez, G.A., R.W. McLachlan, and A.S. Yap, *Productive tension: force-sensing and homeostasis of cell-cell junctions*. *Trends Cell Biol*, 2011. **21**(9): p. 499-505.
100. Stam, S., et al., *Isoforms Confer Characteristic Force Generation and Mechanosensation by Myosin II Filaments*. *Biophys J*, 2015. **108**(8): p. 1997-2006.
101. Thompson, D.A.W., *On Growth and Form*. 1917: Cambridge University Press.
102. Murrell, M., et al., *Forcing cells into shape: the mechanics of actomyosin contractility*. *Nature Reviews Molecular Cell Biology*, 2015. **16**(8): p. 486-498.
103. Sun, S.X., S. Walcott, and C.W. Wolgemuth, *Cytoskeletal cross-linking and bundling in motor-independent contraction*. *Curr Biol*, 2010. **20**(15): p. R649-54.
104. Chugh, P. and E.K. Paluch, *The actin cortex at a glance*. *J Cell Sci*, 2018. **131**(14).
105. Martin, A.C., *Pulsation and stabilization: contractile forces that underlie morphogenesis*. *Dev Biol*, 2010. **341**(1): p. 114-25.
106. Martin, A.C., et al., *Integration of contractile forces during tissue invagination*. *Journal of Cell Biology*, 2010. **188**(5): p. 735-749.
107. Coravos, J.S. and A.C. Martin, *Apical Sarcomere-like Actomyosin Contracts Nonmuscle Drosophila Epithelial Cells*. *Dev Cell*, 2016. **39**(3): p. 346-358.
108. Bertet, C., L. Sulak, and T. Lecuit, *Myosin-dependent junction remodelling controls planar cell intercalation and axis elongation*. *Nature*, 2004. **429**(6992): p. 667-671.
109. Engl, W., et al., *Actin dynamics modulate mechanosensitive immobilization of E-cadherin at adherens junctions*. *Nature Cell Biology*, 2014. **16**(6): p. 584-591.
110. Michael, M., X. Liang, and G.A. Gomez, *Analysis of Myosin II Minifilament Orientation at Epithelial Zonula Adherens*. *Bio Protoc*, 2016. **6**(23).
111. Heer, N.C. and A.C. Martin, *Tension, contraction and tissue morphogenesis*. *Development*, 2017. **144**(23): p. 4249-4260.
112. Guha, M., M. Zhou, and Y.L. Wang, *Cortical actin turnover during cytokinesis requires myosin II*. *Curr Biol*, 2005. **15**(8): p. 732-6.
113. Murthy, K. and P. Wadsworth, *Myosin-II-dependent localization and dynamics of F-actin during cytokinesis*. *Curr Biol*, 2005. **15**(8): p. 724-31.
114. Wu, J.Q., et al., *Spatial and temporal pathway for assembly and constriction of the contractile ring in fission yeast cytokinesis*. *Dev Cell*, 2003. **5**(5): p. 723-34.
115. Wu, J.Q., et al., *Assembly of the cytokinetic contractile ring from a broad band of nodes in fission yeast*. *J Cell Biol*, 2006. **174**(3): p. 391-402.
116. Arnold, T.R., et al., *Anillin regulates epithelial cell mechanics by structuring the medial-apical actomyosin network*. *Elife*, 2019. **8**.
117. Harris, T.J.C. and U. Tepass, *Adherens junctions: from molecules to morphogenesis*. *Nature Reviews Molecular Cell Biology*, 2010. **11**(7): p. 502-514.

118. Shindo, A., *Models of convergent extension during morphogenesis*. Wiley Interdiscip Rev Dev Biol, 2018. **7**(1).
119. Stanfield, C., *Principles of Human Physiology*. 2017: Pearson.
120. VanDussen, K.L., et al., *Abnormal Small Intestinal Epithelial Microvilli in Patients With Crohn's Disease*. Gastroenterology, 2018. **155**(3): p. 815-828.
121. Secondulfo, M., et al., *Ultrastructural mucosal alterations and increased intestinal permeability in non-celiac, type I diabetic patients*. Dig Liver Dis, 2004. **36**(1): p. 35-45.
122. Helander, H.F. and L. Fändriks, *Surface area of the digestive tract – revisited*. Scandinavian Journal of Gastroenterology, 2014. **49**(6): p. 681-689.
123. van der Flier, L.G. and H. Clevers, *Stem cells, self-renewal, and differentiation in the intestinal epithelium*. Annu Rev Physiol, 2009. **71**: p. 241-60.
124. Lieberkühn, J.N., *Joannis Nathanael Lieberkühn... Dissertatio anatomico-physiologica de fabrica et actione villorum intestinorum tenuium hominis. Iconibus aeri incisus illustrata*. Vol. 1. 1745: apud Conrad et Georg. Jac. Wishof.
125. De Sousa E Melo, F. and F.J. De Sauvage, *Cellular Plasticity in Intestinal Homeostasis and Disease*. Cell Stem Cell, 2019. **24**(1): p. 54-64.
126. Chin, A.M., et al., *Morphogenesis and maturation of the embryonic and postnatal intestine*. Seminars in Cell & Developmental Biology, 2017. **66**: p. 81-93.
127. Shyer, A.E., et al., *Villification: How the Gut Gets Its Villi*. Science, 2013. **342**(6155): p. 212-218.
128. Sumigray, K.D., M. Terwilliger, and T. Lechler, *Morphogenesis and Compartmentalization of the Intestinal Crypt*. Developmental Cell, 2018. **45**(2): p. 183-197.e5.
129. Kelsen, D., *Principles and Practice of Gastrointestinal Oncology*. 2008: Lippincott, Williams & Wilkins.
130. Feil, W., et al., *Rapid epithelial restitution of human and rabbit colonic mucosa*. Gastroenterology, 1989. **97**(3): p. 685-701.
131. Krndija, D., et al., *Active cell migration is critical for steady-state epithelial turnover in the gut*. Science, 2019. **365**(6454): p. 705-710.
132. Cheng, H. and C.P. Leblond, *Origin, differentiation and renewal of the four main epithelial cell types in the mouse small intestine V. Unitarian theory of the origin of the four epithelial cell types*. American Journal of Anatomy, 1974. **141**(4): p. 537-561.
133. Cheng, H. and C.P. Leblond, *Origin, differentiation and renewal of the four main epithelial cell types in the mouse small intestine. I. Columnar cell*. Am J Anat, 1974. **141**(4): p. 461-79.
134. Noah, T.K., B. Donahue, and N.F. Shroyer, *Intestinal development and differentiation*. Exp Cell Res, 2011. **317**(19): p. 2702-10.
135. Rhodin, J. and T. Dalhamn, *Electron microscopy of the tracheal ciliated mucosa in rat*. Zeitschrift für Zellforschung und mikroskopische Anatomie, 1956. **44**(4): p. 345-412.
136. Herring, C.A., et al., *Unsupervised Trajectory Analysis of Single-Cell RNA-Seq and Imaging Data Reveals Alternative Tuft Cell Origins in the Gut*. Cell Systems, 2018. **6**(1): p. 37-51.e9.

137. Ting, H.-A. and J. von Moltke, *The Immune Function of Tuft Cells at Gut Mucosal Surfaces and Beyond*. The Journal of Immunology, 2019. **202**(5): p. 1321-1329.
138. Howitt, M.R., et al., *Tuft cells, taste-chemosensory cells, orchestrate parasite type 2 immunity in the gut*. Science, 2016. **351**(6279): p. 1329-33.
139. Gribble, F.M. and F. Reimann, *Function and mechanisms of enteroendocrine cells and gut hormones in metabolism*. Nature Reviews Endocrinology, 2019. **15**(4): p. 226-237.
140. Worthington, J.J., *The intestinal immunoendocrine axis: novel cross-talk between enteroendocrine cells and the immune system during infection and inflammatory disease*. Biochem Soc Trans, 2015. **43**(4): p. 727-33.
141. Koh-en, Y. and T. Prapakorn, *Changes in intestinal villi, cell area and intracellular autophagic vacuoles related to intestinal function in chickens*. British Poultry Science, 2000.
142. Koh-en, Y., K. Hiroshi, and I. Yutaka, *Effects of fasting and refeeding on structures of the intestinal villi and epithelial cells in White Leghorn hens*. British Poultry Science, 1996.
143. Palay, S.L. and L.J. Karlin, *An electron microscopic study of the intestinal villus. I. The fasting animal*. J Biophys Biochem Cytol, 1959. **5**(3): p. 363-72.
144. Palay, S.L. and L.J. Karlin, *An electron microscopic study of the intestinal villus. II. The pathway of fat absorption*. J Biophys Biochem Cytol, 1959. **5**(3): p. 373-84.
145. Ferrary, E., et al., *In vivo, villin is required for Ca(2+)-dependent F-actin disruption in intestinal brush borders*. J Cell Biol, 1999. **146**(4): p. 819-30.
146. Koh-en, Y., Y. Ken, and I. Yutaka, *Morphological Alterations of the Intestinal Villi and Absorptive Epithelial Cells in each Intestinal part in Fasted Chickens*. Journal of Poultry Science, 1995.
147. Yanling, D., et al., *Morphometric and biomechanical intestinal remodeling induced by fasting in rats*. Digestive Diseases and Sciences, 2002.
148. Shamoto, K. and Y. Koh-en, *Recovery responses of chick intestinal villus morphology to different refeeding procedures*. Poultry Science, 2000.
149. Suzanne, D.-E., et al., *Restoration of the jejunal mucosa in rats refed after prolonged fasting*. Comparative Biochemistry and Physiology A-molecular & Integrative Physiology, 2001.
150. Starck, J.M., J.M. Starck, and B. Kathleen, *Structural flexibility of the small intestine and liver of garter snakes in response to feeding and fasting*. The Journal of Experimental Biology, 2002.
151. Clarke, R. and M.C. Rufus, *The time-course of changes in mucosal architecture and epithelial cell production and cell shedding in the small intestine of the rat fed after fasting*. Journal of Anatomy, 1975.
152. Helander, H.F. and L. Fandriks, *Surface area of the digestive tract - revisited*. Scand J Gastroenterol, 2014. **49**(6): p. 681-9.
153. Knutton, S., et al., *The attaching and effacing virulence property of enteropathogenic Escherichia coli*. Zentralbl Bakteriol, 1993. **278**(2-3): p. 209-17.
154. Grimm-Gunter, E.M., et al., *Plastin 1 binds to keratin and is required for terminal web assembly in the intestinal epithelium*. Mol Biol Cell, 2009. **20**(10): p. 2549-62.

155. Postema, M.M., et al., *PACSIN2-dependent apical endocytosis regulates the morphology of epithelial microvilli*. *Mol Biol Cell*, 2019. **30**(19): p. 2515-2526.
156. Revenu, C., et al., *A new role for the architecture of microvillar actin bundles in apical retention of membrane proteins*. *Mol Biol Cell*, 2012. **23**(2): p. 324-36.
157. Hirokawa, N., et al., *Organization of actin, myosin, and intermediate filaments in the brush border of intestinal epithelial cells*. *J Cell Biol*, 1982. **94**(2): p. 425-43.
158. Mooseker, M.S., et al., *Regulation of microvillus structure: calcium-dependent solation and cross-linking of actin filaments in the microvilli of intestinal epithelial cells*. *J Cell Biol*, 1980. **87**(3 Pt 1): p. 809-22.
159. Mooseker, M.S., et al., *Brush border cytoskeleton and integration of cellular functions*. *J Cell Biol*, 1984. **99**(1 Pt 2): p. 104s-112s.
160. Howe, C.L., et al., *Mechanisms of cytoskeletal regulation: modulation of membrane affinity in avian brush border and erythrocyte spectrins*. *J Cell Biol*, 1985. **101**(4): p. 1379-85.
161. Heissler, S.M. and D.J. Manstein, *Comparative kinetic and functional characterization of the motor domains of human nonmuscle myosin-2C isoforms*. *J Biol Chem*, 2011. **286**(24): p. 21191-202.
162. Jana, S.S., et al., *An alternatively spliced isoform of non-muscle myosin II-C is not regulated by myosin light chain phosphorylation*. *J Biol Chem*, 2009. **284**(17): p. 11563-71.
163. McLachlan, A.D. and J. Karn, *Periodic charge distributions in the myosin rod amino acid sequence match cross-bridge spacings in muscle*. *Nature*, 1982. **299**(5880): p. 226-31.
164. Kim, K.Y., et al., *Disease-associated mutations and alternative splicing alter the enzymatic and motile activity of nonmuscle myosins II-B and II-C*. *J Biol Chem*, 2005. **280**(24): p. 22769-75.
165. McConnell, R.E., et al., *Proteomic analysis of the enterocyte brush border*. *Am J Physiol Gastrointest Liver Physiol*, 2011. **300**(5): p. G914-26.
166. Eliahu, G., et al., *Identification and Characterization of Nonmuscle Myosin II-C, a New Member of the Myosin II Family*. *Journal of Biological Chemistry*, 2004.
167. Francesca, D., et al., *Nonmuscle Myosin Heavy-Chain Gene MYH14 Is Expressed in Cochlea and Mutated in Patients Affected by Autosomal Dominant Hearing Impairment (DFNA4)*. *American Journal of Human Genetics*, 2004.
168. Xiaolong, F., et al., *Loss of Myh14 Increases Susceptibility to Noise-Induced Hearing Loss in CBA/Cal Mice*. *Neural Plasticity*, 2016.
169. Zhu, Z., et al., *Mutations of MYH14 are associated to anorectal malformations with recto-perineal fistulas in a small subset of Chinese population*. *Clin Genet*, 2017. **92**(5): p. 503-509.
170. Almutawa, W., et al., *The R941L mutation in MYH14 disrupts mitochondrial fission and associates with peripheral neuropathy*. *EBioMedicine*, 2019. **45**: p. 379-392.
171. Han, J.J., et al., *Elucidation of the unique mutation spectrum of severe hearing loss in a Vietnamese pediatric population*. *Sci Rep*, 2019. **9**(1): p. 1604.
172. Mathur, P. and J. Yang, *Usher syndrome: Hearing loss, retinal degeneration and associated abnormalities*. *Biochim Biophys Acta*, 2015. **1852**(3): p. 406-20.

173. Southard-Smith, A.N., et al., *Dual indexed library design enables compatibility of in-Drop single-cell RNA-sequencing with exAMP chemistry sequencing platforms*. BMC Genomics, 2020. **21**(1): p. 456.
174. Banerjee, A., et al., *Succinate Produced by Intestinal Microbes Promotes Specification of Tuft Cells to Suppress Ileal Inflammation*. Gastroenterology, 2020. **159**(6): p. 2101-2115.e5.
175. Baas, A.F., et al., *Complete polarization of single intestinal epithelial cells upon activation of LKB1 by STRAD*. Cell, 2004. **116**(3): p. 457-66.
176. Grega-Larson, N.E., et al., *Cordon bleu promotes the assembly of brush border microvilli*. Mol Biol Cell, 2015. **26**(21): p. 3803-15.
177. ten Klooster, J.P., et al., *Mst4 and Ezrin induce brush borders downstream of the Lkb1/Strad/Mo25 polarization complex*. Dev Cell, 2009. **16**(4): p. 551-62.
178. Suganuma, M., et al., *Calyculin A, an inhibitor of protein phosphatases, a potent tumor promoter on CD-1 mouse skin*. Cancer Res, 1990. **50**(12): p. 3521-5.
179. Suzuki, A. and T. Itoh, *Effects of calyculin A on tension and myosin phosphorylation in skinned smooth muscle of the rabbit mesenteric artery*. Br J Pharmacol, 1993. **109**(3): p. 703-12.
180. Watanabe, T., H. Hosoya, and S. Yonemura, *Regulation of myosin II dynamics by phosphorylation and dephosphorylation of its light chain in epithelial cells*. Mol Biol Cell, 2007. **18**(2): p. 605-16.
181. Surcel, A., et al., *Pharmacological activation of myosin II paralogs to correct cell mechanics defects*. Proc Natl Acad Sci U S A, 2015. **112**(5): p. 1428-33.
182. Surcel, A., et al., *Targeting Mechanoresponsive Proteins in Pancreatic Cancer: 4-Hydroxyacetophenone Blocks Dissemination and Invasion by Activating MYH14*. Cancer Res, 2019. **79**(18): p. 4665-4678.
183. Kovacs, M., et al., *Mechanism of blebbistatin inhibition of myosin II*. J Biol Chem, 2004. **279**(34): p. 35557-63.
184. Limouze, J., et al., *Specificity of blebbistatin, an inhibitor of myosin II*. J Muscle Res Cell Motil, 2004. **25**(4-5): p. 337-41.
185. Bonder, E.M., D.J. Fishkind, and M.S. Mooseker, *Direct measurement of critical concentrations and assembly rate constants at the two ends of an actin filament*. Cell, 1983. **34**(2): p. 491-501.
186. Brenner, S.L. and E.D. Korn, *On the mechanism of actin monomer-polymer subunit exchange at steady state*. J Biol Chem, 1983. **258**(8): p. 5013-20.
187. Wang, Y.L., *Exchange of actin subunits at the leading edge of living fibroblasts: possible role of treadmilling*. J Cell Biol, 1985. **101**(2): p. 597-602.
188. Shimada, T., et al., *Alanine scanning mutagenesis of the switch I region in the ATPase site of Dictyostelium discoideum myosin II*. Biochemistry, 1997. **36**(46): p. 14037-43.
189. Kuhlman, P.A. and C.R. Bagshaw, *ATPase kinetics of the Dictyostelium discoideum myosin II motor domain*. J Muscle Res Cell Motil, 1998. **19**(5): p. 491-504.
190. Sasaki, N., R. Ohkura, and K. Sutoh, *Dictyostelium myosin II mutations that uncouple the converter swing and ATP hydrolysis cycle*. Biochemistry, 2003. **42**(1): p. 90-5.

191. Kambara, T., et al., *Functional significance of the conserved residues in the flexible hinge region of the myosin motor domain*. J Biol Chem, 1999. **274**(23): p. 16400-6.
192. Sasaki, N., T. Shimada, and K. Sutoh, *Mutational analysis of the switch II loop of Dictyostelium myosin II*. J Biol Chem, 1998. **273**(32): p. 20334-40.
193. Chinthalapudi, K., et al., *Mechanistic insights into the active site and allosteric communication pathways in human nonmuscle myosin-2C*. Elife, 2017. **6**.
194. Sakai, T., et al., *Cargo binding activates myosin VIIA motor function in cells*. Proc Natl Acad Sci U S A, 2011. **108**(17): p. 7028-33.
195. Belyantseva, I.A., et al., *Myosin-XVa is required for tip localization of whirlin and differential elongation of hair-cell stereocilia*. Nat Cell Biol, 2005. **7**(2): p. 148-56.
196. Lonsdale, J., et al., *The Genotype-Tissue Expression (GTEx) project*. Nature Genetics, 2013. **45**(6): p. 580-585.
197. Huxley, H.E., *The double array of filaments in cross-striated muscle*. J Biophys Biochem Cytol, 1957. **3**(5): p. 631-48.
198. Huxley, H.E., *The mechanism of muscular contraction*. Science, 1969. **164**(3886): p. 1356-65.
199. Vicente-Manzanares, M., et al., *Non-muscle myosin II takes centre stage in cell adhesion and migration*. Nat Rev Mol Cell Biol, 2009. **10**(11): p. 778-90.
200. Turner, J.R., et al., *Physiological regulation of epithelial tight junctions is associated with myosin light-chain phosphorylation*. Am J Physiol, 1997. **273**(4): p. C1378-85.
201. Medeiros, N.A., D.T. Burnette, and P. Forscher, *Myosin II functions in actin-bundle turnover in neuronal growth cones*. Nat Cell Biol, 2006. **8**(3): p. 215-26.
202. Ivanov, A.I., et al., *Differential roles for actin polymerization and a myosin II motor in assembly of the epithelial apical junctional complex*. Mol Biol Cell, 2005. **16**(6): p. 2636-50.
203. Tyska, M.J. and M.S. Mooseker, *MYO1A (brush border myosin I) dynamics in the brush border of LLC-PK1-CL4 cells*. Biophys J, 2002. **82**(4): p. 1869-83.
204. Haviv, L., et al., *A cytoskeletal demolition worker: myosin II acts as an actin depolymerization agent*. J Mol Biol, 2008. **375**(2): p. 325-30.
205. Zhang, X.F., et al., *Regulation of axon growth by myosin II-dependent mechanocatalysis of cofilin activity*. J Cell Biol, 2019. **218**(7): p. 2329-2349.
206. McCullough, B.R., et al., *Cofilin increases the bending flexibility of actin filaments: implications for severing and cell mechanics*. J Mol Biol, 2008. **381**(3): p. 550-8.
207. De La Cruz, E.M., J.L. Martiel, and L. Blanchoin, *Mechanical heterogeneity favors fragmentation of strained actin filaments*. Biophys J, 2015. **108**(9): p. 2270-81.
208. Schramm, A.C., et al., *Actin Filament Strain Promotes Severing and Cofilin Dissociation*. Biophys J, 2017. **112**(12): p. 2624-2633.
209. Yu, L.C.-H., *Host-microbial interactions and regulation of intestinal epithelial barrier function: From physiology to pathology*. World Journal of Gastrointestinal Pathophysiology, 2012. **3**(1): p. 27.

210. Chelakkot, C., J. Ghim, and S.H. Ryu, *Mechanisms regulating intestinal barrier integrity and its pathological implications*. *Experimental & Molecular Medicine*, 2018. **50**(8): p. 1-9.
211. Camilleri, M., et al., *Intestinal barrier function in health and gastrointestinal disease*. *Neurogastroenterology & Motility*, 2012. **24**(6): p. 503-512.
212. Takashima, S., D. Gold, and V. Hartenstein, *Stem cells and lineages of the intestine: a developmental and evolutionary perspective*. *Development Genes and Evolution*, 2013. **223**(1-2): p. 85-102.
213. Barker, N., et al., *Identification of stem cells in small intestine and colon by marker gene *Lgr5**. *Nature*, 2007. **449**(7165): p. 1003-1007.
214. Starck, J.M. and K. Beese, *Structural flexibility of the intestine of Burmese python in response to feeding*. *The Journal of Experimental Biology*, 2001.
215. Willems, G., Y. Vansteenkiste, and P. Smets, *Effects of Food Ingestion on the Cell Proliferation Kinetics in the Canine Fundic Mucosa*. *Gastroenterology*, 1971. **61**(3): p. 323-327.
216. Parker, A., et al., *Cell proliferation within small intestinal crypts is the principal driving force for cell migration on villi*. *The FASEB Journal*, 2017. **31**(2): p. 636-649.
217. Friedl, P. and D. Gilmour, *Collective cell migration in morphogenesis, regeneration and cancer*. *Nature Reviews Molecular Cell Biology*, 2009. **10**(7): p. 445-457.
218. Xi, W., et al., *Emergent patterns of collective cell migration under tubular confinement*. *Nature Communications*, 2017. **8**(1).
219. Barth, A.I.M., H. Kim, and I.H. Riedel-Kruse, *Regulation of epithelial migration by epithelial cell adhesion molecule requires its Claudin-7 interaction domain*. *PLOS ONE*, 2018. **13**(10): p. e0204957.
220. Worley, K.E., D. Shieh, and L.Q. Wan, *Inhibition of cell–cell adhesion impairs directional epithelial migration on micropatterned surfaces*. *Integrative Biology*, 2015. **7**(5): p. 580-590.
221. Gumbiner, B.M., *Cell Adhesion: The Molecular Basis of Tissue Architecture and Morphogenesis*. *Cell*, 1996. **84**(3): p. 345-357.
222. Efstathiou, J.A. and M. Pignatelli, *Modulation of Epithelial Cell Adhesion in Gastrointestinal Homeostasis*. *The American Journal of Pathology*, 1998. **153**(2): p. 341-347.
223. Förster, C., *Tight junctions and the modulation of barrier function in disease*. *Histochemistry and Cell Biology*, 2008. **130**(1): p. 55-70.
224. Farquhar, M.G. and G.E. Palade, *JUNCTIONAL COMPLEXES IN VARIOUS EPITHELIA*. *Journal of Cell Biology*, 1963. **17**(2): p. 375-412.
225. Paradis, T., et al., *Tight Junctions as a Key for Pathogens Invasion in Intestinal Epithelial Cells*. *International Journal of Molecular Sciences*, 2021. **22**(5): p. 2506.
226. Delva, E., D.K. Tucker, and A.P. Kowalczyk, *The Desmosome*. *Cold Spring Harbor Perspectives in Biology*, 2009. **1**(2): p. a002543-a002543.
227. Friedl, P. and R. Mayor, *Tuning Collective Cell Migration by Cell–Cell Junction Regulation*. *Cold Spring Harbor Perspectives in Biology*, 2017. **9**(4): p. a029199.

228. Turner, J.R., *Intestinal mucosal barrier function in health and disease*. Nature Reviews Immunology, 2009. **9**(11): p. 799-809.
229. Liu, Z., et al., *Mechanical tugging force regulates the size of cell-cell junctions*. Proceedings of the National Academy of Sciences, 2010. **107**(22): p. 9944-9949.
230. Wang, F., et al., *Interferon- γ and Tumor Necrosis Factor- α Synergize to Induce Intestinal Epithelial Barrier Dysfunction by Up-Regulating Myosin Light Chain Kinase Expression*. The American Journal of Pathology, 2005. **166**(2): p. 409-419.
231. Aldaz, S., L.M. Escudero, and M. Freeman, *Dual role of myosin II during Drosophila imaginal disc metamorphosis*. Nature Communications, 2013. **4**(1): p. 1761.
232. Collinet, C., et al., *Local and tissue-scale forces drive oriented junction growth during tissue extension*. Nature Cell Biology, 2015. **17**(10): p. 1247-1258.
233. Weber, C.R., et al., *Epithelial Myosin Light Chain Kinase Activation Induces Mucosal Interleukin-13 Expression to Alter Tight Junction Ion Selectivity*. Journal of Biological Chemistry, 2010. **285**(16): p. 12037-12046.
234. Chinowsky, C.R., et al., *Nonmuscle myosin-2 contractility-dependent actin turnover limits the length of epithelial microvilli*. Molecular biology of the cell, 2020.
235. Bitner-Glindzicz, M., et al., *A recessive contiguous gene deletion causing infantile hyperinsulinism, enteropathy and deafness identifies the Usher type 1C gene*. Nature Genetics, 2000. **26**(1): p. 56-60.
236. Fousekis, F.S., et al., *Ear Involvement in Inflammatory Bowel Disease: A Review of the Literature*. Journal of Clinical Medicine Research, 2018. **10**(8): p. 609-614.
237. Pinette, J.A., et al., *Brush border protocadherin CDHR2 promotes the elongation and maximized packing of microvilli in vivo*. Mol Biol Cell, 2019. **30**(1): p. 108-118.
238. Hirokawa, N., et al., *Mechanism of brush border contractility studied by the quick-freeze, deep-etch method*. J Cell Biol, 1983. **96**(5): p. 1325-36.
239. Shen, L., et al., *Myosin light chain phosphorylation regulates barrier function by remodeling tight junction structure*. Journal of Cell Science, 2006. **119**(10): p. 2095-2106.
240. Bailey, D.S., et al., *Early biochemical responses of the small intestine of coeliac patients to wheat gluten*. Gut, 1989. **30**(1): p. 78-85.
241. Ho, W.-T., et al., *Targeting non-muscle myosin II promotes corneal endothelial migration through regulating lamellipodial dynamics*. Journal of Molecular Medicine, 2019. **97**(9): p. 1345-1357.
242. Lynn, K.S., R.J. Peterson, and M. Koval, *Ruffles and spikes: Control of tight junction morphology and permeability by claudins*. Biochim Biophys Acta Biomembr, 2020. **1862**(9): p. 183339.
243. Bazellières, E., et al., *Control of cell–cell forces and collective cell dynamics by the intercellular adhesome*. Nature Cell Biology, 2015. **17**(4): p. 409-420.
244. Gayar, C.P. and M.D. Basson, *The effects of mechanical forces on intestinal physiology and pathology*. Cellular Signalling, 2009. **21**(8): p. 1237-1244.
245. Bamburg, J.R. and B.W. Bernstein, *Roles of ADF/cofilin in actin polymerization and beyond*. F1000 Biol Rep, 2010. **2**: p. 62.

246. Niwa, R., et al., *Control of actin reorganization by Slingshot, a family of phosphatases that dephosphorylate ADF/cofilin*. Cell, 2002. **108**(2): p. 233-46.
247. Lee, S.Y., et al., *Identification of sennoside A as a novel inhibitor of the slingshot (SSH) family proteins related to cancer metastasis*. Pharmacol Res, 2017. **119**: p. 422-430.
248. Jia, R.X., et al., *LIMK1/2 inhibitor LIMKi 3 suppresses porcine oocyte maturation*. PeerJ, 2016. **4**: p. e2553.
249. Prunier, C., et al., *LIM kinases: cofilin and beyond*. Oncotarget, 2017. **8**(25): p. 41749-41763.
250. Mead, T.J. and V. Lefebvre, *Proliferation assays (BrdU and EdU) on skeletal tissue sections*. Methods Mol Biol, 2014. **1130**: p. 233-243.
251. Faust, J.J., B.A. Millis, and M.J. Tyska, *Profilin-mediated actin allocation regulates the growth of epithelial microvilli*. Curr Biol, 2019. **In press**.
252. Almutawa, W., et al., *The R941L mutation in MYH14 disrupts mitochondrial fission and associates with peripheral neuropathy*. EBioMedicine, 2019. **45**: p. 379-392.
253. Iyadurai, S., et al., *Variable phenotypic expression and onset in MYH14 distal hereditary motor neuropathy phenotype in a large, multigenerational North American family*. Muscle Nerve, 2017. **56**(2): p. 341-345.